# Molecular dynamics simulations of skin lipids

Evans, D. A.

*Award date:*
1996

*Awarding institution:*
University of Bath

# Molecular Dynamics Simulations of Skin Lipids

Submitted by D.A.Evans

For the degree of Ph.D.
of the University of Bath
1996



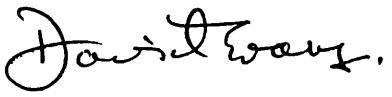

David A Evans





ProQuest LLC
789 East Eisenhower Parkway
P.O. Box 1346
Ann Arbor, MI 48106-1346

# ABSTRACT

Molecular Dynamics Simulations of Skin lipids

Submitted by D.A.Evans for the degree of Ph.D.

of the University of Bath

1996

The first dynamical models of stratum corneum lipid bilayer systems are presented. The models have been analysed to examine their structural and thermodynamic properties. Bilayers with cholesterol included, at low concentration, have been modelled in order to examine its effect upon the thermodynamic and structural behaviour of the system.

New methodology has been developed to enable both the simulation and analysis of these systems. Simulation artefacts associated with the use of truncated cutoffs, applied to the non-bonded interaction, have been analysed. Two new methods have been proposed and tested in order to circumvent this problem.

The bilayer systems are found to be stable over the course of the simulation. Segmental order parameter profiles were calculated and whilst the exact form of experimental profiles was not reproduced the values are within the bounds of those obtained experimentally. The cause of this discrepancy is attributed to the system conditions, size and the short time scale of molecular dynamics simulations

The effect of cholesterol upon the bilayer models has been found to mirror experiment. The general bilayer dimensions are unaffected by cholesterol but the segmental order parameters are increased, indicating a reduction in the fluidity of the lipid acyl chains.

## Acknowledgements

I would like to thank the following people for their help, friendship and companionship during the course of my Ph.D. studies in Bath:

David Osguthorpe for his supervision and help throughout the course of this work and help in reading and advising during the writing of this thesis. Pnina Osguthorpe for her help with work and life, general discussions about life and science. Prem Paul ( Unilever ) for his kind and helpful assistance from afar. Malcolm Campbell for providing entertaining work not always directly connected with my project.

The members of the Molecular Graphics Unit, who between them have made my time here very enjoyable and interesting, Andy ( Jif ) Lemon for sport and curries, Gareth Adams rugby and sport, Steve Joyce, Oz Parchment, Colette Maunder and her husband Ian, Phil Tollinton and Richard ( Sesh ) Sessions.

Life is not all work and I have to thank those people who have made my life here interesting and fun John McGinley for beer and football and more beer!, Jerry Gillespie for beer and rugby and thoughts about writing up, Nick and Lorraine Reeves for talk, cups of coffee and now a job and Jackie McInnes who shared a house with me for two and half years though neither of us can remember why!

Unilever Research Ltd, Port Sunlight Wirral, for there financial support both of the Ph.D. and for several international conferences.

Finally I would like to thank my parents Brian and Sandy and my sister Megan who have always been supportive of me and always encouraged me whenever it was required.

# CHAPTER 1

# INTRODUCTION

The entire surface of the human body is covered by a layer of skin. This is the largest single organ of the human body, in an average 65 Kg male the skin accounts for just over 12.5 % of the body mass, with an area of roughly 1.75 $m^2$. In addition to its obvious role as protection against physical abuse, the skin also has other equally important functions, relating to its forming the interface between the external environment and the internal organism, the human body.

## 1.1 The Functions of the Skin

Obviously the skin's complex structure is not there merely to hold the internal organism in, it is so structured to help[1]:

- prevent harmful substances from entering into the body
- prevent loss of essential fluids from the body
- protect against damage by ultra violet radiation
- regulate the body's temperature
- to contribute to the body's supply of vitamin D, by the affect of UV radiation upon dehydrocholesterol
- the immunological response of the body to outside attack
- endocrine function
- respiration
- contain nerve endings for sensory perception
- sociosexual communication

The stratum corneum makes the loss of essential fluids, especially water loss, to the surrounding environment very difficult, this semi-permable barrier can limit water loss to as low as 500 $cm^3$ per day.

## 1.2 Epidermal Structure and Histology

There are two recognisable layers to the skin, fig 1.2.1,

1. Epidermis
2. Dermis

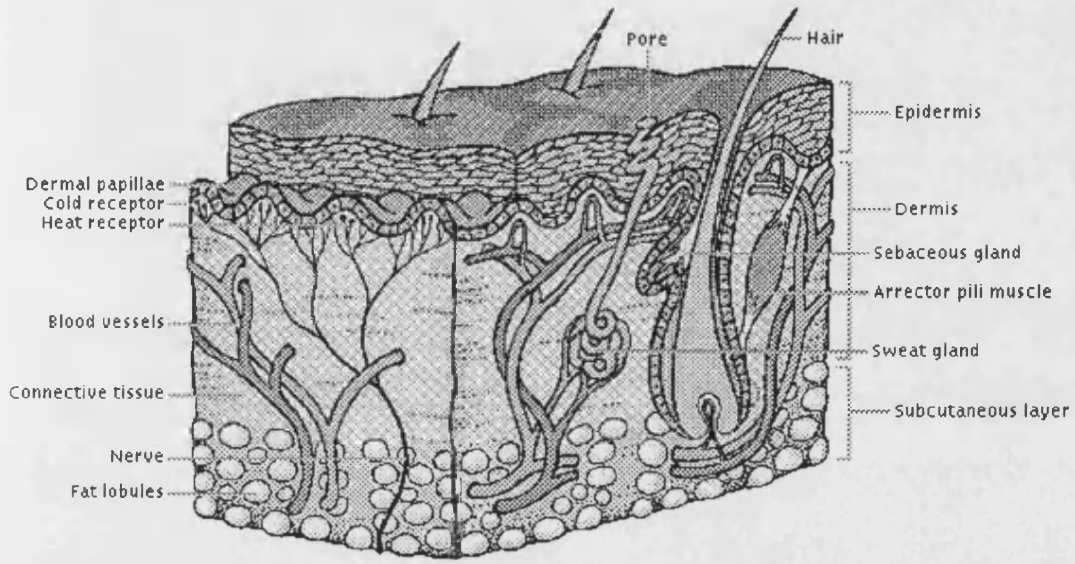


**Fig 1.2.1** Generalised diagram of Human skin

The outer layer, the epidermis is between 0.06 - 0.01 mm thick in most regions, but tending to be thicker on the back and much thicker in the callus areas. This forms most of the cutaneous appendages including the sweat glands and sebaceous glands, hair and nails.

The dermis is connective tissue and is much thicker than the epidermis, 2 - 4 mm. It supports the cutaneous appendages and contains blood vessels, lymphatics and nerves. The dermis consists of a dense network of connective tissue, in which bundles of collagen fibre predominate, intermingled with a mesh of elastic tissue.

The epidermis consists of epithelial cells growing in layers, fig 1.2.2. The deepest layer rests on top of the dermis and is attached to it by a *basement membrane*, cells of this layer, the *basal layer*, continuously divide, the daughter cells moving out towards the surface. As these cells migrate toward the surface they undergo a series of changes, the process of *Keratinization*, this involves the synthesis of *Keratin*, an inert fibrous protein with a high concentration of sulphur containing

residues. As the cells slowly reach the top surface of the skin, *stratum corneum* or *horny layer*, they have become fully keratinized dead cells.

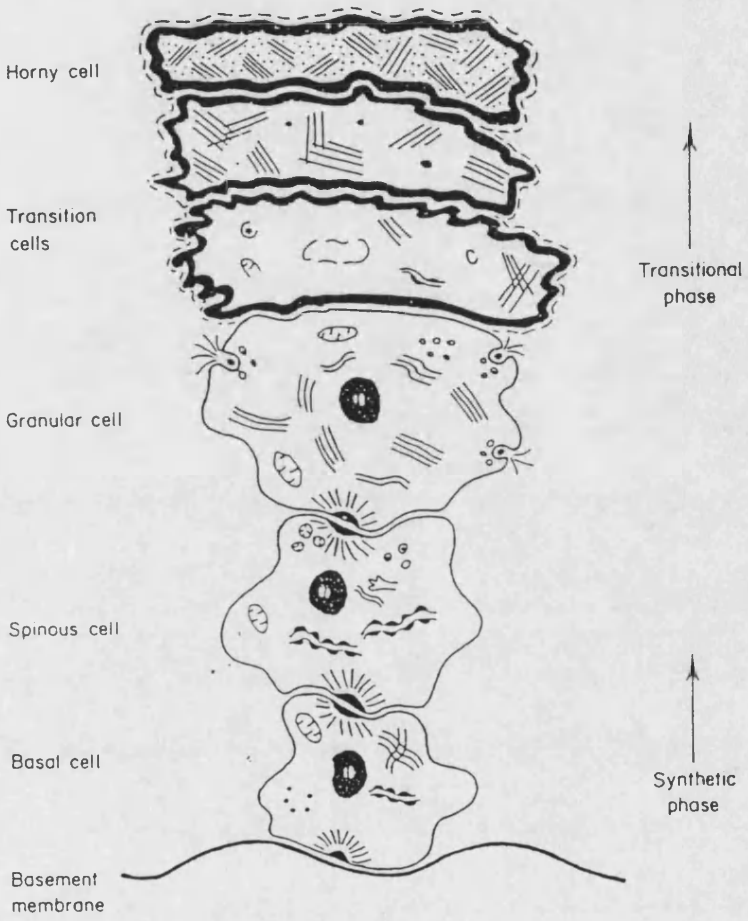


**Fig 1.2.2** Cell Types in the Epidermis ( not to scale )

These cells are devoid of nuclei and cytoplasmic organelles, these having degenerated by the time the cell reaches the upper granular level. The adjacent cells in the stratum corneum overlap and this locking together of the cells with a very large section of intracellular lipids forms a very effective barrier. This barrier is slowly abraded by the day to day activity of the individual.

## 1.3 The Semi-permeable Barrier

The skin is sub-divided into various regions, fig 1.2.1, and as early as 1853 it was recognised that these various layers were not equally permeable. Homalle[2] and Duriau[3] noted that blister formation indicates that the epidermis is considerably more impermeable than the dermis.

The outermost layer of the human skin is the stratum corneum, fig 1.2.2, this layer acts as the primary defensive barrier to foreign bodies. It has to be able to withstand the large diversity of conditions encountered, e.g. from partial to complete immersion in water to the drying affects of extended exposure to direct sunlight, in order to protect the human body. Therefore a knowledge of the structure, function and chemistry of the outermost layer is vital to our understanding of the affects our lifestyle has upon the skin.

The First World War promoted the interest in the skin's permeability, stimulated by the need to understand the affects of war gases and aerosols. Smith *et al* [4] noted that almost the entire amount of a mustard vessicant, dichloroethyl sulphide, could be washed off easily, 15 minutes after being applied to the skin. This led to the identification of the major barrier region, being in the uppermost part of the epidermis, the stratum corneum.

This was not immediately accepted, due to the mistaken belief that the stratum corneum was a grossly porous membrane through which large molecules as well as ions could easily move. This was further added to by the stripping experiments of Blank[5], in which successive layers of the skin are removed, this appeared to offer a way to finally locate the barrier zone with the stratum corneum. The water permeability of excised full thickness skin remained unchanged until the lowest part of the stratum corneum was removed. He erroneously concluded that a

"thin layer in this region must contain the rate-limiting barrier".

The conclusion was incorrect in that the observation only indicates that the lowest lying layers are quite impermeable. This does not indicate that they are any more impermeable than those upper layers of the stratum corneum. The data could equally be interpreted as implying that the bulk of the stratum corneum is uniformly impermeable, this has been shown in subsequent stripping experiments and acknowledged by Blank[6].

Today it is commonly accepted that the stratum corneum is the major rate limiting barrier in the skin[7-10]. Experiments have shown that there is no evidence that any section of the stratum corneum is any more or less permeable than any other, both top and bottom portions are excellent permeability barriers[11].

Transmission electronmicrographs of the stratum corneum in cross section show the arrangement of corneocyte cells surrounded by layers of narrow intercellular lipid[12]. This is shown schematically in fig 1.3.1. This arrangement of tightly packed corneocyte cell 'glued' together with lipid is believed to give the stratum corneum its barrier properties.

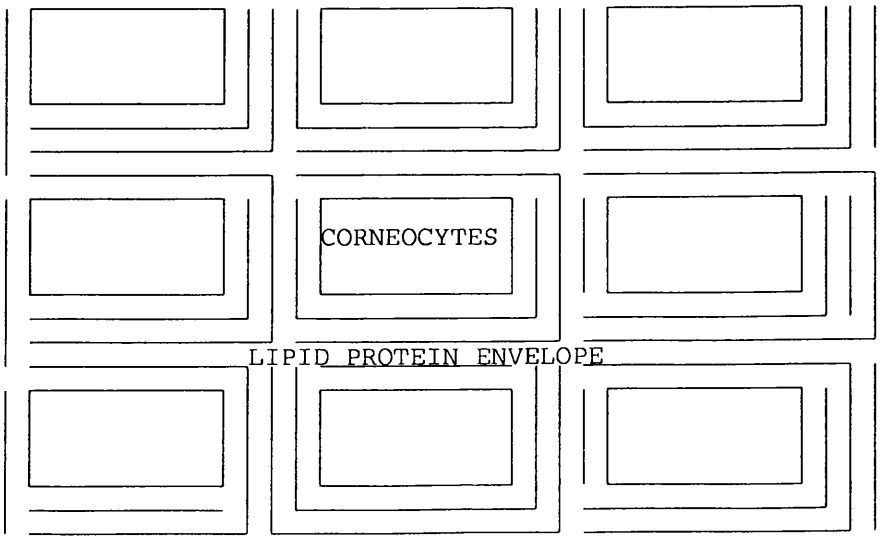


**Fig 1.3.1** Intercellular Lipid surrounding corneocytes

## 1.4 Barrier Properties

The question still remains as to the particular direction that an absorbed moiety has taken to gain entry through the stratum corneum. This either via a corneocyte pathway or more directly through the lipid lamellae.

Results from the investigation of the transport of $HgCl_2$ through human skin indicate that this occurs almost entirely through the intercellular lipids[13]. This lipid lamellae is now believed to be the pathway by which the majority of substances, including water, traverse the stratum corneum.

Thus it is essential that we investigate the molecular organisation of this region. This information will lead to a greater understanding of the processes involved in the different aspects of the skin's function and also give an insight into the possible affect that diseases of the stratum corneum have upon this structure.

Recent X-ray diffraction studies have indicated that the corneocytes are surrounded by single layer of lipids[12,14,15], in addition to the electron microscopy results that support the notion of lipid being found in the intercellular spaces[16]. Further investigation into these systems and the barrier properties needs to be augmented by a knowledge of the chemical nature of these skin lipids.

## 1.5 Chemical Analysis of the Stratum Corneum

The keratinized corneocyte cells are surrounded by a layer of bound lipid. In between these keratinized cells are dense regions of lipid. Chemical analysis of this region of the stratum corneum reveals that the intercellular region is comprised of three general groups of substances[17], table 1.5.1.

**Table** 1.5.1 Composition of the lipid region

| | % by mass of total lipid |
|---|---|
| Ceramides | 49.2 |
| Cholesterol | 19.6 |
| Fatty Acids | 26.0 |

## 1.5.1 Ceramides

Ceramides are a class of neutral lipids found predominantly in the stratum corneum. However shorter chain ceramides have been suggested to have some second messenger function and to be involved in cell regulation[18].

The ceramides have been separated into five to seven classes depending upon the number of hydroxyl groups attached and the length of their acyl chain, see fig 1.5.1

Recent molecular mechanics investigations by Nyholm, Pascher and Sundell into the conformation of glycoceramides are the only examples in the literature of theoretical calculations that have been performed upon ceramides[19]. There are a few crystal structures available[20], however all the crystal structures include a sugar group attached to the primary hydroxyl group, see fig 1.5.1. The majority of ceramide lipids found in the lipid envelope of the stratum corneum contain an isolated hydroxyl group[17].

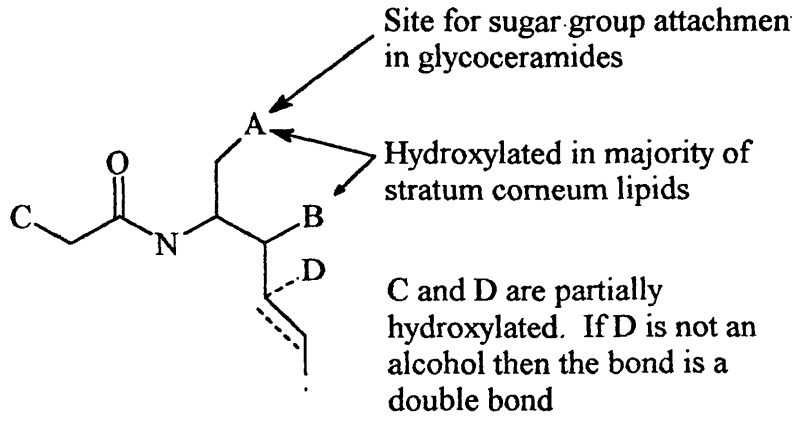


**Fig 1.5.1** Hydroxyl positions around ceramide head group

The ceramides found in the stratum corneum are shown in fig 1.5.2.

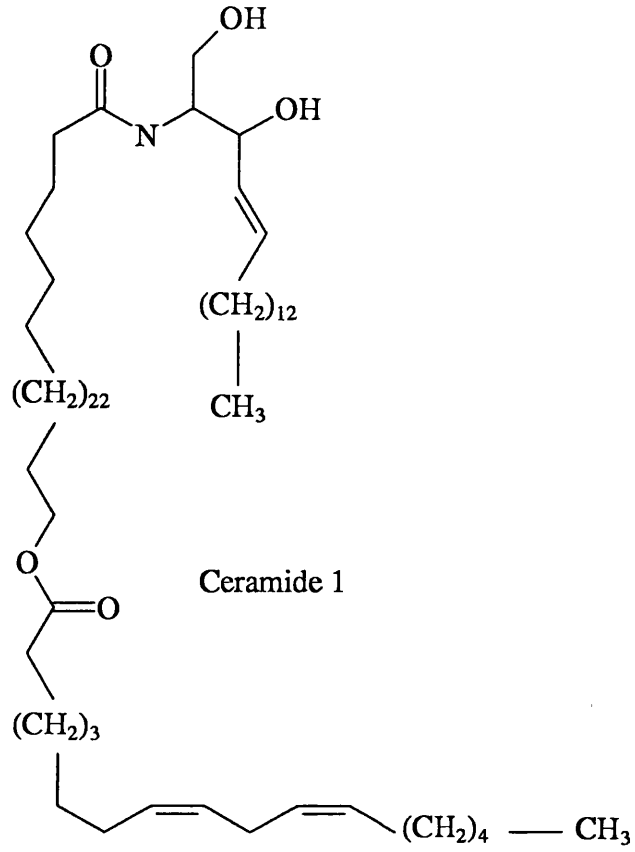

Ceramide 1

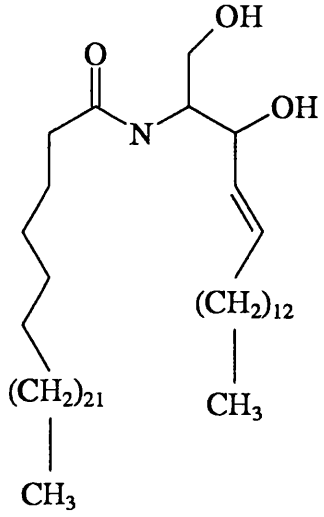

Ceramide 2

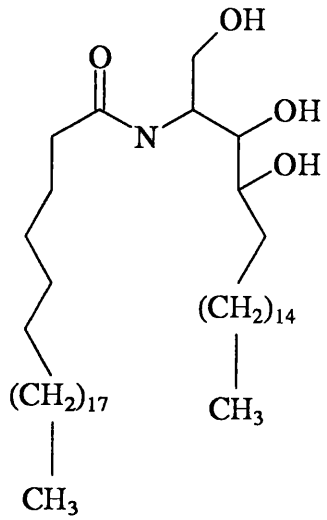

Ceramide 3

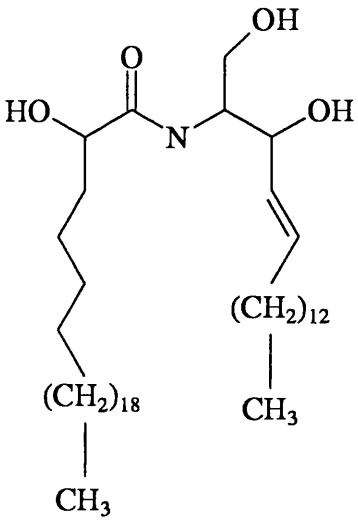

Ceramide 4

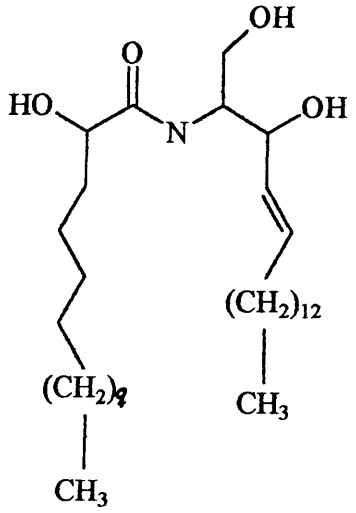


Ceramide 5

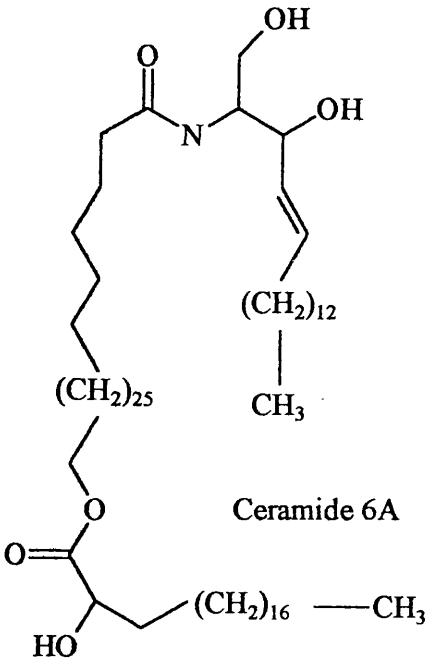


Ceramide 6A

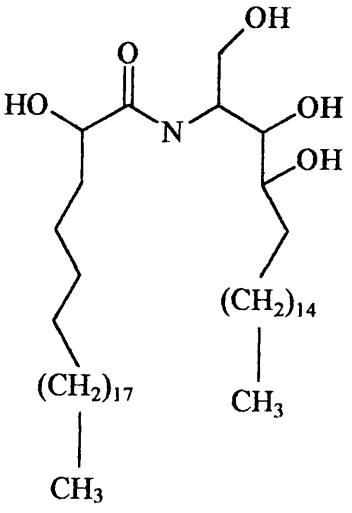


Ceramide 6B

## 1.5.2 Sterols

Another important class of lipids are sterols. These are based upon the sterol ring system of three fused six membered rings and a five membered ring, shown below in fig 1.5.3.

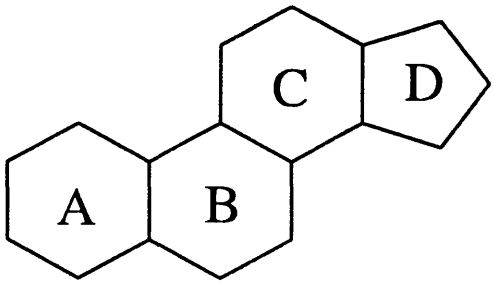


**Fig 1.5.3** Fused ring system of sterols

The most commonly found sterol in the skin and in biological membranes is cholesterol, fig 1.5.4.

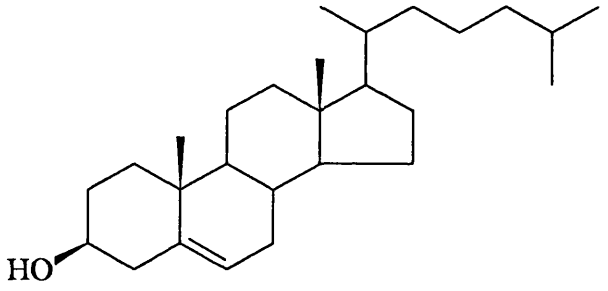


**Fig 1.5.4** Cholesterol

The hydroxyl group attached to the A ring can adopt two possible positions, either above or below the ring, see fig 1.5.5. The β isomeric form, with the hydroxyl group above the ring, is the naturally occurring isomer. The α isomers are known to be membrane anaesthetics.

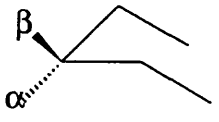


**Fig 1.5.5** α and β isomers of the steroid A ring

### 1.5.3 Fatty Acids

The rest of the lipid region is comprised of short/long chained fatty acids, such as palmitic, steric, oleic and docosamic acids.

## 1.6 Structural Aspects of the Stratum Corneum

Electron microscopy investigations of the stratum corneum using various staining techniques reveals an electron lucent region[12], usually referred to as the *horny cell plasma membrane*, found between the intercellular lamellae and the proteineous corneocyte envelope.

This layer is comprised of a monomolecular layer of ω-hydroxyacyl sphingosines that are chemically bound to the horny cell envelope. Thus in addition to the surrounding protein layer each cell also appears to have a lipid envelope. This envelope may function in corneocyte cohesion and the barrier properties of the stratum corneum[14].

In transmission electron micrographs the translucent region surrounding the corneocytes has the appearance of a cell plasma membrane[12]. There is little change in the appearance of the electron micrograph as the cells migrate from the granular layer into the horny layer, apart from a merging of the inner dense region of the membrane with the protein envelope. It is therefore natural that this region should be referred to as the plasma membrane, though it is now known that it bares little resemblance to true plasma membranes being comprised of neutral ceramides rather that the more common phospholipids found in plasma cell membranes. Also in contrast to plasma cell membranes no fatty acids, cholesterol or its derivatives are found with in this membrane, it is comprised solely of ceramides.

The phase properties of this 'membrane' are also significantly different from those of biological membranes. The long acyl chains are found in the gel phase rather than the more fluid liquid crystalline phase of phospholipids, as a result of which they are highly impermeable to water. Thus it is likely that the lipid covering is also involved in regulating water transport into and out of the corneocytes.

The translucent band disappears from the electron micrographs after treatment with alkali and extraction of the liberated lipids[12]. This indicates that the lipids are

bound to the corneocytes via an alkali labile bond, this is provided by the hydroxyl groups from either the lipid headgroups, see fig 1.5.1, or from the ω-hydroxy-tail groups.

### 1.6.1 Evidence for Bilayer Structure in the Stratum Corneum

In between the keratinized corneocytes there are areas of lipid lamellae. Freeze fracture electron microscopy has shown that this area is composed of multiple sheets of lipid[14,16]. This intercellular layer is formed by the rearrangement of lamellae disks from within the granular layer. These lamellae disks are discharged into the intercellular space in the form of membranous disks.

Landmann[21] first suggested that these disks are formed by the flattening of lipid vesicles. These disks then fuse edge to edge to form the extended lamellae sheets seen in the stratum corneum. Support for these concepts has been provided by the demonstration that specific epidermal lipids can produce flattening and stacking of liposomes prepared either from phospholipids[22] or stratum corneum lipids[23].

A consequence of Landmann's proposal is that each lamellar disk is comprised of two lipid bilayers. When the disks are fused together, edge to edge, each resulting disk should also contain two bilayers.

In 1991 Hou *et al* [24] identified the basic unit of the intercellular lamellae organisation, measuring 129 ± 2 Å.between the centre of consecutive interrupted electron lucent bands in the lamellae. A small angle X-ray diffraction study revealed a repeat unit of 131 ± 2 Å[25], both these results are in agreement with the proposed Landmann double bilayer unit. However theoretical studies presented by Bouwstra *et al* [26] showed that there are several plausible combinations of bilayer structures that will give the similar repeat unit results.

The spacing observed in X-ray diffraction studies of both dry and hydrated stratum corneum samples are very similar. Bouwstra *et al* [26] observed no swelling of the bilayers occurred upon hydration, this agrees with other studies upon murine[14] and human stratum corneum[27]. This indicates that there is very little water found between these bilayers under all hydration conditions, with only very small amounts of water intercalated between the lipid phases. This is in contrast to

other phospholipid enriched biological membranes where the polar headgroups are heavily hydrated[28].

By virtue of the amid head group the ceramides are capable of extensive intermolecular hydrogen bonding[29]. This, and the lack of headgroup hydration, may help to explains the unusually high order observed in these systems[30].

### 1.6.2 Cholesterol in Stratum Corneum Lipids

Transmission electron microscopy experiments have shown that there is very little cholesterol to be found in the lipid envelope surrounding the corneocytes[12]. This has been confirmed by filipin probing experiments[31].

Filipin is a polyene antibiotic that interacts specifically with cholesterol in membranes. This is observed as pitlike deformations, 25 nm diameter, in the membrane plane. The lipid envelope surrounding the corneocytes was found to contain very little cholesterol, whilst the intercellular lamellae were found to contain significant amounts of cholesterol. However, cholesterol was only found in high concentrations in the limiting membranes. The internal structures of the internal lamellae, the central bilayers of repeat units, were found to be poorly labelled with filipin.

These results indicate that the internal structures have either very low concentrations of cholesterol or that these membranes have a much greater rigidity[12], i.e. the filipin probe cannot enter into the membrane.

## 1.7 Phase Behaviour of Lipid Systems

Pure lipid systems exhibit thermotropic mesomorphism ( temperature dependent phase behaviour ) and those dispersed in water also exhibit lyotropic mesomorphism ( solvent dependent phase behaviour )[32]. Geometric factors dictate that for lipids with two chains the bilayer structure is the most favoured, rather than micelles or inverted hexagonal phases[28], fig 1.5.1.

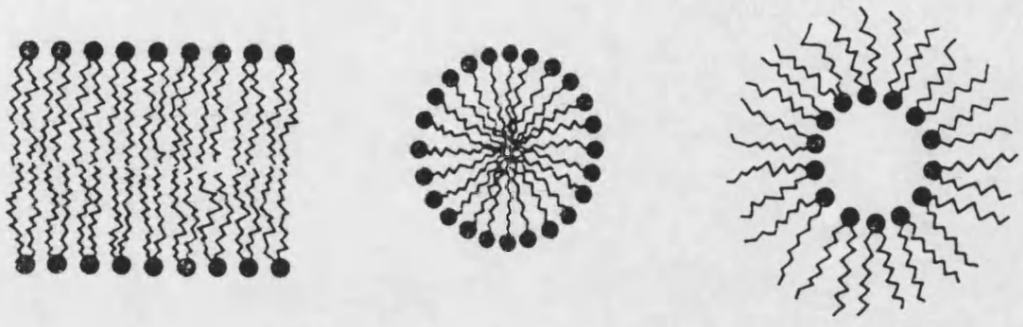

**Fig 1.5.1** Bilayer Structure and Micelles and Inverted Hexagonal Phases

The majority of the investigations of lipid phase behaviour have been performed upon phospholipid systems[33,34]. This is due to the importance of these lipids as major structural elements in biological membranes. This is a direct result of their self organisational properties arising from their amphiphilic nature. However the basic phase properties and changes seen in phospholipid model systems can equally be applied to ceramide systems. It is only recently that the thermodynamic nature of ceramide systems has begun to be investigated[13].

Phospholipids contain a hydrophilic headgroup, phosphate and hydrophobic acyl chains. When dispersed in water hydrophobic effects cause lipid aggregation, with the polar headgroups in contact with the water and the non-polar acyl chains away from the water.

The bilayer structure minimises the contact between the acyl chains and the water molecules. The thermodynamic stability of the bilayer structure may be explained by a number of interactions:

- hydrophobic interactions between the hydrophobic acyl chains
- electrostatic interactions between the polar headgroups and the water molecules
- electrostatic interactions within the headgroup framework.

Lipid-water phase diagrams have been determined using combinations of calorimetric and spectroscopic techniques to determine phase boundaries and X-ray

diffraction, electron-microscopy and NMR spectroscopy to determine specific phase structures[35,36].

Pure hydrated lipid bilayers undergo a calorimetric phase transition from a low temperature phase corresponding to a lamellar crystalline state, $L_c$, to a lamellar gel or ordered bilayer state, $L_\beta$ [28].

The molecular packing properties of the $L_c$ state are quite similar to those of anhydrous lipid crystals. Increasing the temperature causes the steric and Van der Waals interchain interactions favouring crystalline packing to be progressively counteracted by thermal rotational chain excitations. This corresponds to less tightly packed, more strongly hydrated lipid molecules and is accompanied by an increase in the interfacial lipid area, the $L_\beta$ state.

As the temperature increases the lipid acyl chain motion increases further and as the interfacial lipid area increases then eventually the headgroups achieve free rotation. To achieve this and simultaneously retain the close chain packing each lipid molecule is displaced relative to its neighbour along its long axis. As a consequence of this the bilayer surface breaks up into a series of periodic, quasilamellar bilayer segments, known as the $P_\beta$ or ripple phase.

As the temperature is further increased then the acyl chain rotation increases resulting in areas of rotationally isomerised chains, giving rise to fluid domains. This results in further hydration of the headgroup. These fluid domains then grow until all hydrocarbon chains within the bilayer are melted resulting in a fluid bilayer phase, $L_\alpha$.

The nomenclature used to describe lipid phases may be summarised as follows.

| | **Long Range Order Descriptions** |
|---|---|
| L | one-dimensional, lamellar |
| P | two-dimensional oblique or centred ( ripple ) |
| C | three-dimensional crystalline |

| | **Short Range Order Descriptions** |
|---|---|
| α | disordered fluid |
| β | untilted, partially ordered gel |
| β' | tilted, partially ordered gel |

## 1.8 Acyl Chain Motion

The molecular basis for the fluidity of bilayers arises from the rotation of the C–C single bonds in the acyl chain. The time averaged conformation of the acyl chains defines the particular phase of the system.

The carbon-carbon bonds in the alkane chain possess a threefold rotational symmetry arising from the tetrahedral geometry of the $sp^3$ carbon valency. This rotational potential originates from the electronic structure of the $sp^3$ bonds and may be expressed as

$$E_{(\phi)} = ( E_0 / 2 )( 1 - \cos 3\phi ) \qquad \text{( eqn 1.1 )}$$

where $\phi$ is the dihedral angle for the rotation about the C–C bond. For n-alkanes the barrier height $E_0$ is approximately 3.0 kcal $mol^{-1}$[37].

The minima corresponding to the staggered conformations occur at $\phi$ = 180°, ± 60°. The lowest energy minimum is the trans conformation at 180°, the two minima at ±60° corresponding to the two gauche conformations the two gauche

two gauche conformations are higher in energy by 0.5–1 kcal $mol^{-1}$. The barrier between trans and gauche conformations is approximately 3.6 kcal $mol^{-1}$ but the barrier between $gauche^{+}$ and $gauche^{-}$ is much larger[37].

In bilayer systems the intermolecular interactions between lipid chains also have to be taken into account in examining these isomerisation processes. The chain is not an isolated entity allowed total freedom of movement, it exists in a closely packed environment. The small magnitude of volume changes indicates the importance of co-operative packing of chains, with correlated chain motions in fluid lipid bilayers[28].

### 1.8.1 $^{2}$H NMR Spectroscopy of Acyl Chains

$^{2}$H NMR spectroscopy is a powerful technique for the investigation of membrane structure and has yielded information on the dynamics of both phospholipid and ceramide bilayers. The fluidity of the bilayer and specifically the acyl chains may be examined experimentally by $^{2}$H NMR spectroscopy[38,39], giving detailed information on the chain conformations.

This technique investigates the time average behaviour of the lipid acyl chains within the bilayer. By comparing results between homo and heterogeneous bilayers, the effect of dopant molecules may be examined and the way in which lipid acyl chains of varying length are accommodated in a bilayer.

The $^{2}$H NMR spectrum of perdeuterated acyl chains within fluid phase bilayers may be measured and from this data the orientational order parameter calculated for the acyl chains and the individual carbon positions[38]. These results give a direct measure of the fluidity of the bilayer.

NMR order parameters are computed from quadrupole splittings due to molecular rotation around axes perpendicular to the applied magnetic field give rise to sharp features split by:

$$\Delta\nu_q = 3/4\ A_q\ S_{cd} \qquad \text{( eqn 1.2 )}$$

where

$A_q$ is the quadrupole coupling constant

$S_{cd}$ is the orientational order parameter

$$S_{cd} = 1/2\ \langle\ 3\cos^2\theta_{cd} - 1\ \rangle \qquad \text{( eqn 1.3 )}$$

$\theta_{cd}$ is the angle between a carbon-deuterium bond and the bilayer normal.

## 1.9 Influence of Cholesterol upon Lipid Bilayers

There have been numerous studies performed investigating the effect that cholesterol has upon phospholipid bilayers. These studies have included both experimental investigations, e.g. NMR spectroscopy[40], ESR[41], X-ray diffraction[42] and fluorescence[43] as well as theoretical studies, e.g. molecular dynamics[44,45].

Cholesterol has a large effect upon biological membranes, it reduces permeability, increases molecular order and leads to a small increase in membrane thickness[41,43]. Cholesterol is also reported to reduce the hydration of the surrounding bilayer headgroups, resulting in a less polar environment.

The increase in the molecular order of the bilayer has been explained in terms of the interaction between the fused steroid ring and the surrounding lipids acyl chains[45]. Due to the fused steroid ring rigidity the surrounding acyl chains do not have the same potential free volume available for trans-gauche isomerisation to occur in. This leads to a increase in order at the top of the acyl chains. This increase in order, i.e. more trans dihedral angles in the upper acyl chains, leads to a slight

increase in the bilayer's thickness. This increase in the overall thickness of the bilayer will result in there being more free volume for the bottom dihedral angles of the acyl chains and thus an expected increase in the trans-gauche isomerisation and reduction in order. Thus the increase in order at the top of the acyl chain is balenced by a reduction in order at the bottom, corresponding to the experimental observation that there is no overall increase in the average number of trans dihedral angles seen per phospholipid.

## 1.10 Theoretical Studies upon Lipid Bilayer Systems

There have been numerous theoretical studies performed upon bilayer systems, using a variety of different techniques, approximations and conditions. These studies have investigated many different aspects of bilayer structure and properties, e.g. dynamic behaviour[46], phase behaviour[47,48], solvent effects[49], the effects of dopant molecules[45,50] and transport properties[51].

There are certain aspects of the experimental bilayer system which all models must attempt to resolve, through different techniques and varying degrees of approximation,

- the environment of the headgroups,
- the environment of the acyl chains
- the effect of any other bilayer components.

### 1.10.1 Head Group Environment

The headgroup environment has to take account of the interaction between the headgroups of the same monolayer and their interaction with the surrounding molecules, whether these be solvent or other lipid molecules. This has been investigated by examining the solvent structure around the head groups, by investigating the thermodynamic and dipole effects at the interfacial points, density profiles[49], torsion angles[52] and radial distribution functions[53].

**1.10.2 Acyl Chain Environment**

Molecular dynamics and Monte Carlo simulations have provided a wealth of data on both n-alkanes[54-57] and acyl lipid chains[49,53,58-70]. These studies have varied from the investigation of isolated hydrocarbons, through constrained hydrocarbon clusters to simulations of solvated phospholipid bilayers[46,65,67,71,72].

These simulations have often used constraints or simplifications to the system, potential energy or degrees of freedom, in order to speed the calculation and thus enable larger systems to be investigated or longer time scales to be used or more sampling to be performed.

These simplifications have included constraining the headgroup atoms in the plane of the bilayer by a restoring potential and the use of an united or reduced atom representation of the methylene units of the acyl chains. In the united model the methylene unit is replaced by a single atom representing both the carbon and the hydrogen atoms.This approximation reduces the time required for each step of the simulation. However, the electrostatics of the united atom group cannot match those of the full atom representation. The effect of this has been investigated by Hagler *et al* [73], in which they examined the ligand binding of Trimethoprim to *E.coli* Dihydrofolate Reductase using both an united atom and full atom models each with point charges. Their results led them to conclude that the united atom model failed to correctly represent the intermolecular forces in protein systems.

Kim *et al* [74] investigated the effect of using full atom representations in molecular dynamics simulations of Langmuir-Blodgett monolayers and concluded that the results where significantly better than those performed using only the united atom representation. Thus the use of united atom models in lipid chain dynamics must be questioned when the relationship between the chains themselves is of vital importance to structure and phase of the system. The advancement of modern high speed computers now allows the use of much more realistic models of lipids.

The analysis of these systems has generally concentrated on the experimental data available, such as torsion angle behaviour[52] and segmental order parameters[62]. Monte-Carlo studies have demonstrated the importance of chain

packing density to phase transition[75], by investigating a system of decane molecules and sampling the order parameter profiles.

### 1.10.3 Effect of Dopant

The interaction of various components usually found in membranes have also been investigated, from the inclusion of cholesterol in phospholipid bilayers to the simulation of membrane protein behaviour. X-ray diffraction results[43], $^{2}H$ NMR spectroscopy[41] and fluorescence[76] have been used experimentally to investigate the positioning and relative abundance of cholesterol in various phospholipid systems. Molecular dynamics and Monte-Carlo simulations have then studied the interaction of cholesterol with the phospholipid headgroups and their acyl chains[45,50]. In a few simulations[77] ceramides have been incorporated into the bilayer as dopant molecules but never examined in their own right as bilayers.

### 1.10.4 Other Bilayer Models

Other bilayer models include more simplified techniques, such as lattice models[78]. In theses models a lattice is used to represent the possible positions for a carbon segment. A vector normal to the bilayer and having a magnitude of the number of chains intersecting per unit defines the chain flux. For any given chain length the model is characterised by the surface packing density of lipid chains, obtained from X-ray diffraction results.

A further model used is that of Mean Field Theory[79]. A single chain is modelled under the influence of a general molecular field, representing the rest of the acyl chains of the bilayer. These models enable very long simulations to be performed and have produced results which agree well with experiment, e.g. in chain packing simulations[79,80]. However these models cannot provide dynamical information on molecular motions and they treat only approximately thermodynamic properties such as membrane phase transitions.

## 1.11 Molecular Modelling of Stratum Corneum Lipid Bilayers

The postulated double bilayer or multilayer structures of the stratum corneum are believed to be the fundamental structural elements that dictate the permeability of the skin. This permeability effects several of the skin's functions including essential fluid loss and the adsorption of substances through the skin. Hence, it is of great importance to investigate the chemical and structural aspects of these systems.

There have been numerous studies performed upon both extracted and model stratum corneum lipids using practical techniques, e.g. X-ray diffraction and transmission electron microscopy. However there have been no theoretical studies so far.

The work presented in this thesis will be concerned with the modelling of single unhydrated bilayer units. These systems will be unhydrated because of the lack of water found within the intercellular lamellar. The bilayers will be modelled using an empirical all atom force field to represent the potential energy of the system, and studied using Molecular Dynamics techniques.

## 1.12 References

1 Rook, Wilkinson and F.J.G.Ebling, Textbook of Dermatology (1992).

2 A. Homalle, Union Med 7 (1853) 222.

3 F. Duriau, Arch. Gen. Med. T.7 (1856) 161.

4 H.W. Smith, H.A. Clawes and E.K. Marshall, J. Pharmacol. 13 (1919) 1.

5 Blank I.H. J. Invest. Dermatol 45 (1965) 249.

6 Monash S. and Blank I.H. Archives of Dermatology 78 (1958) 710.

7 R.J. Scheuplein and I.H. Blank, Physiol. Rev. 51 (1971) 702.

8 G.M. Golden, D.B. Guzek, A.H. Kennedy, J.E. McKie and R.O. Potts, Biochem. 26 (1987) 2382.

9 R.O. Potts and M.L. Francoeur, Proc. Natl. Acad. Sci. USA 87 (1990) 3871.

10 R.O. Potts and R.H. Guy, Pharm. Res. 9 (1992) 663.

11 S. Monash, J. Invest. Dermatol 29 (1957) 367.

12 D.C. Swartzendruber, P.W. Wertz, K.C. Madison and D.T. Downing, J. Invest. Dermatol 88 (1987) 709.

13 J.A. Bouwstra, M.A. de Vries, G.S. Gooris, W. Bras, J. Brusse and M. Ponec, J. Cont. Rel 15 (1991) 209.

14 S.H. White, D. Mirejovsky and G.I. King, Biochem. 27 (1988) 3725.

15 F. Chang, D.C. Swartzendruber, P.W. Wertz and C.A. Squier, Biochim. Biophys. Acta 1150 (1993) 93.

16 D.C. Swartzendruber, P.W. Wertz, D.J. Kitko, K.C. Madison and D.T. Downing, J. Invest. Dermatol 92 (1989) 251.

17 G.M. Grey, R.J. White, R.M. Williams and H.J. Yardley, Br. J. Dermatol 106 (1982) 59.

18 A. Bielawska, C.M. Linardic and Y.A. Hannun, J. Biol. Chem. 267 (1992) 18493.

19 P.G. Nyholm and I. Pascher, Biochem. 32 (1993) 1225.

20 P.G. Nyholm, I. Pascher and S. Sundell, Chem. Phys. Lipids 52 (1990) 1.

21 L. Landmann, J. Invest. Dermatol 87 (1986) 202.(Abstract)

22 L. Landmann, P.W. Wertz and D.T. Downing, Biochim. Biophys. Acta 778 (1984) 412.

23 W. Abraham, P.W. Wertz and D.T. Downing, Biochim. Biophys. Acta 939 (1988) 403.

24 S.Y. Hou, A.K. Mitra, S.H. White, G.K. Menon, R. Ghadially and P.M. Elias, J. Invest. Dermatol 96 (1991) 215.

25 D.T. Parrott and J.E. Turner, Biochim. Biophys. Acta 1147 (1993) 273.

26 J.A. Bouwstra, G.S. Gooris, J.A. van der Spek, S. Lavrijsen and W. Bras, Biochim. Biophys. Acta 1212 (1994) 183.

27 R.O. Potts and M.L. Francoeur, J. Invest. Dermatol 96 (1991) 495.

28 G. Cevc and D. Marsh, Phospholipid Bilayers: Physical Principles and Models (Interscience, New York, 1987).

29 I. Pascher, Biochim. Biophys. Acta 455 (1976) 433.

30 B. Ongpipattanakul, M.L. Francoeur and R.O. Potts, Biochim. Biophys. Acta 1190 (1994) 115.

31 Y. Kitajima, T. Sekiya, S. Mori, Y. Nozawa and H. Yaoita, J. Invest. Dermatol 84 (1985) 149.

32 G. Lenaz, G. Curatola and L. Masotti, J. Bioenergetics 7 (1975) 233.

33 E. Ladbrook and D. Chapman, Chem. Phys. Lipids 3 (1969) 304.

34 H.L. Casal and H.H. Mantasch, Biochim. Biophys. Acta 779 (1984) 381.

35 M.J. Janiak, D.M. Small and G. Shipley, J. Biol. Chem. 247 (1979) 6068.

36 D. Marsh, Handbook of Lipid Bilayers (Crc Press, 1991).

37 P.J. Flory, Statistical Mechanics of Chain Molecules (Interscience, New York, 1969).

38 J.H. Davis, Biochim. Biophys. Acta 737 (1983) 117.

39 M.R. Morrow, D. Singh, D. Lu and C.W.M. Grant, Biophys. J. 64 (1993) 654.

40 M.R. Morrow, R. Srinivasan and N. Grandal, Chem. Phys. Lipids 58 (1991) 63.

41 F.A. Nezil and M. Bloom, Biophys. J. 61 (1992) 1176.

42 Y.K. Shin, D.E. Budil and J.H. Freed, Biophys. J. 65 (1993) 1283.

43 N.P. Franks, J. Mol. Biol. 100 (1976) 345.

44 O. Edholm and A.M. Nyberg, Biophys. J. 63 (1992) 1081.

45 A.J. Robinson, W.G. Richards, P.J. Thomas and M.M. Hann, Biophys. J. 68 (1995) 164.

46 K.V. Damodaran, K.M. Merz and B.P. Gaber, Biochem. 31 (1992) 7656.

47 T. Taga and K. Masuda, J. Comput. Chem. 16 (1995) 235.

48 T.X. Xiang and B.D. Anderson, Biophys. J. 66 (1994) 561.

49 M.A. Wilson and A. Pohorille, J. Am. Chem. Soc. 116 (1994) 1490.

50 H.L. Scott and W.S. McCullough, Biophys. J. 64 (1993) 1398.

51 S.J. Mckinnon, S.L. Whittenburg and B. Brooks, J. Phys. Chem. 96 (1992) 10497.

52 B.J. Hare, K.P. Howard and J.H. Prestegard, Biophys. J. 64 (1993) 392.

53 K.V. Damodaran and K.M. Merz, Biophys. J. 66 (1994) 1076.

54 A.D. Mackerell, J. Phys. Chem. 99 (1995) 1846.

55 R.M. Venable, Y.H. Zhang, B.J. Hardy and R.W. Pastor, Science 262 (1993) 223.

56 T. Fukada, S. Okazaki and I. Okada, Biophys. J. 64 (1993) 1344.

57 P. Padilla and S. Toxvaerd, J. Chem. Phys. 101 (1994) 1490.

58 K.C. Tu, D.J. Tobias and M.L. Klein, J. Phys. Chem. 99 (1995) 10035.

59 F. Zhou and K. Schulten, J. Phys. Chem. 99 (1995) 2194.

60 A. Pohorille and M.A. Wilson, Origins Of Life And Evolution Of The Biosphere 25 (1995) 21.

61 W. Shinoda, T. Fukada, S. Okazaki and I. Okada, Chem. Phys. Lett 232 (1995) 308.

62 R.W. Pastor, Current Opinion In Structural Biology 4 (1994) 486.

63 A.J. Robinson, W.G. Richards, P.J. Thomas and M.M. Hann, Biophys. J. 67 (1994) 2345.

64 S.G. Flicker and S.G. Bike, Abstracts Of Papers Of The American Chemical Society 208 (1994) 97.

65 T.R. Stouch, H.E. Alper and D. Bassolinoklimas, International Journal Of Supercomputer Applications And High Performance Computing 8 (1994) 6.

66 J.W. Essex, M.M. Hann and W.G. Richards, Philosophical Transactions Of The Royal Society Of London Series B- Biological Sciences 344 (1994) 239.

67 E. Egberts, S.J. Marrink and H.J.C. Berendsen, European Biophysics Journal 22 (1994) 423.

68 S.W. Chiu, E. Jakobsson, S. Subramaniam, M.M. Clark and H.L. Scott, Biophys. J. 66 (1994) A 300.

69 M.M. Clark, H.L. Scott, S.W. Chiu, E. Jakobsson and S. Subramaniam, Biophys. J. 66 (1994) A 300.

70 P.G. Khalatur, A.S. Pavlov and N.K. Balabaev, Makromolekulare Chemie-Macromolecular Chemistry And Physics 188 (1987) 3029.

71 T.R. Stouch, Molecular Simulation 10 (1993) 335.

72 T.R. Stouch and H.E. Alper, Faseb Journal 6 (1992) A 271.

73 P. Dauber-Osguthorpe, V.A. Roberts, D.J. Osguthorpe, J. Wolff, M. Genest and A.T. Hagler, Proteins-Structure Function And Genetics 4 (1988) 31.

74 K.S. Kim, M.A. Moller, D.J. Tildesley and N. Quirke, Molecular Simulation 13 (1994) 77.

75 O.G. Mouritsen, A. Boothroyd, R. Harris, N. Jan, T. Lookman, L. McDonald, D.A. Pink and M.J. Zuckermann, J. Chem. Phys. 79 (1983) 2027.

76 T. Parasassi, M.D. Stefano, M. Loiero, G. Ravagnam and E. Gratton, Biophys. J. 66 (1994) 120.

77 J.M. Boggs and K.M. Koshy, Biochim. Biophys. Acta 1189 (1994) 233.

78 K.A. Dill and P.J. Flory, Proc. Natl. Acad. Sci. USA 77 (1980) 3115.

79 D.R. Fattal and A. Benshaul, Biophys. J. 67 (1994) 983.

80 R.W. Pastor, R.M. Venable and M. Karplus, J. Chem. Phys. 89 (1988) 1112.

# CHAPTER 2

*Methodology*

## 2.0 Introduction

Molecules may exist in a variety of conformations, these will differ in energy depending upon the various interactions within the molecule and those with the surrounding system.

The relationship between a molecules' conformation and its energy is described by a multidimensional potential energy surface or **PES**. The PES describes the total available phase space of a molecule or molecular system.

It possible to approximate such a surface with an empirical fit of various mathematical expressions. The commonest approximations include terms to describe the energy required to deform internal co-ordinates, non-bonded and electrostatic interactions of a molecule, often known as a '*minimal*' representation
e.g.

$$E_{pot} = E_{bond} + E_{angle} + E_{dihedral} + E_{non\text{-}bond} + E_{electrostatic} \qquad (\text{eqn } 2.1)$$

The mathematical representation of this equation is known as the **FORCE FIELD**. Force fields differ in how they mathematically describe the individual terms and hence the values associated with them, also other terms may be included to explicitly characterise certain conditions and occurrences, e.g. hydrogen bonding[1,2].

## 2.1 Valence Force Field

The force field that will be used throughout the work discussed will be the **Valence Force Field[3]**. This has the form shown in equation 2.2 :

$$V_{pot} = \Sigma D_b [ 1 - e^{-\alpha (b - b_0)} ]^2 \qquad \text{Bond Strain Energy}$$

$$+ 1/2 \Sigma H_\theta ( \theta - \theta_0 )^2 \qquad \text{Angle Strain Energy}$$

$$+ 1/2 \Sigma H_\phi ( 1 + s \cos n\phi ) \qquad \text{Torsional Energy}$$

$$+ 1/2 \Sigma H_\chi \chi^2 \qquad \text{Out of Plane Energy}$$

$$+ \Sigma \Sigma F_{bb'} ( b - b_0 ) ( b' - b_{0'} ) \qquad \text{Cross Terms}$$

$$+ \Sigma \Sigma F_{\theta\theta'} ( \theta - \theta_0 ) ( \theta' - \theta_{0'} )$$

$$+ \Sigma \Sigma F_{b\theta} ( b - b_0 ) ( \theta - \theta_0 )$$

$$+ \Sigma \Sigma F_{\phi\theta\theta'} \cos \phi ( \theta - \theta_0 ) ( \theta' - \theta_{0'} )$$

$$+ \Sigma \Sigma F_{\chi\chi'} \chi \chi'$$

$$+ \Sigma \Sigma \varepsilon [ ( A / r^{12} ) - 2 ( B / r^6 ) ] \qquad \text{Lennard-Jones Energy}$$

$$+ \Sigma \Sigma q_i q_j / r \qquad \text{Electrostatic Energy}$$

( eqn 2.2 )

The parameters for this force field were refined to reproduce experimental data from a set of model compounds[3-5] and more recently further compared for use in lipid simulations[6].

### Bond Strain Energy

The bond deformation energy is represented by a Morse function. $b_0$ represents the preferred bond length, i.e. where there is no bond strain. The parameter $D_b$ is the depth of the function, the energy required to break the bond, i.e. to lengthen the bond from $b_0$ to $b_\infty$ i.e. an infinite distance between the two atoms. In

cases where there are exceptionally strained bonds a harmonic function may alternatively be employed:

$$E_{bond} = \frac{1}{2} k_b ( b - b_0 )^2 \qquad \text{( eqn 2.3 )}$$

$k_b$ is the force constant.

**Angle Strain Energy**

The angle deformation is represented by a harmonic function, where $H_t$ is the force constant and $q_0$ the preferred angle where there is no angle strain.

**Torsional Energy**

The torsion deformation is represented by a fourier expansion, which may be one of three terms, a onefold, twofold or threefold term[3]. The threefold term is sufficient to describe a torsion angle around a single bond, maxima at eclipsed positions ( 0°, ±120° ) and minima at staggered positions ( ±60°, 180° ). The twofold term is used to describe double and conjugated bonds, whilst the onefold term represents dipole - dipole interactions[7].

**Out of Plane Energy**

The out of plane term is required for conjugated systems[3], it describes the energy necessary to deform a conjugated system from planarity, i.e. $sp^2$ systems, alkenes, amides and arenes.

**Cross-Terms**

The previous terms are also referred to as *diagonal* terms. The Valence Force Field also includes *off-diagonal* or *cross* terms, representing the coupling between two or more internals. For example the bond - bond coupling term defines the change in energy of a stretched bond ( b ) when the adjacent bond ( b' ) is already stretched.

These terms are required to reproduce experimental vibrational data and will affect the shape of the potential surface in non-equilibrium regions.

**Lennard-Jones Energy**

The non-bonded interaction of an atom with the others in the system is represented by a *Lennard-Jones* potential. This describes all interactions between atoms separated by 3 bonds or more.

The function was originally proposed to explain the interatomic forces occurring in noble gas atoms[8]. It contains two separate terms:

- an attractive term, dependent upon $r^6$, which accounts for forces caused by induced polarisation effects.
- a repulsive term, dependent upon $r^{12}$, which accounts for replusions between electrons due to the Pauli exclusion principle.

**Electrostatic Energy**

The non-bonded electrostatic interaction energy of two atoms is represented as a pairwise *Coulombic* interaction between partial point charges centred on atoms. The parameters $q_i$ and $q_j$ are the partial charges on atom i and j respectively.

For the calculations presented in this work the values for $q_i$ and $q_j$ are pre-determined for all atom types with the exception of carbon. The charge on a given carbon atom depends upon its local environment and is determined to maintain overall neutrality as seen in the work of Hagler *et al* [3].

## 2.2 Spherical Cutoff Applied to the Non-Bond Potential

The non-bond potentials ( Lennard-Jones and electrostatic energies ) describe the influence of a single atom upon all the others of the system. This is calculated between all pairs of atoms separated by two or more bonds, this pairwise calculation is the longest part of the potential energy calculation and is the limiting factor in deciding the size of system that may be examined. However at large distances the interaction is small and it is therefore a good approximation to neglect it for distances

longer than a given cutoff value. This considerably reduces the time required to calculate this term of the potential energy.

The cutoff distance used is of immense importance to the calculation. If too short a cutoff is used then vital information will be ignored in the calculation, thus resulting in an unrealistic model, a long cutoff only results in longer time required to calculate the potential energy. Thus careful attention must be paid to the cutoff used and the compromise made between the accuracy of the model and the time required to perform the calculation. The Lennard-Jones energy falls off to a value that becomes small enough to be ignored, after roughly 8 Å. The electrostatic energy however, has effect at much longer distances, the interaction of charged groups greatly effecting the molecular geometry and energy. The interaction of charges is observed over distances considerably greater than that for the Lennard-Jones energy. Hence a longer cutoff is required before these interactions can be ignored. For the purposes of the calculations reported in this thesis a non-bond cutoff of 13 Å was employed.

## 2.3 Periodic Boundary Conditions

To simulate bilayer system one wishes to reduce surface or edge effects be observed. This is achieved by using *Periodic Boundary Conditions*[9], that is a cubic box, containing a model system known as the *unit cell,* is replicated throughout space to form an infinite lattice. Thus as a molecule leaves the unit cell an image of it will enter the unit cell from the opposite face, hence there are no walls at the boundary of the central box and no surface molecules.

This is implemented by assigning molecules from the unit cell and surrounding adjacent cell as *basic* and *ghost* molecules respectively. When one of the basic molecules crosses a periodic boundary, its co-ordinates are translated such that it enters the unit cell on the opposite side, the process is referred to as *swapping*. Basic molecules interact with both basic and ghost molecules whereas ghost molecules may only interact with basics. The co-ordinates of the system are maintained in their non-swapped form on the molecular dynamics output.

## 2.4 Minimisation

A molecule may exist in any of the accessible conformations on the PES. However stable structures are characterised by being stationary points on this surface, where the local energy is a minimum.
i.e.

$$\partial v / \partial r = 0 \qquad \text{( eqn 2.4 )}$$

where r are the co-ordinates.

It is assumed that biologically active molecules will exist as stable, low energy structures. Any random structure produced may have unfavourable interactions, e.g. steric clashes, so we have to be able to adjust this structure to reduce these interactions and to promote favourable ones.

This is achieved by the use of mathematical techniques known as *Minimisation Procedures*. Both the first and second derivatives of the potential energy with respect to the co-ordinates may be calculated analytically.
A typical minimisation strategy is:

1. Calculate energy of trial structure
2. Make a conformational change from derivative information
3. Loop over 1 and 2 until a pre-set maximum derivative value is achieved or a set number of steps of minimisation performed

The maximum derivative is set a target value dependent upon the size of system and any further calculations to be performed. As the molecule reaches an energy minimum upon the potential energy surface the derivatives will all increasingly tend toward zero. With large molecules or systems of molecules it may be necessary to set a target maximum derivative that merely assures that there are no large derivatives ( i.e. forces ) acting upon any part of the system.

There are several mathematical techniques that can be utilised to achieve this. They are classified according to how they calculate the direction of the next step.

## 2.4.1 First Derivative Methods[10]

These methods calculate the first derivatives of the potential energy with respect to the co-ordinates, this is then used to calculate the direction of the next step.

### Steepest Descents

This method uses only the first derivative information to minimise a structure. The next positions of the atoms are generated by purely following the first derivatives or gradients along the PES, the method follows the energy '*downhill*'.

$$x_k = x_{k-1} + l_k s_k \qquad \text{( eqn 2.5 )}$$

$$s_k = -g_k / |g_k| \qquad \text{( eqn 2.6 )}$$

where $X_k$ is the set of co-ordinates for the iteration k, $s_k$ the step direction as determined by the energy gradient vector $g_k$, and $l_k$ is the step size. This method is effective if the forces, i.e. gradients, on each atom are large, however as the structure approaches a stationary point, e.g. minimum, then the gradients tend to be very small and so this method becomes less effective.

### Conjugate Gradients

It is possible to exert more control over the minimisation by including information about the previous pathway in the current step. In conjugate gradients, information regarding the previous gradient is included in the calculation of the next direction to step, so that the next step will have a gradient that is '*conjugate*' to the previous step.

$$s_k = -g_k + b_k s_{k-1} \qquad \text{( eqn 2.7 )}$$

$$b_k = g_k^{\,2} / g_{k-1}^{\,2} \qquad \text{( eqn 2.8 )}$$

where $g_k$ is the gradient and $s_k$ the step size at iteration k, $b_k$ is the weighting factor, the ratio of the current and previous gradients.

This results in a more effective minimiser with better search direction and convergence properties than Steepest Descents.

### 2.4.2 Second Derivative Methods[10]

These methods use information about the second derivatives, the curvature of the surface, when calculating the direction of the next step.

#### Newton Raphson

There is a whole family of methods which are all derived from the Newton - Raphson method which requires first and second derivative information about the surface. The method proceeds by assuming that the PES is a quadratic function of the co-ordinates then the first derivative with respect to the co-ordinates is:

$$\partial v/\partial r = g + H ( r - r^0 ) \qquad \text{( eqn 2.9 )}$$

at a minimum $\partial v/\partial r = 0$ and hence the iteration step $s_k$ is given by:

$$s_k = ( r - r^0 )_k = -H^{-1}_k \; g_k \qquad \text{( eqn 2.10 )}$$

The different family of methods is born from different approaches to the calculation of the second derivative matrix, H, the *Hessian* matrix.

#### Quasi Newton-Raphson

This method builds up a numerical approximation to the Hessian, H, from the initial value of the gradient at previous iterations. Thus whilst a full analytical second derivative is not calculated the space for the matrix still needs to be allocated by the computer.

**Limitations on Second Derivative Methods**

There are limitations placed upon these second derivative methods due to the calculation of the Hessian matrix. This results in only relatively small systems being able to be examined by these methods.

The first derivative methods obviously do not suffer from this limitation and hence can be used for much larger systems, e.g. bilayers with > 1000 atoms. However the much better convergence properties of the second derivative methods around a minimum account for their use.

## 2.5 Molecular Dynamics

Biological systems do not exist as single stationary low energy structures. Rather they are dynamic systems in a continual state of change, traversing the accessible regions of the energy surface.

Thus via small changes in internal co-ordinates the general structure of a molecule will change. These seemingly small changes can lead to large conformational transformations, e.g. the chair - twist boat change in cyclohexane and the opening and closing of enzyme pockets.

In order to examine some these processes we need to be able to simulate the motions of the atoms due to the changing forces present upon them.

The collective motion of all the particles in a system over time can be described by *Newton's Second Law of Motion*,

$$F_i = m_i a_i \qquad \text{( eqn 2.11 )}$$

where $F_i$ is the force acting upon atom I which has a mass of $m_i$, and an acceleration of $a_i$.

The force on an atom can be calculated from its potential energy,

$$F_i = -\partial v / \partial r \qquad \text{( eqn 2.12 )}$$

thus the acceleration on an atom can be calculated:

$$a_i = F_i / m_i = -1 / m_i \; \partial v / \partial r \qquad \text{( eqn 2.13 )}$$

It is possible to calculate a new set of co-ordinates from the current ones by applying a Taylor expansion to the co-ordinates, i.e.

$$f_{(x+a)} = f_{(a)} + x/1!\, f'_{(a)} + x^2/2!\, f''_{(a)} + x^3/3!\, f'''_{(a)} + \ldots\ldots \qquad \text{( eqn 2.14 )}$$

when applied to the co-ordinates

$$r_{(r+\delta t)} = r_{(t)} + \delta t\, dr_{(t)} / dt + \delta t^2 / 2\ d^2 r_{(t)} / dt^2 + .... \qquad (\text{eqn } 2.15)$$

which gives

$$r_{(t+\delta t)} = r_{(t)} + \delta t\, v_{(t)} + \delta t^2 / 2\ a_{(t)} \qquad (\text{eqn } 2.16)$$

where

$v_{(t)}$ = velocity at time t

$a_{(t)}$ = acceleration at time t

The higher order terms of the expansion are ignored, this gives a small but persistent error.

### 2.5.1 Nature of the Time Step δt

It is assumed that the acceleration remains constant throughout the time step δt, unless an infitessimately small time step is taken then this assumption is not true. However this error may be ignored if sufficiently small time steps are taken.

It is usual to use a time step that is smaller than the time difference for the highest frequency vibration observed in the system. Typically these are bond stretches, with a maximum frequency around 3500 $cm^{-1}$, N--H stretch, this corresponds to a time for the vibration of 8 fs. In the following molecular dynamics simulations a time step of 1 fs is employed. This allows the calculation of properties dependent on the higher frequency vibrations yet maximises the time step with good energy conservation over the long term.

## 2.5.2 Molecular Dynamics Algorithms

The commonest algorithms used in biological simulations are based upon the *Verlet* algorithm.

### Verlet

The Verlet algorithm[11] is based upon a central difference solution to the Taylor series expansion,

$$r_{(t+\delta t)} = r_{(t)} + \delta t\, v_{(t)} + \delta t^2/2\, a_{(t)} \qquad \text{( eqn 2.17 )}$$

$$r_{(t-\delta t)} = r_{(t)} + \delta t\, v_{(t)} + \delta t^2/2\, a_{(t)} \qquad \text{( eqn 2.18 )}$$

Combining these together gives

$$r_{(t+\delta t)} = 2r_{(t)} - r_{(t-\delta t)} + \delta t^2\, a_{(t)} \qquad \text{( eqn 2.19 )}$$

Notice that this equation only requires information about the co-ordinates and the accelerations to calculate the next set of co-ordinates, no velocity information. The velocities may be calculated by a simple derivative equation,

$$v_{(t)} = ( r_{(t+\delta t)} - r_{(t-\delta t)} ) / 2\,\delta t \qquad \text{( eqn 2.20 )}$$

these may be used to calculate the kinetic energy of the system and hence its temperature.

### Leapfrog

A variant upon the Verlet is the Leapfrog[9]. In this algorithm the velocities are used to calculate the next set of co-ordinates,

$$r_{(t+\delta t)} = r_{(t)} + \delta t\, v_{(t+\delta t/2)} \qquad \text{( eqn 2.21 )}$$

the velocities are calculated by

$$v_{(t+\delta t/2)} = v_{(t-\delta t/2)} + \delta t^2/2\, a_{(t)} \qquad \text{( eqn 2.22 )}$$

The algorithm derives its name from the velocities being half a time step out of phase with the co-ordinates and accelerations, and 'leapfrogging' over them when recalculated.

**Velocity Verlet**[12]

The leapfrog algorithm was written because it was desired to include the velocities in the generation of the next co-ordinates. However the implementation of this involves the velocities being out of phase with the co-ordinates and accelerations by half a time step. The Velocity Verlet is a direct solution of the Taylor series approximation used in the initial Verlet algorithm. Thus in this algorithm the co-ordinates, velocities and the accelerations are all at the same time step and are in phase,

$$r_{(t+\delta t)} = r_{(t)} + \delta t\, v_{(t)} + \delta t^2/2\, a_{(t)} \qquad \text{( eqn 2.23 )}$$

the velocities are then calculated by a half step predictor - corrector

$$v_{(t+\delta t/2)} = v_{(t)} + \delta t/2\, a_{(t)} \qquad \text{( eqn 2.24 )}$$

and

$$v_{(t+\delta t)} = v_{(t+\delta t/2)} + \delta t/2\, a_{(t+\delta t)} \qquad \text{( eqn 2.25 )}$$

to give

$$v_{(t+\delta t)} = v_{(t)} + \delta t/2\, [\, a_{(t)} + a_{(t+\delta t)}\, ] \qquad \text{( eqn 2.26 )}$$

A requirement of all Verlet derived algorithms is that they give identical co-ordinate trajectories. The implementation of the Velocity Verlet in the **VFF** gives an identical co-ordinate trajectory to both the Verlet and Leapfrog algorithms, but also gives an identical energy trajectory to the Verlet as they are derived from identical solutions to the Taylor series expansion.

### 2.5.3 Initial Velocities for a Molecular Dynamics Simulation

The initial velocities for a simulation are assigned from a *Maxwell-Boltzman* distribution about a predefined temperature,

$$f(v)\,dv = [\, m / 2\pi k_b T \,]^{3/2} \exp[-m v^2 / 2 k_b T\,]\, 4\pi v^2\, dv$$

### 2.5.4 Calculation of Temperature and Pressure

**Temperature**

Temperature is a thermodynamic quantity, it can be related to the average kinetic energy of the system through the *equipartion principle*, hence for a single atom,

$$K.E. = 3/2\, k_b T \qquad (\text{eqn } 2.27)$$

thus

$$T = 1/3\, m v^2 / k_b \qquad (\text{eqn } 2.28)$$

**Pressure**

There are two contributions to the calculation of the system pressure, from the ideal and non-ideal behaviour of the system. The ideal contribution is derived from calculating the pressure of an ideal gas, from the kinetic energy, the potential energy being zero.

$$PV_{ideal} = N k_b T = 1/3 < \Sigma \ p_i^2 / m_i > \qquad (\text{eqn } 2.29)$$

The non-ideal component, the *virial* $\omega$, is described by the potential energy of the system.

$$\omega = -1/3 \Sigma r_i \nabla_{ri} V = 1/3 \Sigma r_i f_i \qquad (\text{eqn } 2.30)$$

where $\nabla_{ri} V$ is the derivative of the potential energy V.
Thus for intermolecular interactions:

$$PV = Nk_bT_i + <\omega> \qquad (\text{eqn } 2.31)$$

and the instantaneous pressure is,

$$P_i = Nk_bT + \omega / V \qquad (\text{eqn } 2.32)$$

where $T_i$ is the instantaneous temperature and V the volume.

## 2.5.5 Statistical Ensembles

The molecular dynamics algorithms described produce trajectories that are in the *micro-canonical* ensemble or *constant NVE*, that is a constant number of particles, N, volume, V, and total energy, E. The temperature and pressure vary.
It may be desirous to run simulations under other conditions to provide further information about the system under investigation. Common conditions for biological simulations are those of :

1. Constant Temperature, *constant NVT*
2. Constant Temperature and Pressure, *constant NPT*

**Constant Temperature Simulations**

The conceptually simplest method for conducting constant temperature simulations is the direct scaling of the velocities,
e.g. proposed for the Leapfrog algorithm by Brown and Clarke[13]

$$V_{(t+\delta t/2)} = \beta\, v_{(t-\delta t/2)} + \delta t\, a_{(t)} \qquad \text{( eqn 2.33 )}$$

where

$$\beta^2 = ( 3 ( N - 1 ) T_r / T \qquad \text{( eqn 2.34 )}$$

$T_r$ is the required temperature and T is the actual temperature of the step. The ( N - 1 ) factor occurs due to the removal of three degrees of freedom by the constraint of zero total linear momentum.

This gives a constant temperature simulation, but tends to deliver a rather harsh scaling of the velocities, thus adversely effecting the simulation[9].

A less harsh method was proposed by Berendsen *et al* [14] in 1984. In this method the velocities that appear in the generation of the next step are scaled.

$$r_{(t+\delta t)} = r_{(t)} + \lambda\, \delta t\, v_{(t+\delta t/2)} \qquad \text{( eqn 2.35 )}$$

where

$$\lambda^2 = 1 + \delta t / \tau [ T_r / T - 1 ] \qquad \text{( eqn 2.36 )}$$

This has the effect of a *temperature bath*, where the atoms of the system interact with the bath and are scaled accordingly. The severity of the interaction is governed by the *temperature bath time constant* $\tau$, as $\tau$ approaches $\delta t$ then $\lambda$ becomes

similar to Brown and Clarke's $\beta$, whereas when $\tau$ approaches infinity then the simulation becomes completely decoupled from the temperature bath and reverts to a micro-canonical simulation.

As was mentioned previously a requirement of Verlet derived algorithms is that they give identical co-ordinate trajectories. Thus it is possible to express each algorithm in terms of each other, and hence it is possible to form equations of motion in the Velocity Verlet that perform the same scaling as those derived by Berendsen for the Leapfrog.

The following set of new equations has been derived for temperature bath scaling using the Velocity Verlet,

$$r_{(t+\delta t)} = r_{(t)} + \lambda\, \delta t\, v_{(t)} + (2 - \lambda)\, \delta t^2/2\, a_{(t)} \qquad \text{(eqn 2.37)}$$

where $\lambda$ is Berendsen's scaling factor.
Thus it is possible to perform constant temperature dynamics with the Velocity Verlet using the methodology of Berendsen *et al*[14] .

**Constant Pressure Simulations**

In their 1984 paper Berendsen *et al* [14] also described an algorithm for performing constant pressure dynamics, scaling the co-ordinates and allowing unit cell parameters to vary with the simulation conditions.
The co-ordinate scaling factor used is similar to that for the constant temperature dynamics,

$$r' = \chi^{1/3}\, r \qquad \text{(eqn 2.38)}$$

where

$$\chi = 1 - \delta t / t_p\, (P_r - P) \qquad \text{(eqn 2.39)}$$

with $\beta_T$ being the isothermal compressibility and $P_r$ the required pressure, of the system.

Again the severity of the coupling to the pressure bath is controlled by the *pressure bath time constant* $t_p$.

**Constant Temperature and Pressure Simulations**

It is possible to perform constant temperature and pressure simulations by combining the two methodologies described above.

These algorithms have been implemented in the **VFF** program using the Velocity Verlet algorithm as the integration framework by the author.

## 2.6 Analysis of Molecular Dynamics Simulations

The vast quantity of data that is produced by a molecular dynamics simulation needs to be analysed so to gain the fullest amount of information regarding the system. The simulations presented in this report have all been analysed using the in-house program **FOCUS**[15], Finally One Can Understand Simulations.

### 2.6.1 Time Averages and Standard Deviations

The statistical average and standard deviation of a property, P, are given by:

$$< P > = 1/N \Sigma p ( t_k ) \qquad \text{( eqn 2.40 )}$$

$$\sigma = ( < p^2 > - < p >^2 )^{1/2} \qquad \text{( eqn 2.41 )}$$

$< p >$ is time average of the property, where $p ( t_k )$ is the property value at time $t_k$ and $\sigma$ is the standard deviation.

### 2.6.2 Thermodynamic Properties

A number of thermodynamic properties may also be calculated from a trajectory, these are based upon the atomic co-ordinates and velocities, and the unit cell dimensions.

#### Thermodynamic Information

Information about the conditions of the simulation at each stored step are recorded on a molecular dynamics trajectory. These include unit cell vectors and volume, atomic and molecular pressure, temperature, total, potential and kinetic energies. The individual components of the potential energy for each molecule are also stored, that is $E_b$, $E_\theta$, $E_\phi$, $E_\chi$, $E_{vdw}$, and the individual energy components from the

cross-terms and the molecular and atomic pressure tensors ( components of the pressure ).

## 2.6.3 Structural Properties

The co-ordinates of the system are stored on the trajectory, this allows for the calculation of structural properties, their time dependence and ensemble averages.

### Average Co-ordinates

The co-ordinates at a particular step may be returned or the average co-ordinates for the whole simulation or part thereof may be calculated.

### Distances, Angles and Torsion Angles

The distance between two co-ordinates, the angle between three co-ordinates and the torsion angle between four co-ordinates may be calculated. These do not necessarily need to be connected co-ordinates, thus bonded and non-bonded distances may be calculated.

The ensemble averages and distributions may be calculated, e.g. measuring the distributions of trans and gauche conformations in the acyl chains.

## 2.6.4 Segmental Order Parameters

The segmental order parameters for C-H bonds in the acyl chains of the lipid molecules may be calculated and compared to experimental results from $^2H$ NMR spectroscopy, ( C-D bonds ).

A tensor, $S_{ij}$, is calculated:

$$S_{ij} = \tfrac{1}{2} < \cos \theta_i \cos \theta_j - \delta_{ij} > \qquad \text{( eqn 2.42 )}$$

where i,j = [ x,y,z ], $\theta_i$ is the angle subtended between that axis and the fixed system co-ordinate axis defined as the bilayer normal.

This defines the methylene groups average orientation relative to a long molecular axis.

The three molecular axes are calculated thus:

x-axis = H-H vector

y-axis = bisectrix of the H-C-H angle

z-axis = the vector perpendicular to the H-C-H plane

This may be compared to the experimental results by calculating an experimental order parameter:

$$S_{cd} = 2/3\ S_{xx} + 1/3\ S_{yy} \qquad \text{( eqn 2.43 )}$$

In an all trans chain with the chain aligned along the bilayer normal then segmental order parameter for each carbon is 1, whilst in a completely random chain, i.e. totally disordered, $S_{cd} = 0.0$.

## 2.6.5 Fourier Transforms

A principal tool in molecular dynamics analysis is the fourier transform[15-17]. It characterises a function of time in terms of typical frequencies. The mathematical definition of a Fourier transform is:

$$H(\nu) = \int h(\nu)\, e^{-j\nu t} = A(\nu) + B(\nu) \qquad \text{( eqn 2.44 )}$$

where $H(\nu)$ is the frequency domain representation of the function of time $h(\nu)$. In general $H(\nu)$ is a complex function, with A and B being the real and imaginary components.

Fourier transforms may be applied to the both thermodynamic and structural properties, revealing characteristic frequencies. High frequencies are associated with

short time scale events, e.g. bond stretches, and low frequencies with much longer time scale events, e.g. conformational change.

**Filtering**

This method is based upon digital signal processing techniques, in which 'filtering' is used in order to remove 'noise' from an electric signal. Each atomic trajectory may be treated in an analogous manner.

This involves three steps:

1. Fourier transform each trajectory
2. Apply a filtering function to remove the unwanted frequencies
3. Apply an inverse Fourier transform to back transform into the time domain.

This allows both thermodynamic and structural properties to be investigated. Structural properties may be filtered to reveal the motion associated with a characteristic frequency[16,18-21]. The thermodynamic properties may be filtered to reduce 'noise' and thus reveal any correlations between the properties[15,16].

## 2.7 Software

### 2.7.1 VFF: Minimisation and Molecular Dynamics

The program VFF[3] is a combined molecular mechanics and dynamics program for calculating the energetic, dynamic and structural properties of molecular systems. The following information is required:

- Cartesian co-ordinates of the system
- Residue library describing the connectivity and bond order of the molecules
- The force field parameters used in the energy calculation ( eqn 2.2 )
- A control file for the running the program, containing information regarding the number of steps and any relevant physical information

This information is used to calculate the internal geometry of the system followed by the potential energy and first and second derivatives with respect to the Cartesian co-ordinates. This allows for the energy minimisation procedures to be

performed. A trajectory of the atomic co-ordinates, velocities and energy components may then be calculated.

### 2.7.2 INSIGHT: A Molecular Graphics Program

INSIGHT[22] is a molecular graphics program used on a graphics workstation which allows the construction, manipulation and analysis of molecular systems. The Cartesian co-ordinates of these systems may be obtained and redisplayed, the periodic images may also be displayed. Systems may be solvated, in a variety of solvents, using a *SOAK* facility.

### 2.7.3 ALIGN: An alignment program

The ALIGN[23] program requires a Cartesian input file which is rotated and aligned along a specified axis. This produces the base molecular configuration for the generation of a bilayer.

### 2.7.4 GENBIL: A bilayer generation program

GENBIL[23] constructs a bilayer using a previous aligned Cartesian co-ordinate file. This program allows for bilayers of differing size and density to be produced.

### 2.7.8 FOCUS: A molecular dynamics analysis program

FOCUS[15] allows for the analysis of molecular dynamics trajectories, by making available at each saved time step the atomic co-ordinates, velocities and energetics of the system. These may then be used to calculate the instantaneous and time average values of a property.

## 2.8 References

1 S.J. Weiner, P.A. Kollman, D.A. Case, U.C. Singh, C. C.Ghio, S. Alagona, S.J. Profeta and P. Weiner, J. Am. Chem. Soc. 106 (1984) 765.

2 U.C. Singh, P.K. Weiner, J.W. Caldwell and P.A. Kollman, (1988) (Abstract)

3 P. Dauber-Osguthorpe, V.A. Roberts, D.J. Osguthorpe, J. Wolff, M. Genest and A.T. Hagler, Proteins-Structure Function And Genetics 4 (1988) 31.

4 A.T. Hagler, E. Huler and S. Lifson, J. Am. Chem. Soc. 96 (1974) 5319.

5 S. Lifson, A.T. Hagler and P. Dauber, J. Am. Chem. Soc. 101 (1979) 5111.

6 T.R. Stouch, K.B. Ward, A. Altieri and A.T. Hagler, J. Comput. Chem. 12 (1991) 1033.

7 U. Burket and N.L. Allinger, Molecular Mechanics (American Chemical Society, Washington, D.C. 1982).

8 P.W. Atkins, Physical Chemistry (Oxford University Press, Oxford, 1982).

9 M.P. Allen and D.J. Tildesley, Computer Simulation of Liquids (Oford Science Publications, Oxford, 1987).

10 R. Fletcher, Practical Methods of Optimization (Wiley, N.Y. 1980).

11 L. Verlet, Phys. Rev. Z 159 (1967) 98.

12 W.C. Swope, H.C. Anderson, P.H. Berens and K.R. Wilson, J. Chem. Phys. 76 (1982) 637.

13 D. Brown and J.H.R. Clarke, J. Molec. Phys. 51 (1984) 1242.

14 H.J.C. Berendsen, J.P.M. Postma, W.F. van Gunsteren, A. DiNola and J.R. Haak, J. Chem. Phys. 81 (1984) 3684.

15 D.J. Osguthorpe and P. Dauber-Osguthorpe, Journal Of Molecular Graphics 10 (1992) 178.

16 R.B. Sessions, D.J. Osguthorpe and P. Dauber-Osguthorpe, J. Phys. Chem. 99 (1995) 9034.

17 P. Dauber-Osguthorpe and D.J. Osguthorpe, J. Comput. Chem. 14 (1993) 1259.

18 P. Dauber-Osguthorpe and D.J. Osguthorpe, J. Am. Chem. Soc. 112 (1990) 7921.

19 P. Dauber-Osguthorpe and D.J. Osguthorpe, Biochem. 29 (1990) 8223.

20 R.B. Sessions, P. Dauber-Osguthorpe and D.J. Osguthorpe, J. Mol. Biol. 210 (1989) 617.

21 D.J. Osguthorpe, Journal Of Molecular Graphics 6 (1988) 221.

22 T. Taga and K. Masuda, J. Comput. Chem. 16 (1995) 235.

23 P.J. Tollinton, University of Bath, Bath, U.K. (1994).

# CHAPTER 3

*Simulation Details*

## 3.0 Introduction

It is of great importance in molecular dynamics simulations that the starting conformation should not adversely influence the direction in which the simulation proceeds. A simulation must be allowed to develop under the control of the potential energy force field and any constraints placed upon the system.

Thus it is very important to be extremely careful when constructing the initial system and to carefully investigate results from early calculations for instabilities or artificially introduced phenomena.

## 3.1 Lipid Conformation

The head group conformation and stereochemistry were obtained from a crystal structure of a brain glucoceramide[1,2] obtained from the Cambridge Crystallographic Database[3]. Individual structures of ceramide 4 and 5 were then constructed using the Insight[4] molecular modelling package and minimised using the VFF[5] to produce minimised initial geometries. These structures were used as the starting lipid conformation for the generation of the ceramide bilayers.

## 3.2 Cholesterol Conformations

The crystal structure for cholesterol[6] was obtained from the Cambridge Crystallographic Database[3] and a single cholesterol moiety extracted from the unit cell using the Insight[4] molecular modelling package and minimised using the VFF[5] to produce the initial geometry. The 3-$\alpha$ isomer was constructed by a simple inter-change of the hydroxyl and hydrogen substituents of the 3-carbon and then further minimised using the VFF[5].

## 3.3 Generation of Bilayer Conformations

The bilayer conformations used in the following simulations were all constructed using similar methodology. The constituent lipid in the bilayer was built using the Insight[4] Molecular Modelling suite and any relevant crystallographic information. This lipid was then minimised until the total average absolute derivative was less than $10^{-4}$ kcal $mol^{-1}$ $Å^{-1}$. This conformation was duplicated and the two lipids positioned so as to represent one molecule from each monolayer of the bilayer, fig 3.3.1.

**Fig 3.3.1** Representation of the two lipid bilayer construct

This two molecule bilayer was aligned using the ALIGN[7] program such that the longest length ( the bilayer normal direction ) was parallel to a specific cartesian axis, after which the structure was replicated in the two other cartesian axis directions to produce the desired bilayer size and head group density, using the GENBIL[7] program.

### 3.3.1 Minimisation of Initial Conformations

After the initial conformation has been produced by the above procedure, then any unfavourable interactions within the bilayer are removed by performing a steepest descents minimisation of a few hundred steps upon the isolated bilayer unit. Following this the minimisation is repeated using periodic boundary conditions, so as to include the interaction of the outer lipids with their periodic images of the bilayer.

This process is continued until the total average absolute derivative of the system is less than 0.5 kcal $mol^{-1}$ $Å^{-1}$. Once this has been achieved then the bilayer is used as the starting conformation for molecular dynamics simulations.

## 3.4 Initial Molecular Dynamics Simulations

Several initial simulations were performed upon the various bilayer conformations so as to investigate the stability of each. Whilst a system may appear to be stable upon energy minimisation, it may posses energy that will adversely affect the simulation. If this occurs then that starting conformation has to re-assessed and modified.

## 3.5 Starting Structures Presented in this Report

The simulation titles and the unit cell dimensions are shown in table 3.5.1. In all simulations the unit cell angles, α,β and γ are all 90°.

**Table 3.5.1** Simulation unit cell dimensions and titles

| Simulation | Simulation Title | Unit cell vector A Å | Unit cell vector B Å | Unit cell vector C Å | Unit cell volume Å$^3$ |
|---|---|---|---|---|---|
| Argon 1 | arg | 37.44 | 37.44 | 37.44 | 52491 |
| BPTI | BPTI 1, 2, 3 | 45.5 | 41.0 | 46.5 | 86746 |
| Ceramide 5 | C5_1 | 21.5 | 43.0 | 24.0 | 22185 |
| Ceramide 5 with β-cholesterol | C5_2 | 21.0 | 43.0 | 21.0 | 18963 |
| Ceramide 5 with α-cholesterol | C5_3 | 24.5 | 45.5 | 24.5 | 27311 |
| Ceramide 4 | C4_1 | 24.5 | 59.0 | 25.0 | 36138 |
| Ceramide 4 with β-cholesterol | C4_2 | 24.5 | 59.0 | 25.0 | 36138 |

## 3.6 Molecular Dynamics Simulation Details

### 3.6.1 Argon Simulations

A face centred cubic lattice of 864 argon atoms was constructed for test simulations to validate the Velocity Verlet molecular dynamics routine. The time step of 10 fs and a straight truncated non-bond cutoff of 11.236 Å were employed. The simulation total simulation averages were calculated at the end of each simulation.

### 3.6.2 BPTI Simulations

The crystal structure for BPTI[8] was obtained from the Brookhaven Protein Data Bank[9] and solvated using the Insight[4] molecular modelling suite. This structure was minimised to remove any clashes introduced by the solvation procedure, after which the structure was used as a test case to investigate the new temperature bath methodology used in conjunction with the Velocity Verlet molecular dynamics algorithm.

A time step of 1 fs and a straight truncation non-bonded cutoff of 13 Å with a 15 Å limit used for the generation of the neighbour list were employed. The simulation details, e.g. atomic co-ordinates, velocities, forces and energies together with molecular properties, were written to a history file every 10 molecular dynamics steps, i.e. every 10 fs.

### 3.6.3 Lipid Simulations

All the molecular dynamics simulations performed used a time step of 1 fs with the simulation details, e.g. atomic co-ordinates, velocities, forces and energies with molecular properties unit cell vectors and energies, recorded every 4 fs.

A straight truncation non-bonded cutoff of 13 Å was used to limit the Lennard-Jones and electrostatic interactions, with a 15 Å limit used for the generation of the neighbour list. The initial velocities were sampled from a *Maxwell-Boltzmann* distribution.

The ceramide 5 systems were sampled from a constant temperature and pressure ensemble with a target temperature and pressure of 320 K and 1 bar respectively. The time constants were 150 and 200 fs for the temperature and pressure baths respectively.

The ceramide 4 systems were sampled from a constant temperature ensemble with a target temperature of 320 K and a temperature bath time constant of 150 fs.

## 3.7 Definition of Acyl Chain Torsion Angles

The torsion angles defined for the acyl chains of Ceramides 4 and 5 are shown below in fig 3.7.1.

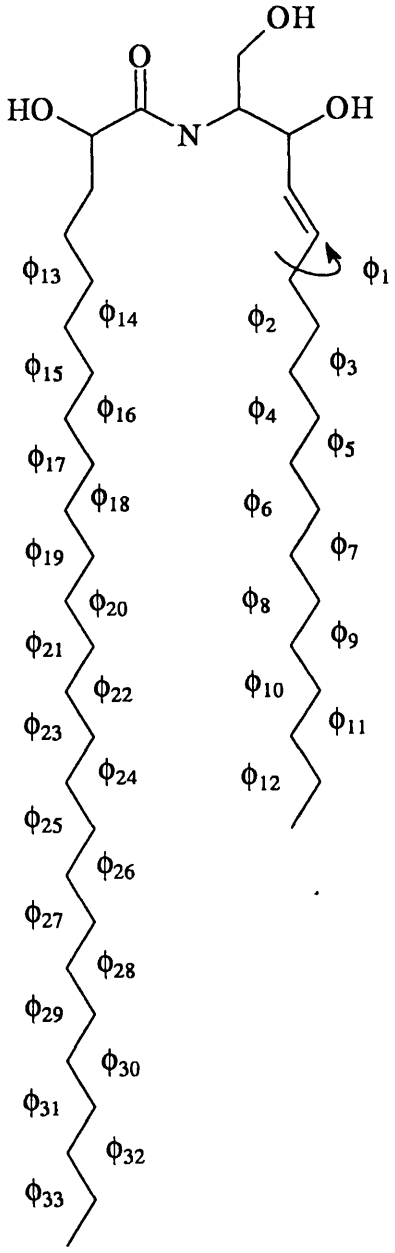


Ceramide 4 Acyl chain torsion angles

All initial torsion angles were set to 180 °

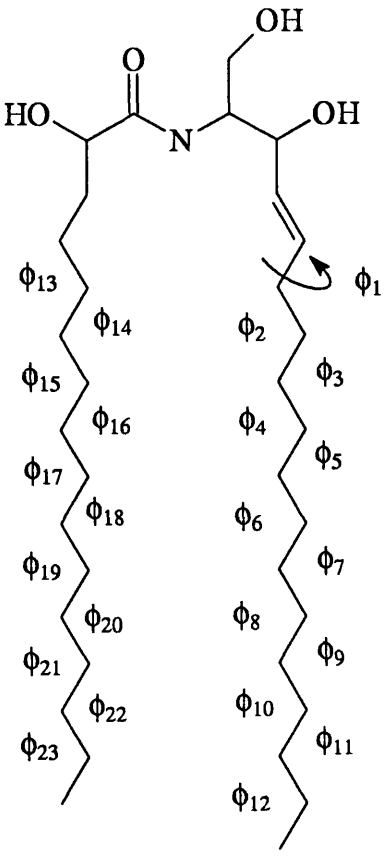


Ceramide 5 Acyl Chain Torsion Ang

All initial torsion angles were set to 180 °

**Fig 3.7.1** Acyl chain torsion angles.

## 3.8 References

1 P.G. Nyholm, I. Pascher and S. Sundell, Chem. Phys. Lipids 52 (1990) 1.

2 P.G. Nyholm and I. Pascher, Biochem. 32 (1993) 1225.

3 F.H. Allen, S. Bellard, M.D. Brice, B.A. Cartwright, A. Doubleday, H. Higgs, T. Hummelink, B.G. Hummelink-Peters, O. Kennard, W.D.S. Motherwell, J.R. Rodgers and D.G. Watson, Acta Crystallography Sect. B B35 (1979) 2331.

4 INSIGHT, BIOSYM technologies, San Diego, USA, (1989).

5 P. Dauber-Osguthorpe, V.A. Roberts, D.J. Osguthorpe, J. Wolff, M. Genest and A.T. Hagler, Proteins-Structure Function And Genetics 4 (1988) 31.

6 H.S. Shieh, L.G. Hoard and C.E. Nordman, Acta Crystallography Sect B 37 (1981) 1538.

7 P.J. Tollinton, University of Bath, Bath, U.K. (1994).

8 A. Wlodawer, J. Deisenhofer and R. Huber, J. Mol. Biol. 193 (1987) 145.

9 F.C. Berstein, T.F. Koctzle, G.J. Williams, E.F. Meyer Jnr, M.D. Brice, J.R. Rodgers, O. Kennard, T. Shimanouchi and M. Tasumi, J. Mol. Biol. 112 (1977) 535.

# CHAPTER 4

*Initial Testing of new Methodology*

## 4.0 Introduction

The work presented in this thesis has involved the implementation of new methodologies in the VFF[1] program, in order to perform molecular dynamics simulations under a variety of different conditions. Before proceeding with the work the new routines must be tested in order to check the validity of their use.

The implementation of the Velocity Verlet[2] integration algorithm may be tested by referring back to the original work of Verlet[3], in which he was investigating the Lennard-Jones fluid argon. After verification of the integration algorithm then the implementations of the constant temperature and pressure baths must also be validated.

Previous work[4] has indicated that there are considerable problems associated with the use of non-bond cutoffs in molecular dynamics simulations. This is observed even when performed under constant temperature bath conditions[4]. This has been investigated using a solvent and protein system; *Bovine Pancreatic Trypsin Inhibitor*, BPTI, in a large box of waters.

## 4.1 Argon Simulations

In his 1967 paper Verlet[3] was testing 'approximate theories' that attempted to reproduce experimental data by using newly developed computational techniques. As previously stated any Verlet derived molecular dynamics algorithm will give identical co-ordinate trajectories, thus this implementation of the Velocity Verlet should be able to reproduce the original work of Verlet.

The argon system under investigation is a face centred cubic lattice of argon atoms, with all the unit cell lengths equal at 31.792 Å, see table 3.1

The Lennard-Jones 6-12 representation of the Van der Waals energy may more formally be written as:

$$V(r) = 4\varepsilon[(\sigma/r)^{12} - (\sigma/r)^{6}] \qquad \text{(eqn 4.1)}$$

where $\varepsilon$ is the energy of the function at its minimum, with a separation of $\sigma$.

For this simulation a unit cell of 864 argon molecules in a face centred cubic packing arrangement was produced, with a density of 1.461 kg $m^{-3}$, with a $\varepsilon$ value of 0.238 kcal $mol^{-1}$ and a $\sigma$ value of 3.405 Å. A time step of 10 fs was used with a cut-off of 11.236 Å ( 3.3 $\sigma$ ), with an initial starting temperature of 420.0 K.

The results are shown below in table 4.1.1.

**Table 4.1.1** Comparison of Verlet derived algorithms with original results

| Simulation | Potential energy kcal $mol^{-1}$ | Pressure bar | Temperature K |
|---|---|---|---|
| Verlet[i] | – 777.3 | 1490.2 | 306.3 |
| Verlet[ii] | – 776.8 | 1494.7 | 306.2 |
| Leapfrog[ii] | – 775.4 | 1497.5 | 307.2 |
| Velocity Verlet[ii] | – 776.9 | 1499.5 | 306.1 |

[i] Original Verlet results[3]

[ii] Verlet derived algorithms in the VFF[1]

These results indicate that the implementations of the three Verlet derived algorithms in the VFF[1] are able to reproduce the original work of Verlet. The minor differences seen in the results are due to the initialisation of the Maxwell-Boltzmann[5] velocity distribution with a random number. The starting position in phase space dictates where the simulation will proceed to, thus different random numbers will result in slightly different results. However these results show that we are able to reproduce the original Verlet method.

Temperature and pressure bath scaling routines have been implemented using the Velocity Verlet[3] as the integration algorithm. These baths are in the spirit of those proposed by Berendsen *et al*[6]. The combination of these two baths results in a system that samples under constant temperature and pressure conditions.

## 4.2 Investigation of Temperature Effects due to a Spherical Cutoff

In previous work into hydrated phospholipid bilayers[4] a temperature disparity between the sub-components of the system was observed, even though constant temperature bath conditions were applied and the average temperature of the system was that of the target temperature. The velocities of the sub-components were different, with the water velocities much larger than those of the lipids. This results in the lipids being considerably colder than the surrounding solvent.

This problem occurs when performing simulations upon heterogeneous systems. It is a direct result of the cutoff used to truncate the pairwise non-bond interactions. The nature of a direct cutoff results in instabilities in the derivatives of those atoms at the edge of the cutoff.

### 4.2.1 Molecular Dynamics Simulations of Bovine Pancreatic Trypsin Inhibitor

Bovine Pancreatic Trypsin Inhibitor, BPTI, is a relatively small protein, 58 residues and 892 atoms, including all hydrogens. This, along with a great deal of knowledge regarding its tertiary structure from very accurate X-ray diffraction and neutron diffraction derived structures, has lead to BPTI becoming one of the most common test cases for molecular dynamics simulations.

The structure for BPTI[7] was obtained from the Brookhaven Protein Database[8], this was a combined X-ray diffraction and neutron diffraction study with an overall resolution of less than 1.5 Å and an r factor of 0.162.

This structure was solvated using the *soak* facility in the Insight[9] molecular modelling suite. This resulted in a system containing 5674 atoms, 892 protein and 4782 water atoms. The system dimensions are shown in table 4.2.1.

**Table 4.2.1** BPTI unit cell dimensions

| A<br>Å | B<br>Å | C<br>Å | Angles<br>$\alpha = \beta = \gamma$ ° | Volume<br>Å$^3$ |
|---|---|---|---|---|
| 45.5 | 41.0 | 46.5 | 90 | 86746 |

## 4.2.2 Molecular Dynamics Simulation of BPTI

The solvated BPTI system was investigated using the constant temperature methodology of Berendsen *et al*[6] with the Velocity Verlet[3] integration algorithm for 150 ps.

A 13 Å truncation non-bonded cutoff was employed with a 15 Å limit used for the generation of the neighbour list. A time step of 1 fs was employed with the thermodynamic, molecular and atomic data saved every 10 steps of the simulation. The temperature bath was used from the start of the simulation with a target temperature of 300 K and a temperature bath time constant of 150 fs.

The potential energy and the total average temperature and the average temperatures of the waters and protein were followed through the simulation. The results are seen in fig 4.2.1.

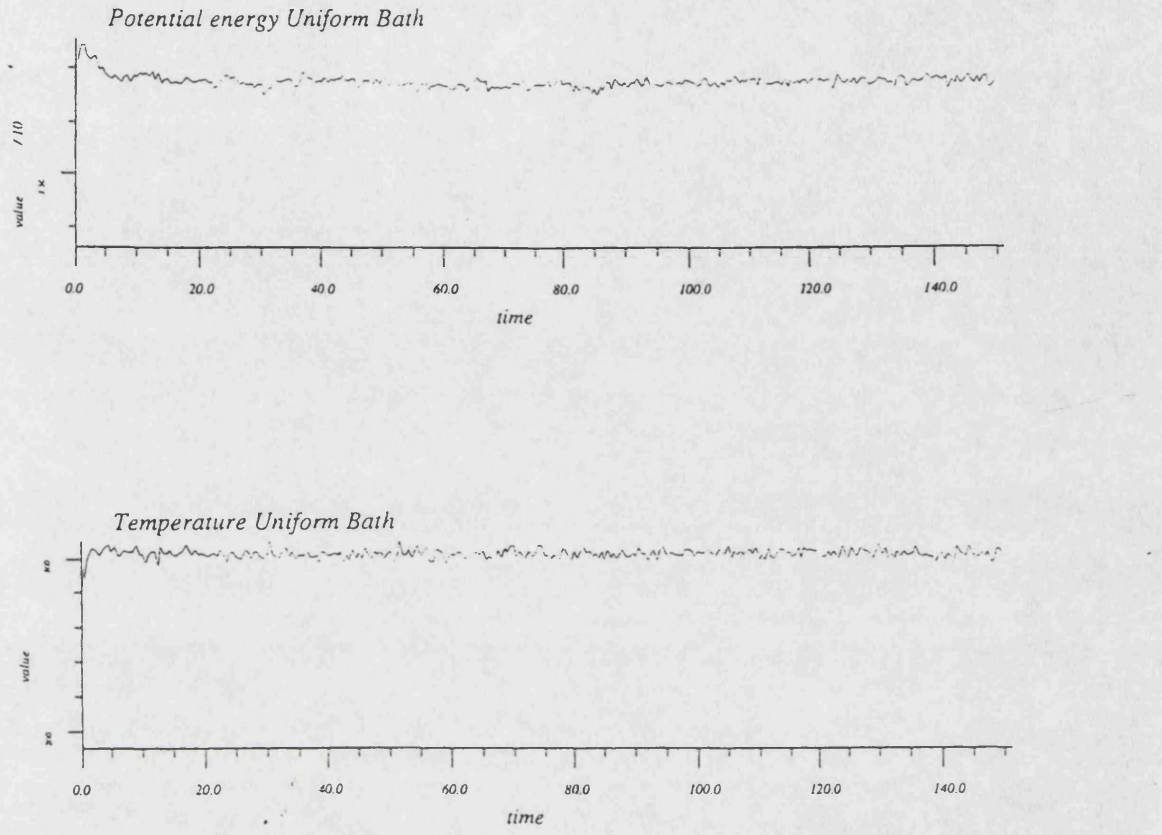


**Fig 4.2.1** Potential Energy and Temperature Profiles for Uniform Temperature Bath.

From the plots of the energies it can be seen that the simulation appears to be quite stable and continuing successfully after coming to 'equilibrium' after 15 ps. The averages for the whole simulation are shown in table 4.2.2 below.

**Table 4.2.2** BPTI 1 energy averages

| Parameter | Average 0-150 ps | Standard Deviation |
|---|---|---|
| Total energy kcal $mol^{-1}$ | – 8161.2 | 212.3 |
| Potential energy kcal $mol^{-1}$ | – 13273.3 | 212.6 |
| Kinetic energy kcal $mol^{-1}$ | 5112.1 | 46.0 |
| Temperature K | 302.3 | 2.7 |

These results indicated that the system is quite stable and that the temperature bath is working effectively with the average temperature 2 K above the target temperature.

However examination of the average temperature profiles for the individual sub-systems, water and protein, fig 4.2.2, reveals that the protein and water soon diverge in their temperatures with the protein rapidly lowering its temperature for the first 20-25 ps of the simulation before plateauing out, whilst the water temperature initially rises and then remains essentially constant from 2-5 ps onwards.

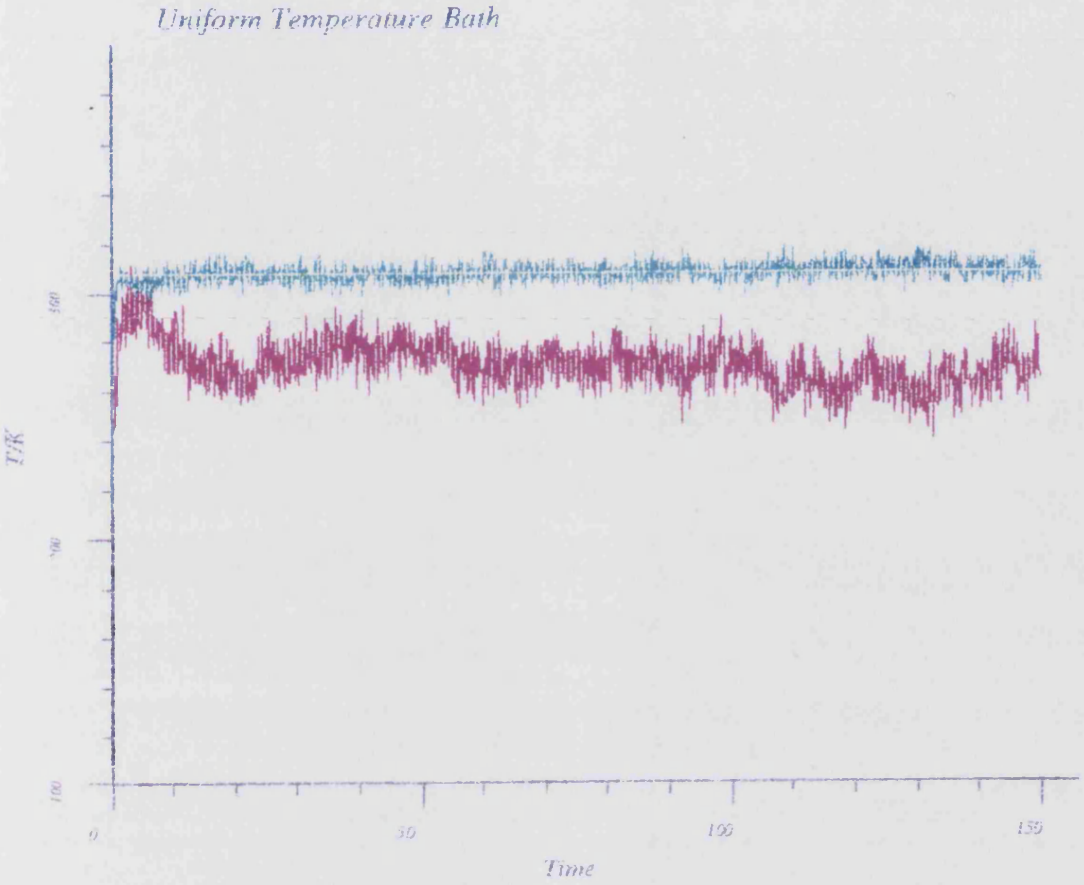


**Fig 4.2.2** Temperature Profiles for Protein ( red ) and Water ( green ) sub-systems.

The exact nature of this is seen in the statistics for the individual sub-systems, shown in table 4.2.3.

**Table 4.2.3** BPTI 1 sub-component average temperatures

| Temperature sub-system K | Average 0-150 ps | Standard Deviation |
|---|---|---|
| Waters | 307.7 | 4.4 |
| Protein | 270.4 | 9.3 |

These results show that the system does not have a balanced temperature distribution. Whilst the average temperature for the whole system was correct the

temperatures of the sub-components are not, the water temperature is 5 K higher in temperature than the system average and the protein is 32 K lower!

In this investigation the rational for employing the temperature bath was to ensure that the sub-system of interest, the protein, was simulated at the target temperature. These results show that this has not occurred, the protein is actually below 0° C and nearly 40 K cooler than the solvent it is in. Thus any results obtained from this simulation regarding the motion of the protein are for a protein at 270 K rather than one at 300 K.

## 4.3 Solutions using Temperature Bath Methodologies

Two solutions to this problem have been implemented in the VFF[1].
The two methods are:

- Reassignment of velocities from a Maxwell-Boltzmann distribution
- Multiple temperature baths

### 4.3.1 Reassignment of Velocities

The temperature of the system, or any sub-component of it, is dependent upon the kinetic energy of the individual atoms and hence their velocities. Thus whilst the velocities of the protein and water sections of the simulation were very different, their overall value is appropriate for the temperature.

We may attempt to remove the differences in sub-component temperatures by occasionally reassigning all the velocities of the whole system. The velocities are sampled from a Maxwell-Boltzmann distribution, at the temperature of the whole system at the previous step. This follows the methodology proposed by Swope *et al*[3], who were investigating water clusters.

A requirement of a molecular dynamics trajectory is that over a short time span it is back integrable, although for practical reasons ( finite precision ) and theoretical reasons ( the trajectory is chaotic ) it is not possible to back integrate the whole trajectory. However if there has been an irreversible change in any of the

variables seen in the integration equation, i.e. co-ordinates, velocities or accelerations, then it is impossible to back integrate even over a short time span.

Thus by reassigning the velocities to random new values it becomes impossible to back integrate over the reassignment and this effects what properties may be validly calculated from that simulation.

Time independent properties, e.g. temperature, potential energy and kinetic energy may be calculated for the whole simulation and their ensemble averages are statistically valid. However time dependent values should not be calculated over these reassignments, but may be calculated between them when the trajectory is back integrable. Thus co-ordinate properties such as diffusion or autocorrelation functions should not be calculated for the whole simulation.

### 4.3.2 Multiple Temperature Baths

In a similar manner to a single temperature bath it is also possible to use more than one, with a bath applied to a specific sub-set of atoms. This results in each sub-set of atoms being scaled to the correct temperature. This also affords the opportunity to specifically scale sub-systems to different temperatures and thus impart energy to a specific part of the system.

However, when scaling different sub-sections of a system with different scaling factors then angular momentum artefacts will be introduced. In order to overcome this the angular momentum of the system is calculated before any scaling is performed and any changes introduced by the scaling are corrected. This method should ensure that the protein and water sub-systems will be at the correct temperatures without any angular momentum artefacts being introduced into the system.

## 4 .4 Application of Multiple Temperature Baths and Velocity Reassignment

These two methods have been implemented in the VFF[1] program, by the author. These methods were tested using the solvated BPTI system described above.

- A single temperature bath was applied to the whole system with the same target temperature and time values as above, but the velocities of the systems were reassigned once every picosecond.
- One temperature bath was applied to the waters and another applied to the protein, both had the target temperature and time constant values used in the original single temperature bath simulation.

Each system was sampled for 150 ps with a time step of 1 fs. The temperature baths had a time constant of 150 fs.

### 4.4.1 Reassignment of Velocities

The potential energy and the temperature for the system are shown in fig 4.4.1, again these show that the system has stabilised, with 'equilibration' occurring after 30 ps.

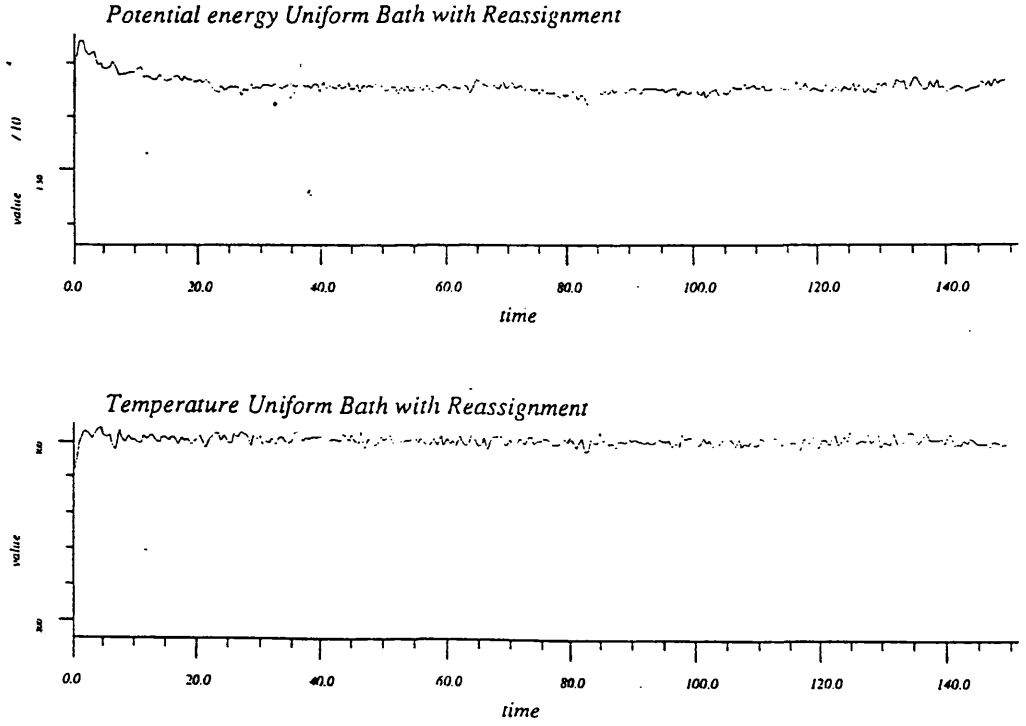


**Fig 4.4.1** Potential Energy and Temperature Profiles for the Reassignment of Velocities with a Uniform Temperature Bath.

Their averages are shown below in table 4.4.1.

**Table 4.4.1** BPTI 2 energy averages

| Parameter | Average 0-150 ps | Standard Deviation |
|---|---|---|
| Total energy kcal $mol^{-1}$ | – 8338.1 | 234.0 |
| Potential energy kcal $mol^{-1}$ | – 13439.8 | 233.0 |
| Kinetic energy kcal $mol^{-1}$ | 5101.6 | 42.9 |
| Temperature K | 301.7 | 2.5 |

As in the original simulation these values appear to indicate that the simulation has proceeded as required. This average temperature values for the waters and protein are shown below in table 4.4.2.

**Table 4.4.2** BPTI 2 sub-system average temperatures

| Temperature sub-system K | Average 0-150 ps | Standard Deviation |
|---|---|---|
| Waters | 302.6 | 4.0 |
| Protein | 296.2 | 8.7 |

This indicates that the implementation of the reassignment of velocities has resulted in the protein temperature approaching very closely the target temperature, and the water temperature only just exceeding it. This is seen clearly in fig 4.4.2 where the protein and water temperatures are very close.

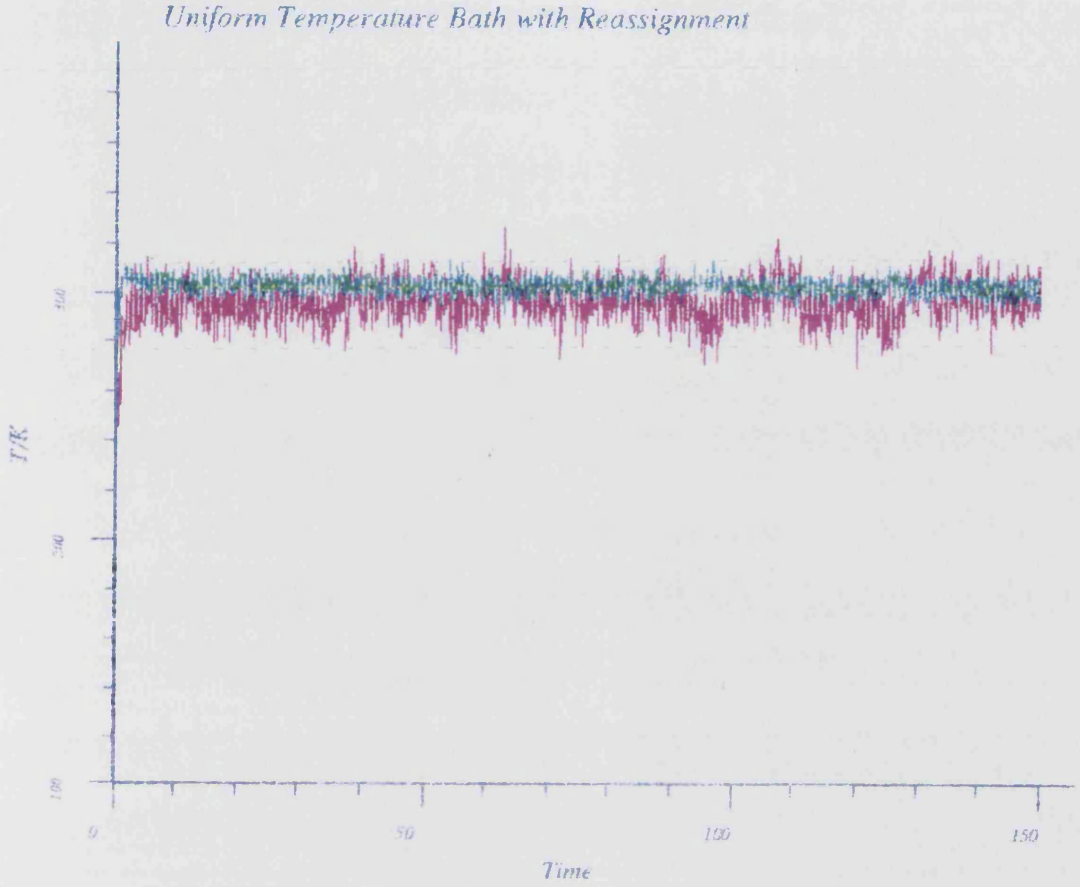


**Fig 4.4.2** Temperature Profiles for the Protein ( red ) and Water ( green ) sub-systems.

## 4.4.2 Multiple Temperature Baths

The potential energy and the temperature for the system are shown in fig 4.4.3.

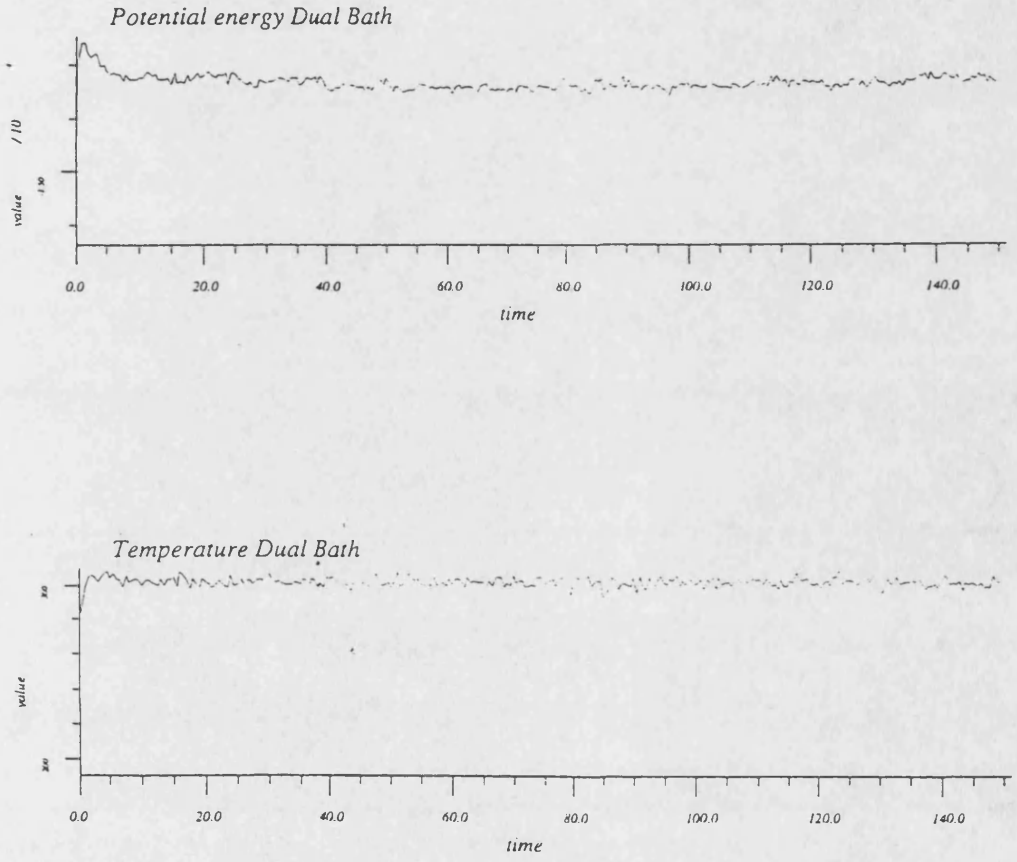


**Fig 4.4.3** Potential Energy and Temperature Profiles for the Multiple Temperature Baths.

Again these show that the system has stabilised and reached 'equilibrium' after 20 ps. The averages are shown below in table 4.4.3.

**Table 4.4.3** BPTI 3 energy averages

| Parameter | Average 0-150 ps | Standard Deviation |
|---|---|---|
| Total energy kcal $mol^{-1}$ | – 8238.9 | 221.1 |
| Potential energy kcal $mol^{-1}$ | – 13343.5 | 222.2 |
| Kinetic energy kcal $mol^{-1}$ | 5104.6 | 45.1 |
| Temperature K | 301.8 | 2.7 |

Again these values indicate that the simulation has proceeded as expected, the average values for the temperature of the waters and protein are shown below in table 4.4.4.

**Table 4.4.4** BPTI 3 sub-system average temperatures

| Temperature sub-system K | Average 0-150 ps | Standard Deviation |
|---|---|---|
| Waters | 302.1 | 3.9 |
| Protein | 299.8 | 7.9 |

These results together with fig 4.4.4, show that in this simulation the protein and waters are now essentially both at the target temperature. Thus in this simulation the protein can be fully analysed and investigated at the target temperature rather than being more than 30 K below it.

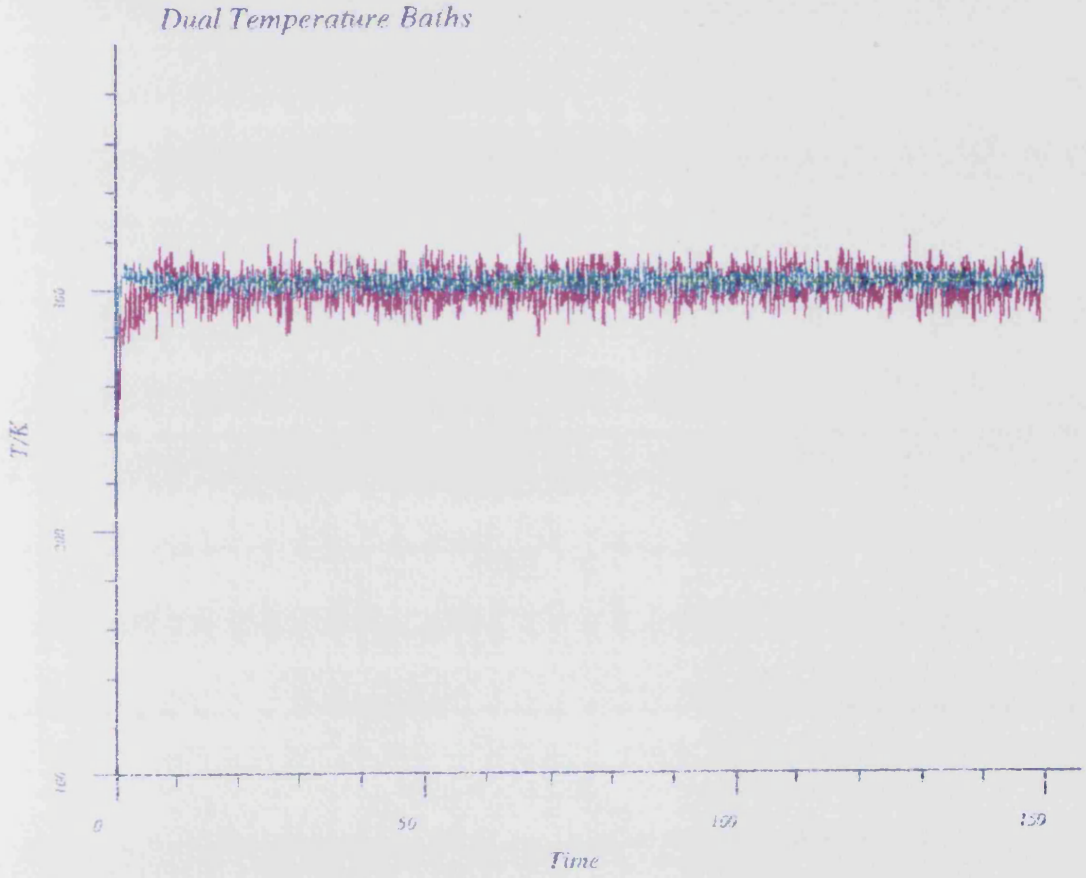


**Fig 4.4.4** Temperature Profiles for the Protein ( red ) and Water ( green ) sub-systems.

## 4.5 Conclusions

These results have shown that the single temperature bath methodology does not work for heterogeneous systems, when employing a cutoff to the non-bond functions. Thus further methodology needs to be employed in order to prevent the disparity in temperatures seen in different sub-sections of the system. The two methods presented here have both achieved the objective of simulating the protein and its solvent at the target temperature whilst each offers its own advantages and disadvantages.

The method involving the reassignment of velocities essentially performs a single Monte-Carlo step[2] this results in more of phase space being sampled. This is seen by examining the potential energy profiles for each method and their standard deviations, table 4.5.1.

**Table 4.5.1** Average Potential Energy and Standard Deviations

| Potential Energy kcal $mol^{-1}$ | Average 100-350 ps | Standard Deviation |
|---|---|---|
| Reassignment of Velocities | – 13429.8 | 233.0 |
| Multiple Temperature Baths | – 13343.5 | 222.2 |

The standard deviation for the reassignment of velocities method is larger than that for the multiple temperature baths. This indicates that more of phase space is being sampled by this method, obviously both of these methods sample more of phase space than the original simulation where the protein was at a much lower temperature

It may be useful to combine these two methodologies, using the reassignment of velocities in an initial equilibration stage and once equilibration is reached then using the multiple temperature baths. Thus allowing more phase space to be sampled initially and after equilibration all time dependent properties may be calculated. Also the reassignment of velocities method may be used as a tool to search conformational space.

## 4.6 References

1 P. Dauber-Osguthorpe, V.A. Roberts, D.J. Osguthorpe, J. Wolff, M. Genest and A.T. Hagler, Proteins-Structure Function And Genetics 4 (1988) 31.

2 W.C. Swope, H.C. Anderson, P.H. Berens and K.R. Wilson, J. Chem. Phys. 76 (1982) 637.

3 L. Verlet, Phys. Rev. Z 159 (1967) 98.

4 A.P. Lemon, Modelling the Biological Membrane (Ph.D. Thesis University of Bath, 1995).

5 P.W. Atkins, Physical Chemistry (Oxford University Press, Oxford, 1982).

6 H.J.C. Berendsen, J.P.M. Postma, W.F. van Gunsteren, A. DiNola and J.R. Haak, J. Chem. Phys. 81 (1984) 3684.

7 A. Wlodawer, J. Deisenhofer and R. Huber, J. Mol. Biol. 193 (1987) 145.

8 F.C. Berstein, T.F. Koctzle, G.J. Williams, E.F. Meyer Jnr, M.D. Brice, J.R. Rodgers, O. Kennard, T. Shimanouchi and M. Tasumi, J. Mol. Biol. 112 (1977) 535.

9 INSIGHT, BIOSYM technologies, San Diego, USA, (1989).

# CHAPTER 5

*Ceramide 5 Bilayer Simulations*

## 5.0 Introduction

This chapter will be concerned with the simulation of ceramide 5 bilayers. Three simulations are presented:

1. a pure ceramide 5 bilayer containing 18 lipids, C5_1,
2. a bilayer as in 1 where one central lipid from one monolayer has been replaced by one cholesterol, 5 cholesten-3β-ol, C5_2,
3. a bilayer as in 1 where one central lipid from one monolayer has been replaced by one 5 cholesten-3α-ol, C5_3.

Each simulation will be analysed to investigate its thermodynamic and structural behaviour. In addition the effect of the two dopant molecules will be assessed in terms of their effect upon the structural and thermodynamic properties of their respective bilayers, as well as the differences caused by the isomeric forms of cholesterol.

## 5.1 Pure Ceramide 5 Bilayer, C_1

The bilayer model C5_1, consisting of 18 ceramide 5 lipids in two 3x3 monolayers, was constructed using the methodology described in Chapter 3. Two ceramide 5 molecules were built and placed directly over each other in the 'bilayer' conformation, using the Insight molecular modelling suite. This construct was then aligned along the y-axis, now defined as the bilayer normal, the bilayer was then built by replication in the head group axes x and z.

Lattice points are separated by 7 Å in the x plane and 8 Å in the z plane. The resulting co-ordinates were minimised until the total rms. derivative was below 0.5 kcal $mol^{-1}$ $Å^{-1}$. These minimised co-ordinates were used as the starting conformation for the molecular dynamics simulation.

### 5.1.1 Simulation Conditions

The molecular dynamics trajectory was initially sampled in the constant NVE ensemble for 50 ps, after which the constant pressure bath was applied with a target pressure of 1 bar. After a further period of 15 ps the constant temperature bath was applied with a target temperature of 320 K. The bilayer simulation was sampled under these constant temperature and pressure conditions for a further 290 ps.

## 5.1.2 Thermodynamics

The thermodynamic data is stored on a trajectory history file every 4 steps of the simulation, this information can be extracted and manipulated using the FOCUS[1] program.

The extracted thermodynamic information is shown in fig 5.1.1. The application of the constant pressure and temperature conditions can be clearly seen at 50 and 65 ps respectively.

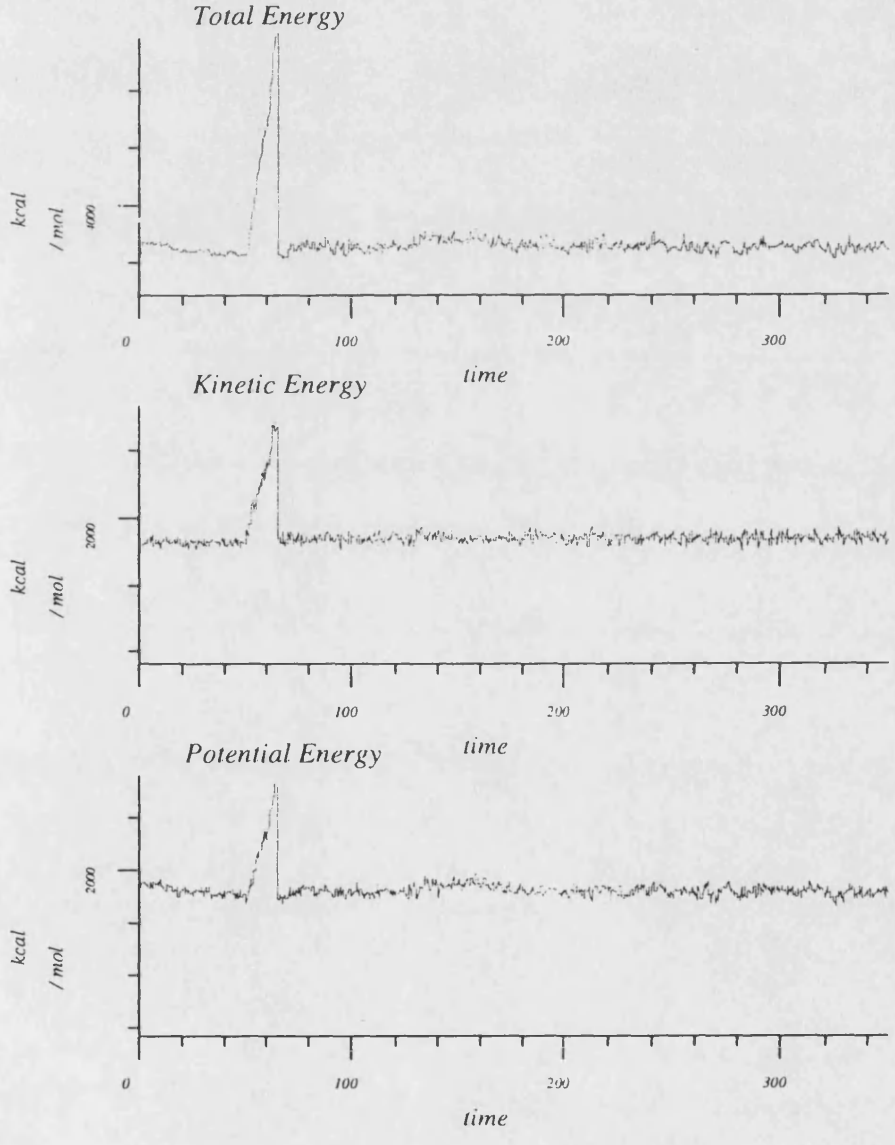


**Fig 5.1.1a** Potential, Kinetic and Total Energies for C5_1

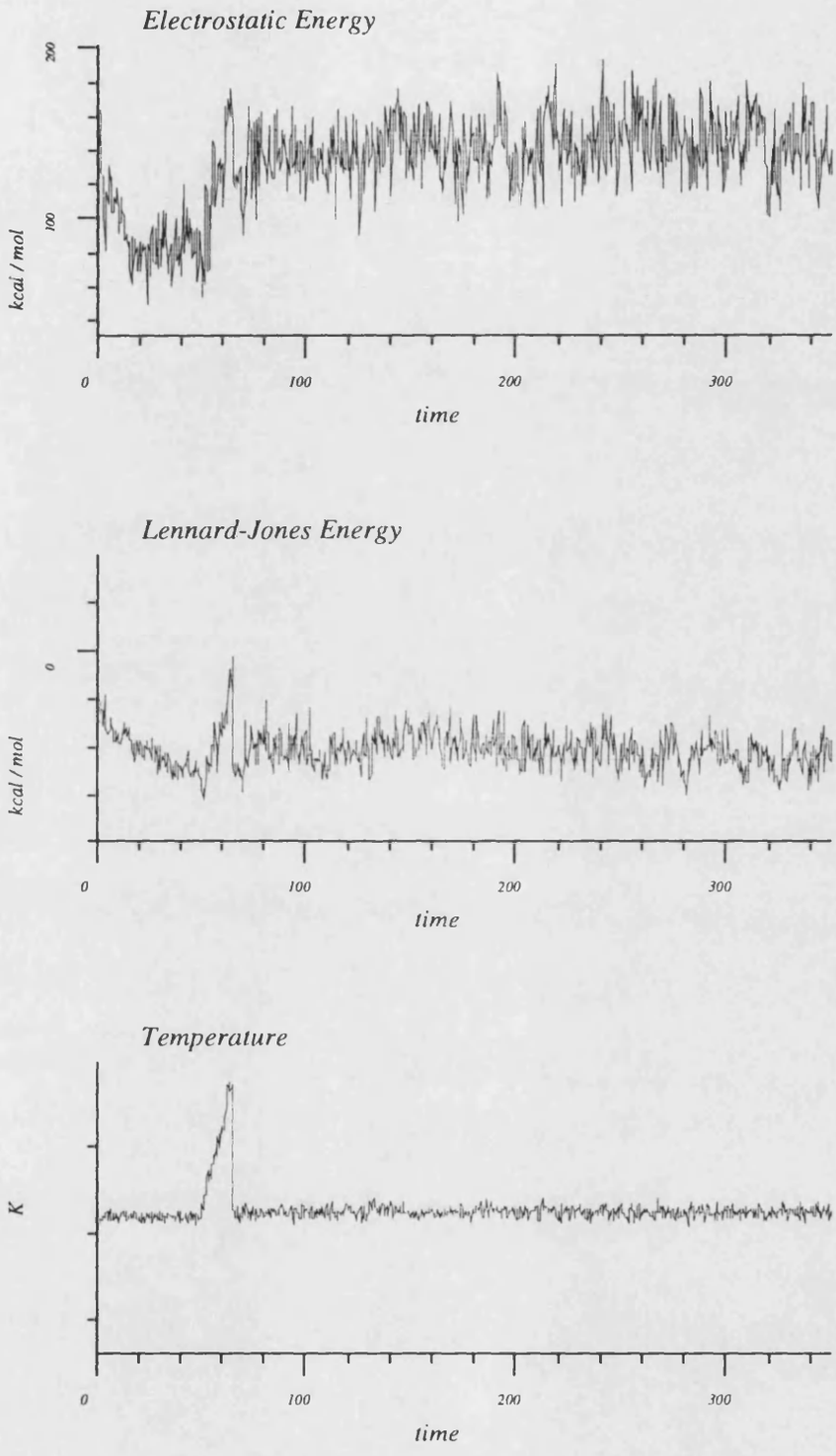


**Fig 5.1.1b** Electrostatic and Lennard-Jones Energies and Temperature Profiles for C5_1

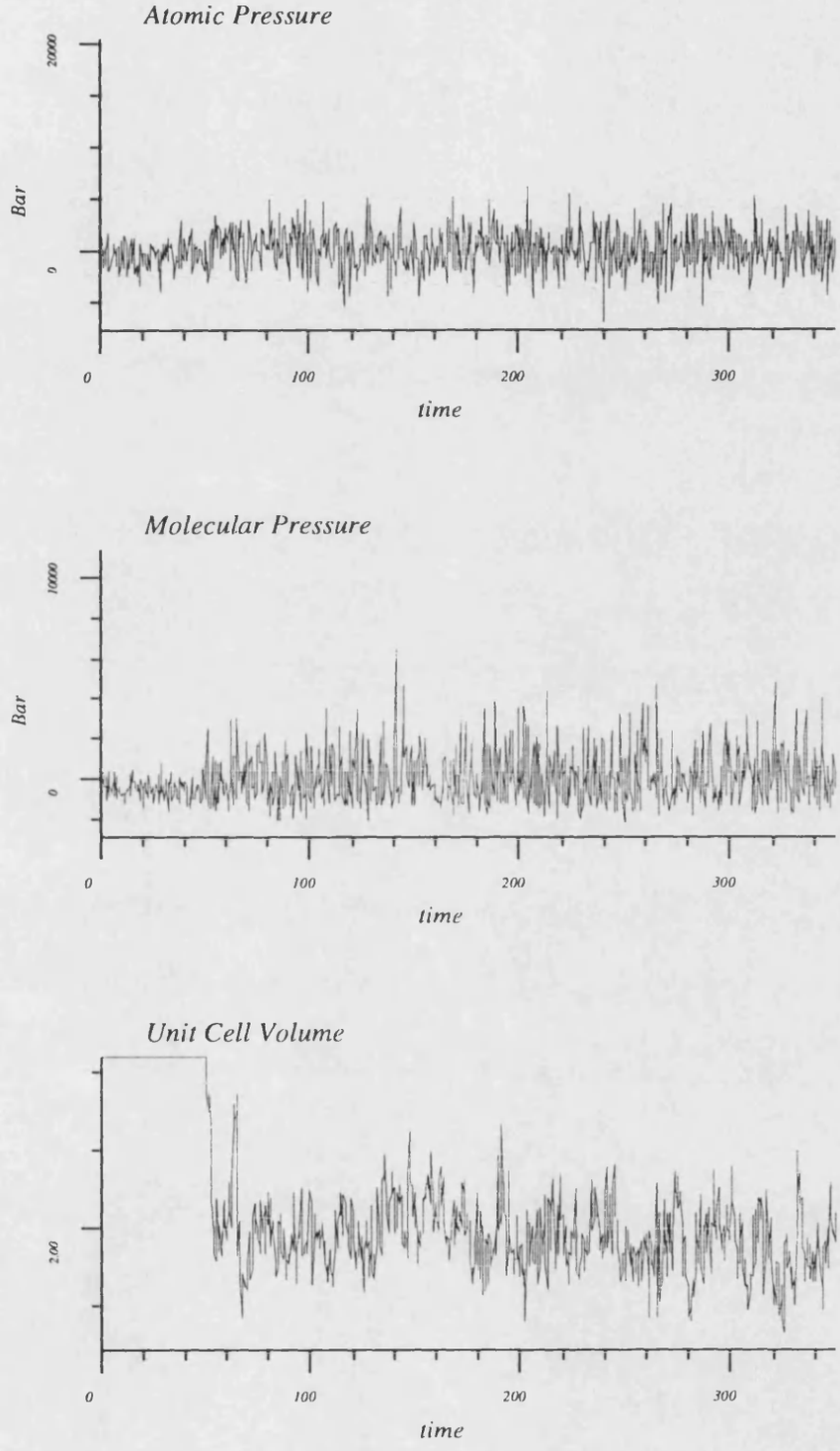


**Fig 5.1.1c** Unit Cell Volume, Molecular and Atomic Pressures for C5_1

The unit cell volume drops to approximately 90 % of its starting value as a consequence of the pressure bath scaling. This reduction was non-isotropic with the bilayer normal ( unit cell vector B, ucv B ) increasing by 4.2 % whilst the head group vectors ( ucv A and C ) drop by 10.9 % and 3.6 % respectively, table 5.1.1.

**Table 5.1.1** Unit cell dimension for C5_1

| Unit cell | Initial value | Average 100-350 ps | % Change |
|---|---|---|---|
| Vector A Å | 21.5 | 19.2 | – 10.9 |
| Vector B Å | 43.0 | 44.8 | 4.2 |
| Vector C Å | 24.0 | 23.1 | – 3.6 |
| Volume $Å^3$ | 22185 | 19851 | – 10.5 |

The molecular pressure appears to have reached equilibrium in terms of the pressure scaling algorithm after 50 ps of pressure scaling ( 100 ps ), with an average molecular pressure of 96.5 bar, whilst the atomic pressure is 1.2 bar. However the standard deviation of these values are so large as to make any interpretation of these values difficult, table 5.1.2.

**Table 5.1.2** Molecular and atomic pressures for C5_1

| Pressure bar | Average 100-350 ps | Standard Deviation |
|---|---|---|
| Molecular | 96.5 | 1416 |
| Atomic | 1.2 | 1943 |

Unit cell vectors A and C are seen to oscillate about an average of 19.2 Å and 23.1 Å, whilst the bilayer normal has an average of 44.8 Å.

The temperature of the system was scaled to 320 K, the average temperature of the system during the constant NVE stage of the simulation, before the constant pressure scaling was started. This resulted in an average temperature of 324.9 K. The relative stability's of the temperature and pressure scaling baths as shown by their standard deviations, table 5.1.3, is an indication of the correlation time for those baths and hence for the processes involved.

**Table 5.1.3** Molecular Pressure and Temperatures for C5_1

| | Average<br>100-350 ps | Standard<br>Deviation |
|---|---|---|
| Molecular Pressure<br>bar | 96.5 | 1416 |
| Temperature<br>K | 324.9 | 5.4 |

The temperature obviously has a small correlation time whilst the pressure scaling has a very much larger time, probably in the order of tens to hundreds of ps.

### 5.1.3 Analysis of 100 - 350 ps

For this period of the simulation the system appears to be fairly stable with only small oscillations seen in the unit cell vectors and volume about their average values, table 5.1.4.

**Table 5.1.4** Unit cell dimensions for C5_1 100-350 ps

| Unit cell | Average 100-350 ps | Standard Deviation |
|---|---|---|
| Vector A Á | 19.2 | 0.3 |
| Vector B Å | 44.8 | 1.0 |
| Vector C Å | 23.1 | 0.6 |
| Volume $Å^3$ | 19851 | 443.7 |

The kinetic energy is obviously very stable over this period due to the effect of the temperature bath. Thus the total energy fluctuations mirror the potential energy, however as can be seen from the standard deviations of the potential energy these fluctuations are relatively small, 47.7 kcal $mol^{-1}$, only a 2.7 % change. The stability of the scaled kinetic energy results in the temperature having a very small standard deviation of 5.4 K, 1.7 %, table 5.1.5.

The electrostatic and Lennard-Jones energies show a greater degree of fluctuation with larger standard deviations, 17.0 kcal $mol^{-1}$ ( 12.0 % ) and 35.1 kcal $mol^{-1}$ ( 16.9 % ) respectively. Some of this fluctuation can be accounted for by the pressure bath scaling, the effect of which can cause large changes in the Lennard-Jones energy when the co-ordinates are rescaled.

**Table 5.1.5** Energy components for C5_1, 100-350 ps

| Energy<br>kcal $mol^{-1}$ | Average<br>100-350 ps | Standard<br>Deviation |
|---|---|---|
| Total energy | 3644.8 | 45.8 |
| Potential energy | 1797.2 | 47.7 |
| Kinetic energy | 1847.6 | 30.7 |
| Electrostatic | 142.4 | 17.0 |
| Lennard-Jones | -208.5 | 35.1 |
| Temperature K | 324.9 | 5.4 |

The form of the potential energy plot of the system matches that of the Lennard-Jones energy. This may be a consequence of the pressure scaling, with the repositioning of the co-ordinates of each molecule causing direct changes in the intermolecular energies and hence affecting the overall potential energy of the system. This has been investigated by the use of Fourier transform techniques.

### 5.1.4 Fourier Transformations of Thermodynamic Data

The thermodynamic data for this section of the simulation, 100-350 ps, has been Fourier transformed to reveal any correlations within the data. The data is transformed from the time domain into the frequency domain. Any events that occur over a regular time span will appear at the frequency of that time period.

Digital signal processing techniques can be applied to the Fourier transformed data to remove frequencies that are not of interest, usually high frequency modes such as bond stretches and angles bends. This results in the removal of 'noise' from the property, this resultant property can then be back transformed into the time domain to give the low frequency 'noiseless' property. This enables the investigation of these low frequency motions, which are often conformational changes.

The Fourier transformed potential, kinetic, total, electrostatic and Lennard-Jones energies and the molecular pressure are shown in fig 5.1.2.

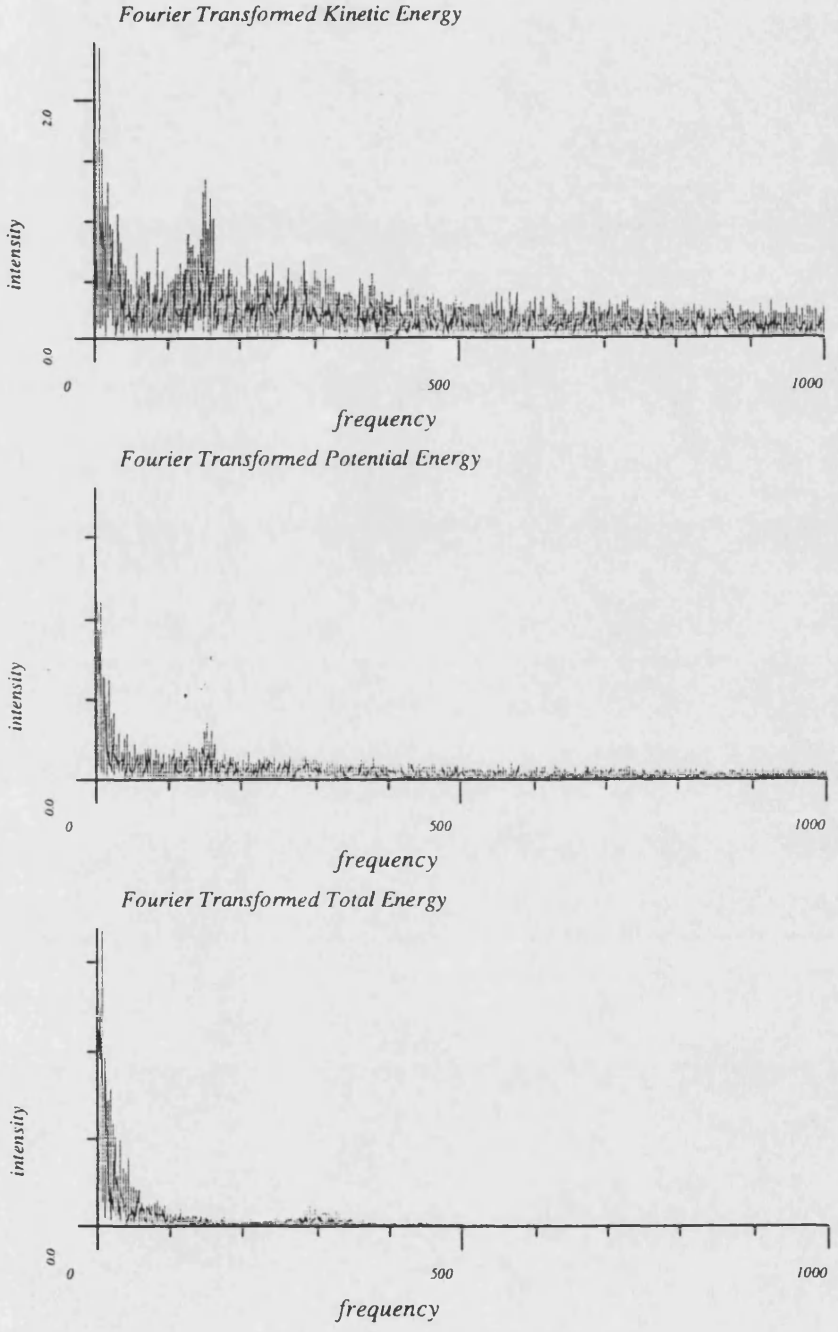


**Fig 5.1.2a** Fourier transformed Potential, Kinetic and Total Energies

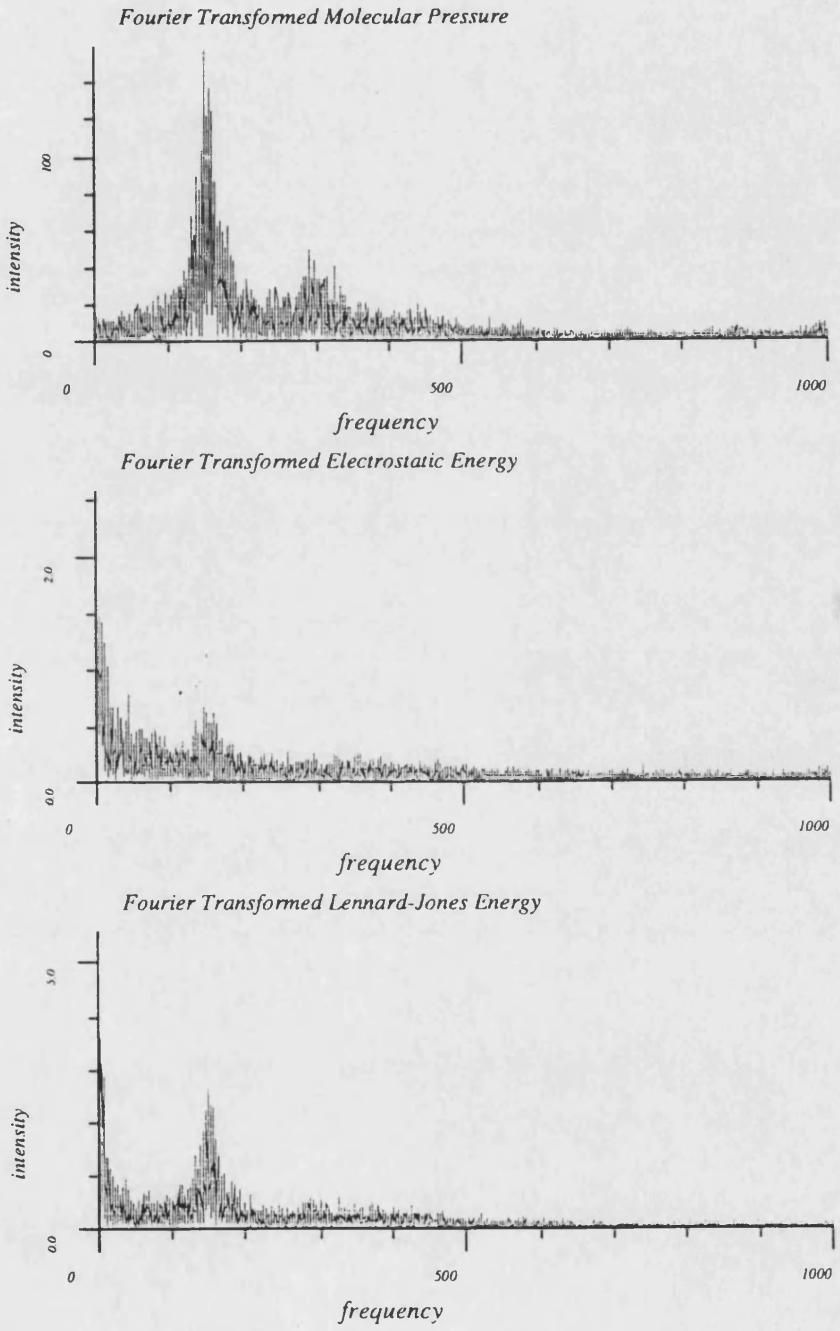


**Fig 5.1.2b** Fourier Transformed Electrostatic and Lennard-Jones Energies and Molecular Pressure

All of these plots have a dominant frequency around 160 $cm^{-1}$, this corresponds to a time period of ~220 fs. This is also the time constant for the constant pressure bath scaling, $t_p$.

The presence of this peak in the kinetic energy indicates that there is a high degree of coupling between the temperature and pressure. The peak at 160 $cm^{-1}$, seen in the molecular pressure, is also observed in the Fourier transform of the unit cell vector B and the component of the pressure tensor on the y-axis, fig 5.1.3, but is not as highly coupled with any other unit cell vector or component of the pressure tensor. This indicates that it is fluctuations in unit cell vector B, the bilayer normal, which dominate the pressure bath scaling, and hence the pressure of the whole system.

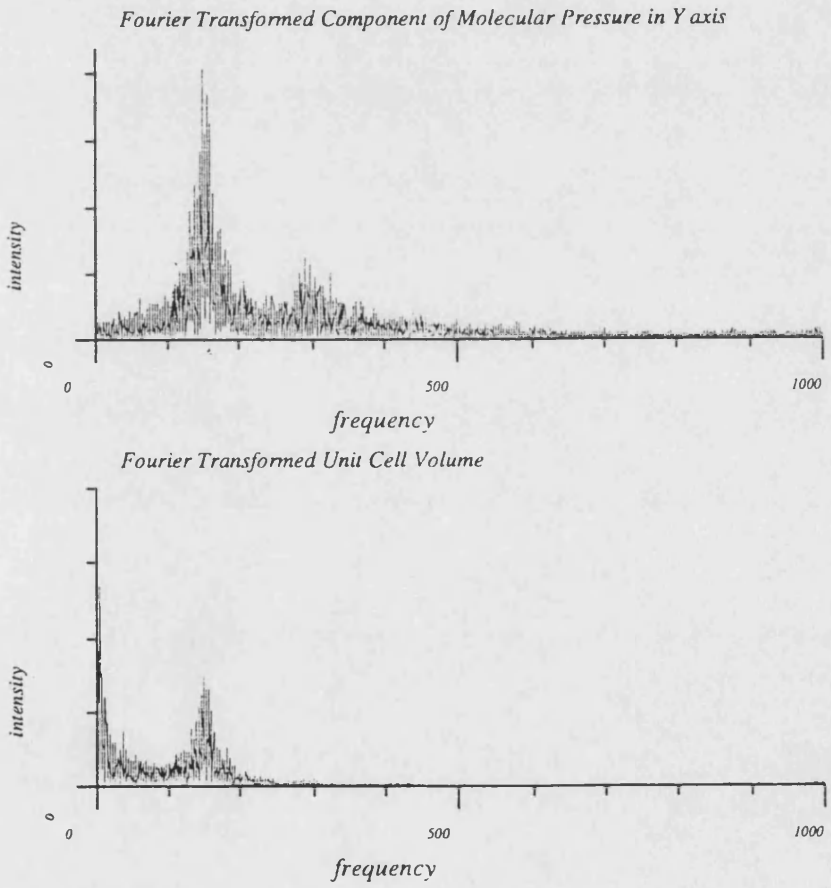


**Fig 5.1.3** Fourier transformed Unit Cell Vector B and Molecular Pressure Tensor Component along the Y axis

### 5.1.5 Filtering of Thermodynamic Data

The relationship between the potential and Lennard-Jones energies has been investigated further using filtering. The thermodynamic trajectory of this simulation has been Fourier transformed and high frequency modes have been removed using digital signal processing techniques to leave only low frequency motions. This is known as *filtering*[2]. The trajectory has been filtered to remove all frequencies above 20 $cm^{-1}$, thus retaining only the lowest frequencies of the system and then back transformed to the original time domain.

A graphical representation of the relationship between the potential and Lennard-Jones energies in this filtered trajectory is shown in fig 5.1.4, it can be seen that the form of the Lennard-Jones energy closely follows that of the potential energy.

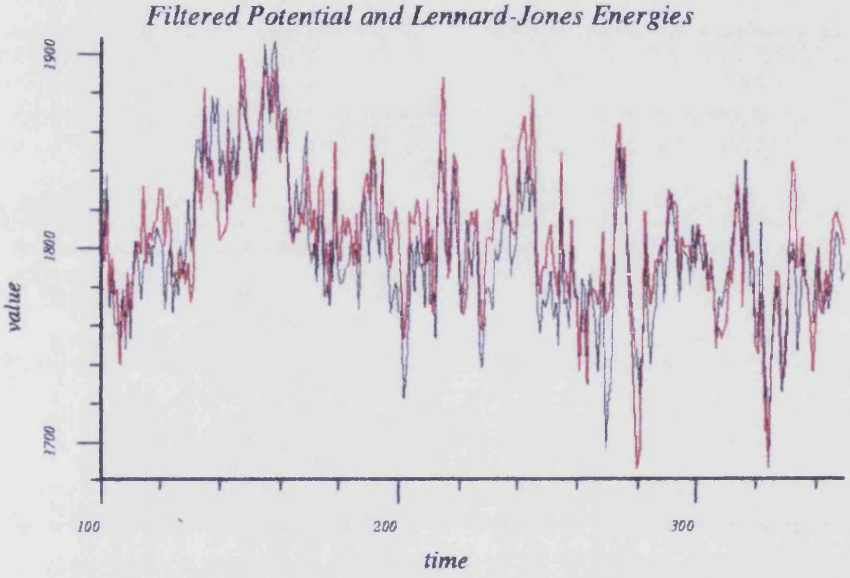


**Fig 5.1.4** Filtered Potential ( black ) and Lennard-Jones ( red ) Energies

This indicates that the fluctuations in the potential energy are dominated by changes in the Lennard-Jones energy. There is also a degree of correlation between the Lennard-Jones energy and the unit cell volume, thus changes in the unit cell volume, due to the pressure scaling, directly effect the Lennard-Jones energy and thus the potential energy. As there is no correlation between the internal energies and the potential energy, then the fluctuations in the Lennard-Jones energy are due to intermolecular interactions.

## 5.1.6 Analysis of Structural Data

Along with the thermodynamic data, the co-ordinates of all atoms within the unit cell are stored every 4 steps of the simulation. From these co-ordinates it is possible to calculate various structural properties including torsion angles and segmental order parameters.

### Acyl Chain Average Torsion Angles

The average values for the torsion angles defined in chapter 3 for the acyl chains are shown below in table 5.1.6.

**Table 5.1.6** Acyl chain average torsion angles

| | Average 100-350 ps | Standard Deviation | | Average 100-350 ps | Standard Deviation |
|---|---|---|---|---|---|
| $\phi_1$ | 452.5 | 249.8 | $\phi_{13}$ | 202.3 | 55.0 |
| $\phi_2$ | 202.9 | 42.5 | $\phi_{14}$ | 176.5 | 33.8 |
| $\phi_3$ | 207.5 | 56.4 | $\phi_{15}$ | 218.9 | 50.0 |
| $\phi_4$ | 180.8 | 27.8 | $\phi_{16}$ | 180.2 | 41.1 |
| $\phi_5$ | 177.4 | 47.1 | $\phi_{17}$ | 175.6 | 35.1 |
| $\phi_6$ | 179.1 | 24.8 | $\phi_{18}$ | 178.5 | 27.0 |
| $\phi_7$ | 182.1 | 31.6 | $\phi_{19}$ | 197.0 | 41.4 |
| $\phi_8$ | 176.6 | 33.4 | $\phi_{20}$ | 175.1 | 36.3 |
| $\phi_9$ | 177.8 | 37.3 | $\phi_{21}$ | 224.6 | 57.7 |
| $\phi_{10}$ | 181.6 | 39.2 | $\phi_{22}$ | 212.4 | 59.0 |
| $\phi_{11}$ | 254.7 | 69.1 | $\phi_{23}$ | 226.2 | 67.0 |
| $\phi_{12}$ | 225.6 | 83.1 | | | |

These values are a measure of the fluidity of the two acyl chains. For example the first torsion, $\phi_1$, has a very large standard deviation indicating that it is freely rotating. This in understood in terms of the change in volume effected by the rotation

of this torsion angle, the torsion is subtended from a double bond thus there will be little change in volume of the chain by rotating around this torsion, hence allowing free rotation. The end torsions of both chains, $\phi_{11\text{-}12}$ and $\phi_{21\text{-}23}$ show high degrees of rotational freedom compared with the rest of the chain. Their average torsion angles are more greatly diverged from the initial 180° starting conformation and in addition have larger standard deviations. This indicates that these torsion angles have a larger rotational movement compared to the rest of the chain, rather than the torsion has left the 180° minimum and moved to another local minimum with a small standard deviation. This is due to there being an increase in the free volume available to the lower torsions, due to a slight separation between the two monolayers.

In both chains the central torsions, $\phi_4$, $\phi_6$ and $\phi_{18}$ have considerably lower standard deviations than the rest of the chain and their average values have not deviated from the initial conformation. This indicates that there is some degree of rigidity within the acyl chain units and their interactions with the rest of the system. This prevents free rotation of these torsions and hence greatly reduces the actual free volume that the chain may occupy.

**Segmental Order Parameters**

The segmental order parameters for the two chains of the ceramide lipids have been calculated and are shown in fig 5.1.5.

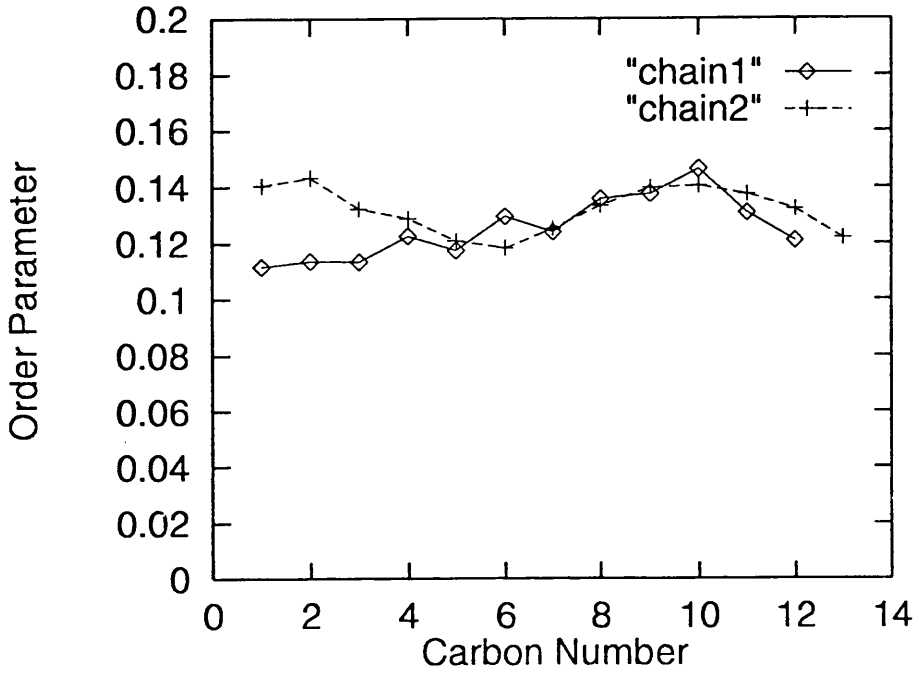


**Fig 5.1.5** Segmental Order Parameters for Chains 1 and 2 in C5_1

The segmental order parameters do not show the characteristic features normally associated with order profiles[3], both the profile for chain 1 and 2 are essentially flat until carbon 10 when they begin to decrease. This decrease in order parameter is expected, and confirmed by the increase in rotational freedom observed for the lower torsions, this decrease is also observed experimentally.

The torsion data indicated that $\phi_4$ and $\Theta_6$ in chain 1 and $\phi_{18}$ in chain 2 were less rotationally free than the other torsion angles, this is seen in the order parameters by the increase in value at carbon numbers 3 and 5 in chain 1 and 6 to 8 in chain 2.

The torsion data and the order parameter values indicate that the core of the bilayer does have some rotational freedom. The actually values for the order parameters indicates that the bilayer is quite fluid.

## 5.2.0 Ceramide 5 Bilayer with 1 Cholesterol, C5_2

The bilayer model C5_2, consisting of 17 ceramide 5 lipids and a single cholesterol molecule, was constructed using the bilayer constructed for simulation C5_1 as an initial template. The central ceramide molecule in the upper monolayer was removed and replaced by a cholesterol molecule using the Insight molecular modelling suite. The y-axis is still the bilayer normal, the x and z axes describing the head group plane.

Lattice points are separated by 7 Å in the x plane and 7 Å in the z plane. The resulting co-ordinates were minimised, until the total rms. derivative was below 0.5 kcal $mol^{-1}$ $Å^{-1}$. These minimised co-ordinates were used as the starting conformation for the molecular dynamics simulation.

### 5.2.1 Simulation Conditions

The molecular dynamics trajectory was sampled initially in the constant NVE ensemble for 60 ps, after which both the constant pressure and temperature baths were applied with the same target pressure and temperatures applied in the C5 simulation, i.e. 1 bar and 320 K. target pressure of 1 bar. The bilayer simulation was sampled under these constant temperature and pressure conditions for a further 290 ps.

## 5.2.2 Thermodynamics

The extracted thermodynamic information is shown in fig 5.2.1. The addition of constant pressure and temperature conditions can be clearly seen at 60 ps.

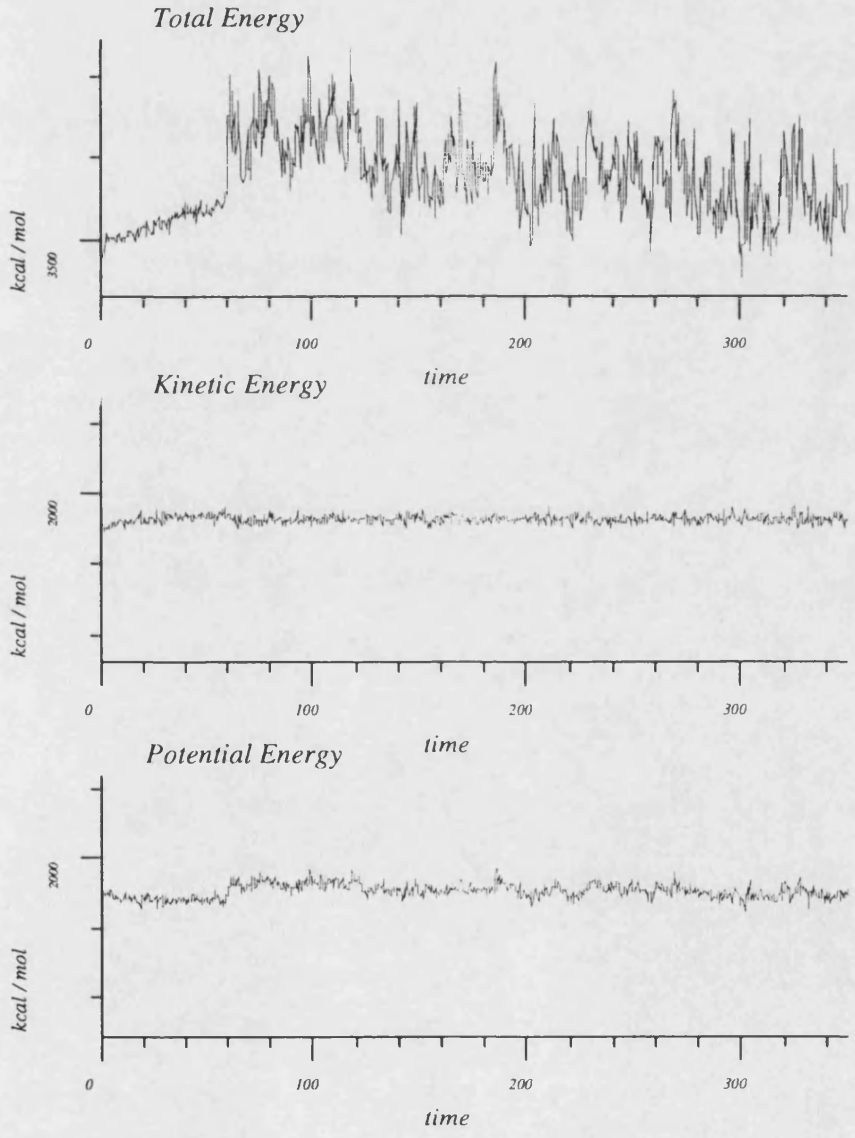


**Fig 5.2.1a** Potential, Kinetic and Total Energies for C5_2

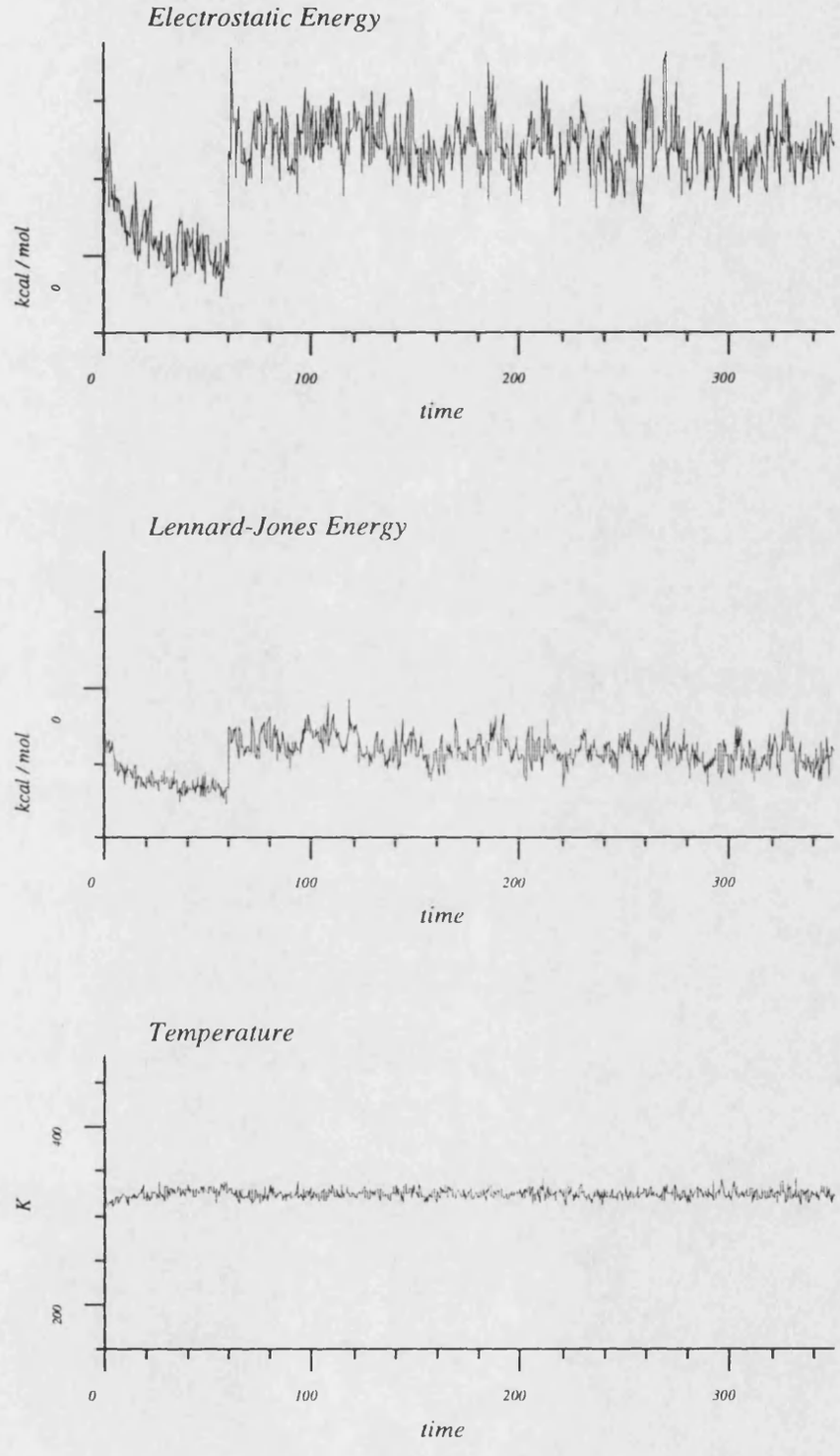


**Fig 5.2.1b** Electrostatic and Lennard-Jones Energies and Temperature Profiles for C5_2

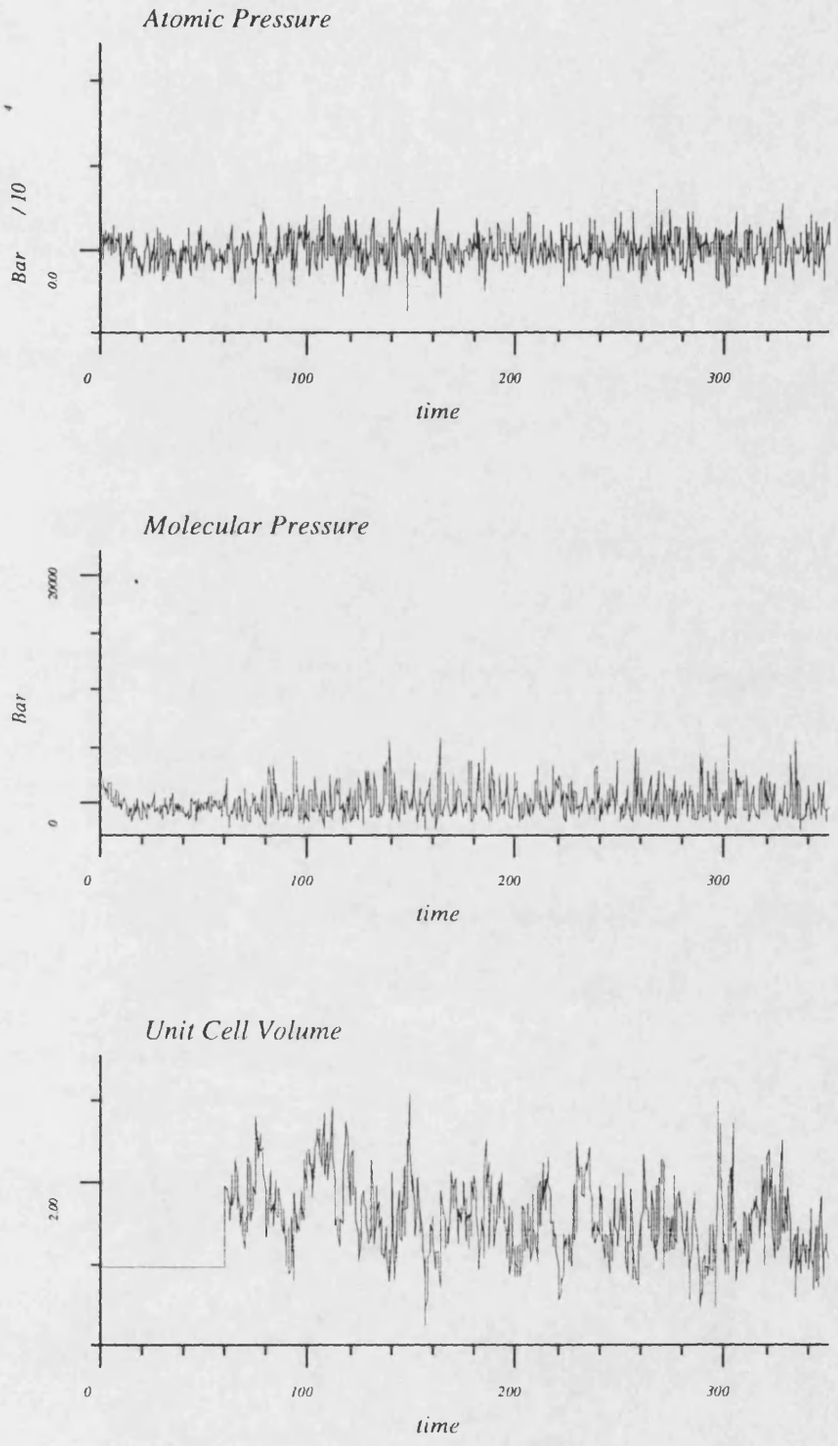


**Fig 5.2.1c** Unit Cell Volume, Molecular and Atomic Pressures for C5_2

The unit cell volume increases by approximately 3 % from its starting value as a consequence of the pressure bath scaling. This increase was non-isotropic with the bilayer normal ( unit cell vector B, ucv B ) increasing by 3 % and ucv C increasing by 9.6 % whilst the other head group vector ( ucv A ) decreased by 9 %, table 5.2.1.

**Table 5.2.1** Unit cell dimensions

| Unit cell | Initial value | Average 100-350 ps | % Change |
|---|---|---|---|
| Vector A Å | 21.0 | 23.0 | 9.6 |
| Vector B Å | 43.0 | 44.4 | 3.1 |
| Vector C Å | 21.0 | 19.1 | – 9.0 |
| Volume $Å^3$ | 18963 | 19523 | 2.9 |

The molecular pressure appears to have reached equilibrium in terms of the pressure scaling algorithm after 40 ps of pressure scaling ( 100 ps ), with an average molecular pressure of 97.1 bar, whilst the atomic pressure is 0.3 bar. However the standard deviation of these values are so large as to make any interpretation of these values difficult, table 5.2.2.

**Table 5.2.2** Molecular and Atomic Pressure

| Pressure bar | Average 100-350 ps | Standard Deviation |
|---|---|---|
| Molecular | 97.1 | 1409 |
| Atomic | 0.3 | 1900 |

Unit cell vectors A and C are seen to oscillate about an average of 23.0 Å and 19.1 Å, whilst the bilayer normal has an average of 44.4 Å.

The temperature of the system was scaled to 320 K, which resulted in an average temperature of 324.5 k.

The relative stability of the temperature and pressure scaling baths, as shown by their standard deviations, table 5.2.3, is an indication of the correlation time for those baths and hence for the processes involved. The temperature obviously has a small correlation time whilst the pressure scaling has a very much larger time, probably in the order of tens to hundreds of ps.

**Table 5.2.3** Molecular pressure and Temperature

| Parameter | Average<br>100-350 ps | Standard<br>Deviation |
|---|---|---|
| Temperature<br>K | 324.5 | 5.3 |
| Molecular pressure<br>bar | 97.1 | 1409 |

### 5.2.3 Analysis of 100 - 350 ps

For this period of the simulation the system appears to be fairly stable with only small oscillations about their average values seen in the unit cell vectors and volume.

**Table 5.2.4** Unit cell dimensions

| Unit cell | Average 100-350 ps | Standard Deviation |
|---|---|---|
| Vector A Å | 23.0 | 0.2 |
| Vector B Å | 44.4 | 1.0 |
| Vector C Å | 19.1 | 0.5 |
| Volume $Å^3$ | 19523 | 464.1 |

The kinetic energy is obviously very stable over this period due to the effect of the temperature bath. Thus the total energy mirrors the potential energy in its fluctuations and whilst the standard deviation is small 2.8 % there are some significant fluctuations seen, with a decrease in the overall potential energy of the system from 100 to 150 ps.

The electrostatic and Lennard-Jones energies show the same changes through the course of the simulation, essentially mirroring the potential energy. This fluctuation can be accounted for by the pressure bath scaling, the effect of which causes large changes in the Lennard-Jones energy when rescaling the co-ordinates.

**Table 5.2.5** Energy components

| Energy<br>kcal $mol^{-1}$ | Average<br>100-350 ps | Standard<br>Deviation |
|---|---|---|
| Total energy | 3578.7 | 45.4 |
| Potential energy | 1764.6 | 49.3 |
| Kinetic energy | 1814.2 | 29.6 |
| Electrostatic | 71.7 | 17.2 |
| Lennard-Jones | -169.8 | 35.4 |
| Temperature K | 324.5 | 5.3 |

The change in potential energy and the corresponding changes in the Lennard-Jones and electrostatic energies stem from changes in the unit cell volume which decreases slightly during the period from 100 to 150 ps. This is seen by the decrease in the head group ucv C from ~ 20 Å to 19 Å, and a smaller increase in the bilayer normal distance, ucv B.

The other head group vector, ucv A, remains essentially constant from 120 ps onwards with only minor deviations from its average, shown by a small standard deviation.

## 5.2.4 Fourier Transformation of Thermodynamic data

The thermodynamic trajectory for this section of the simulation, 100-350 ps, has been Fourier transformed in order to reveal any frequency correlations between the data. The plots for the total, potential and kinetic energies, those for the Lennard-Jones, electrostatic energies and the molecular pressure and the unit cell volume are shown in fig 5.2.2.

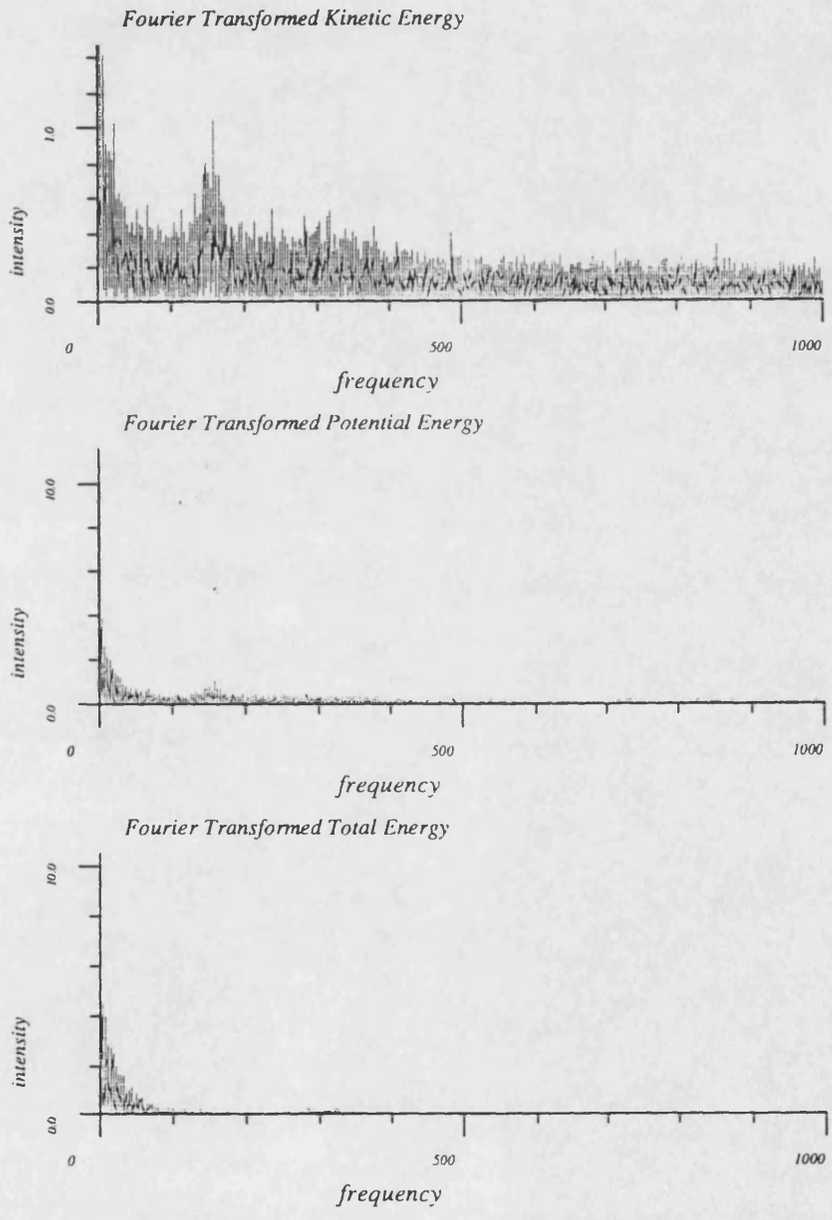


**Fig 5.2.2a** Fourier Transformed Potential, Kinetic and Total Energies.

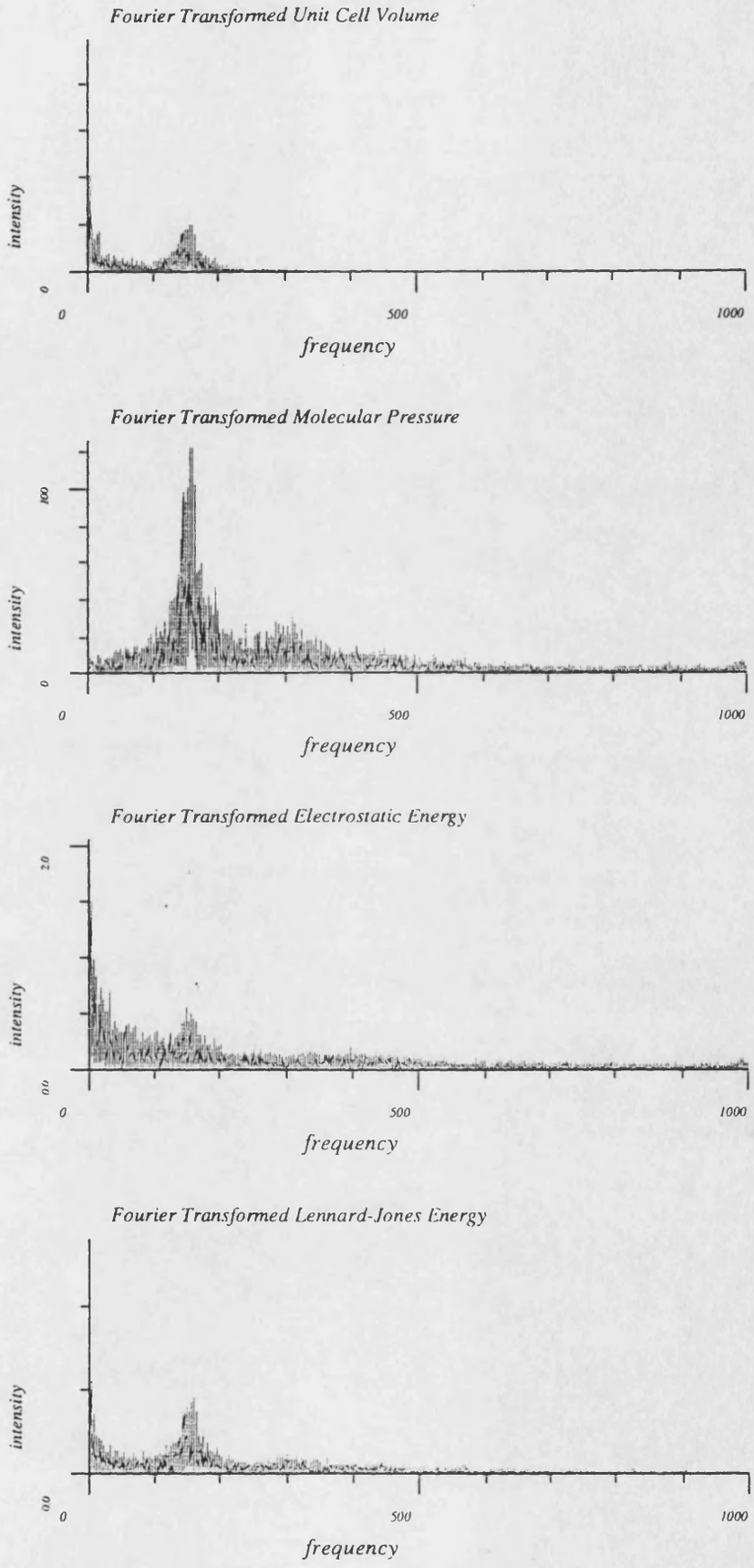


**Fig 5.2.2b** Fourier Transformed Electrostatic, Lennard-Jones Energies, Unit Cell Volume and Molecular Pressure.

It can be seen from these graphs that there is a dominant frequency in the kinetic energy and molecular pressure around 160 $cm^{-1}$, this peak is also seen in the Lennard-Jones, electrostatic energies and in the bilayer normal vector, ucv B.

This frequency corresponds to a motion on the time scale of ~ 220 ps, which is also the time constant of the pressure bath, $t_p$. This peak in both the kinetic energy and the molecular pressure indicates that there is a high degree of coupling between the temperature and pressure.

The presence of this peak in the Fourier transform of the bilayer normal, unit cell vector B, indicates a correlation between this property and the pressure. The absence of this peak in the other unit cell vectors indicates that it is this vector that is most influenced by the changes in the pressure, caused by the scaling algorithm. This relationship is further examined using the filtering techniques.

### 5.2.5 Filtering of Thermodynamic Data

The relationship between the potential and Lennard-Jones energies has been investigated using the filtering methodology[2].

A graphical representation of the relationship between the potential and Lennard-Jones energies in this filtered trajectory is shown in fig 5.2.3, it can be seen that the form of the Lennard-Jones energy closely follows that of the potential energy over the simulation.

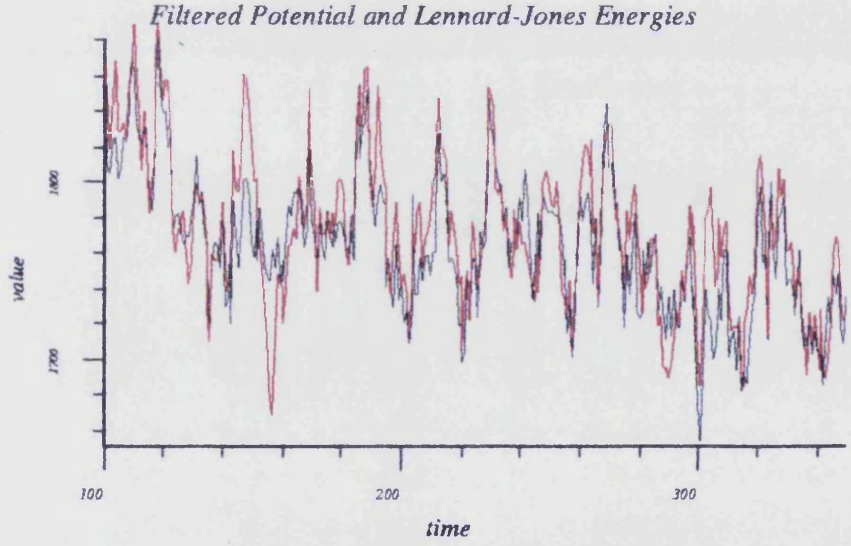


**Fig 5.2.3** Filter Potential ( black ) and Lennard-Jones ( red ) Energies

A correlation is also seen between the Lennard-Jones energy and the unit cell volume. The Fourier transform spectra also indicates that the Lennard-Jones energy and the unit cell volume were correlated to the pressure.

This filtering technique has been applied to all of the thermodynamic quantities stored on the trajectory to investigate any other relationships, which has revealed that the molecular pressure is directly correlated with the pressure in the y-axis, the bilayer normal, whilst not obviously with the other pressure axes. This correlation is also indicated by the coupling seen between the pressure and unit cell vector B from the Fourier transformed data. This indicates that pressure changes are caused by fluctuations in the bilayer normal and that these dominate the pressure, this may be an artefact of the constant pressure algorithm or it may be an indication of the least stable vector in the simulation.

## 5.2.6 Analysis of Structural Data

### Acyl Chain Average Torsion Angles

The average values for the torsion angles defined in chapter 3 for the acyl chains are shown below in table 5.2.6.

**Table 5.2.6** Acyl chain average torsion angles

| | Average 100-350 ps | Standard Deviation | | Average 100-350 ps | Standard Deviation |
|---|---|---|---|---|---|
| $\phi_1$ | 210.1 | 136.4 | $\phi_{13}$ | 177.5 | 39.7 |
| $\phi_2$ | 178.6 | 51.4 | $\phi_{14}$ | 180.9 | 28.8 |
| $\phi_3$ | 172.2 | 39.3 | $\phi_{15}$ | 173.3 | 40.0 |
| $\phi_4$ | 177.1 | 32.9 | $\phi_{16}$ | 182.0 | 24.4 |
| $\phi_5$ | 186.5 | 41.7 | $\phi_{17}$ | 171.6 | 37.7 |
| $\phi_6$ | 178.4 | 26.0 | $\phi_{18}$ | 180.8 | 26.4 |
| $\phi_7$ | 195.7 | 35.1 | $\phi_{19}$ | 180.5 | 30.2 |
| $\phi_8$ | 182.7 | 30.7 | $\phi_{20}$ | 181.0 | 28.0 |
| $\phi_9$ | 201.3 | 45.7 | $\phi_{21}$ | 174.1 | 41.2 |
| $\phi_{10}$ | 170.4 | 39.3 | $\phi_{22}$ | 177.1 | 62.3 |
| $\phi_{11}$ | 173.8 | 48.2 | $\phi_{23}$ | 195.2 | 59.3 |
| $\phi_{12}$ | 212.9 | 67.8 | | | |

The degree of fluidity within the bilayer is indicated by the average torsion angles and their standard deviations. The first torsion, $\phi_1$, in chain 1 has a large amount of rotational freedom and a standard deviation of greater than 50 %, this torsion is the first torsion of the chain after the double bond ( see chapter 3 ) and this structural arrangement allows it to rotate with greater freedom than the rest of the chain.

The terminal torsions in both chains, $\phi_{12}$, $\phi_{22}$ and $\phi_{23}$, also have high degrees of rotational freedom, with all of them having larger standard deviations than previous

torsions. This indicates that these torsions have a greater degree of conformational freedom compared to the rest of the bilayer. This conclusion agrees with the idea of the chain ends being slightly separated from each other, thus allowing them free volume in which to rotate.

There are several torsion angles which show a lower propensity to rotate than their surrounding torsions, $\phi_6$, $\phi_{16}$, $\phi_{18}$ and $\phi_{20}$. This indicates that there is some rigidity within the system due to intermolecular interactions which prevents all the torsion angles from rotating with the same degree of freedom, thus reducing the potential volume that the bilayer can occupy.

**Segmental Order Parameters**

The segmental order parameters for the two chains of the ceramide lipids have been calculated and are shown in fig 5.2.4

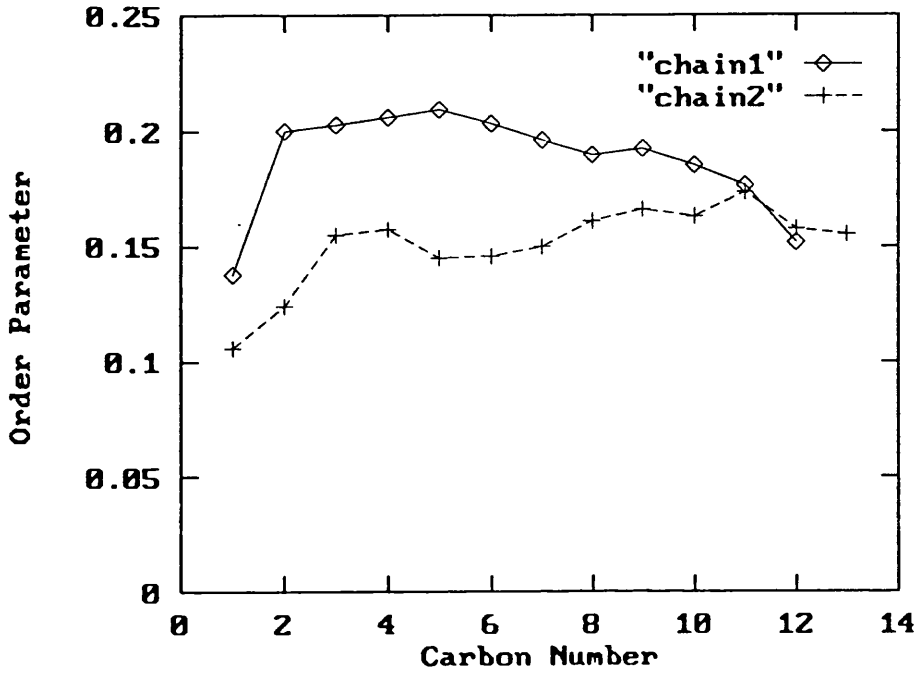


**Fig 5.2.4** Segmental Order Parameters for Chains 1 and 2 in C5_2

The segmental order profiles for the acyl chains shows the general characteristics followed by experimental order profiles[4], there being a characteristic plateau up to carbon atom number 8. However after carbon 8 the order parameters should decrease along the tails of the hydrophobic chains, this is observed in the order parameters for chain 1 but not for chain 2.

The values for chain 2 from carbon 3 downwards are essentially constant, indicating that the plateau of chain 2 continues out past carbon 8. Also chain 1 shows a slight dip at carbon 3 in agreement with experimental results, whereas chain 2 actually shows an increase. The torsion data indicates that $\phi_6$ in chain 1 and $\phi_{16}$, $\phi_{18}$ and $\phi_{20}$ in chain 2 have less rotational freedom than the rest of their respective chains. This is observed in the order parameters by increases in parameter values at carbon positions 3 to 4, 6 to 8 in chain 2. The actual values for the order parameters are within the error of those obtained experimentally.

## 5.3.0 Ceramide 5 Bilayer with a 3α-Cholesterol, C5_3

The bilayer model C5_3, consisting of 17 ceramide 5 lipids and a single 3α-cholesterol molecule, was constructed using the bilayer constructed for simulation C5_1 as an initial template. The central ceramide molecule in the upper monolayer was removed and replaced by a 3-α-cholesterol molecule using the Insight molecular modelling suite. The y-axis is still the bilayer normal and the x and z axes describing the head group plane.

Lattice points are separated by 8.2 Å in the x plane and 8.2 Å in the z plane. The resulting co-ordinates were minimised until the total rms. derivative was below 0.5 kcal $mol^{-1}$ $Å^{-1}$. These minimised co-ordinates were used as the starting conformation for the molecular dynamics simulation.

### 5.3.1 Simulation Conditions

The molecular dynamics trajectory was sampled initially in the constant NVE ensemble for 15 ps, after which a constant pressure bath was applied with a target pressure of 1 bar. After 30 ps a temperature bath of 306 K was applied due to the system beginning to increase in temperature in simulations that were continued past this stage without the bath applied. At 95 ps once the constant pressure appeared to have stabilised then the target temperature was raised to 320 K to be in agreement with the previous two simulations. The bilayer simulation was sampled under these constant temperature and pressure conditions for a further 250 ps.

## 5.3.2 Thermodynamics

The extracted thermodynamic information is shown in fig 5.3.1. The addition of constant pressure conditions can be clearly seen at 15 ps, the addition of a constant temperature bath at 30 ps and the change of target temperature at 95 ps.

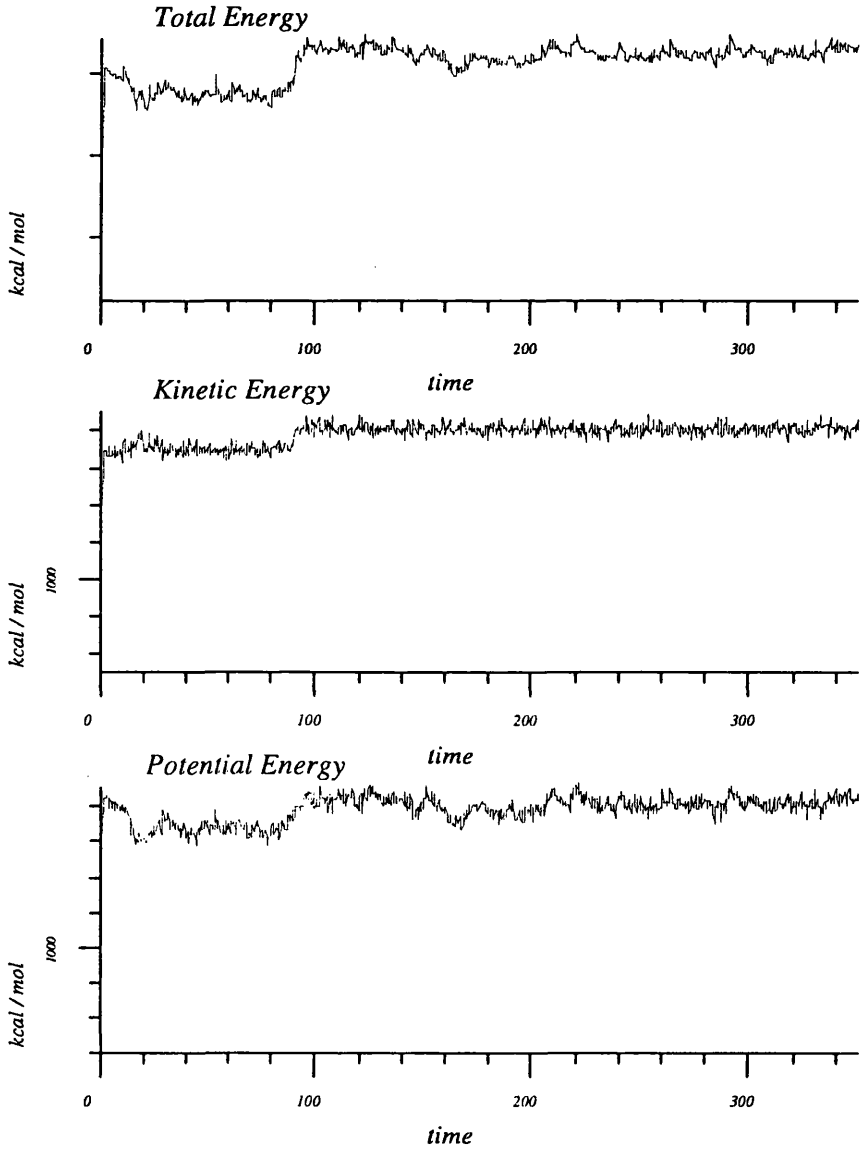


**Fig 5.3.1a** Potential, Kinetic and Total Energies for C5_3

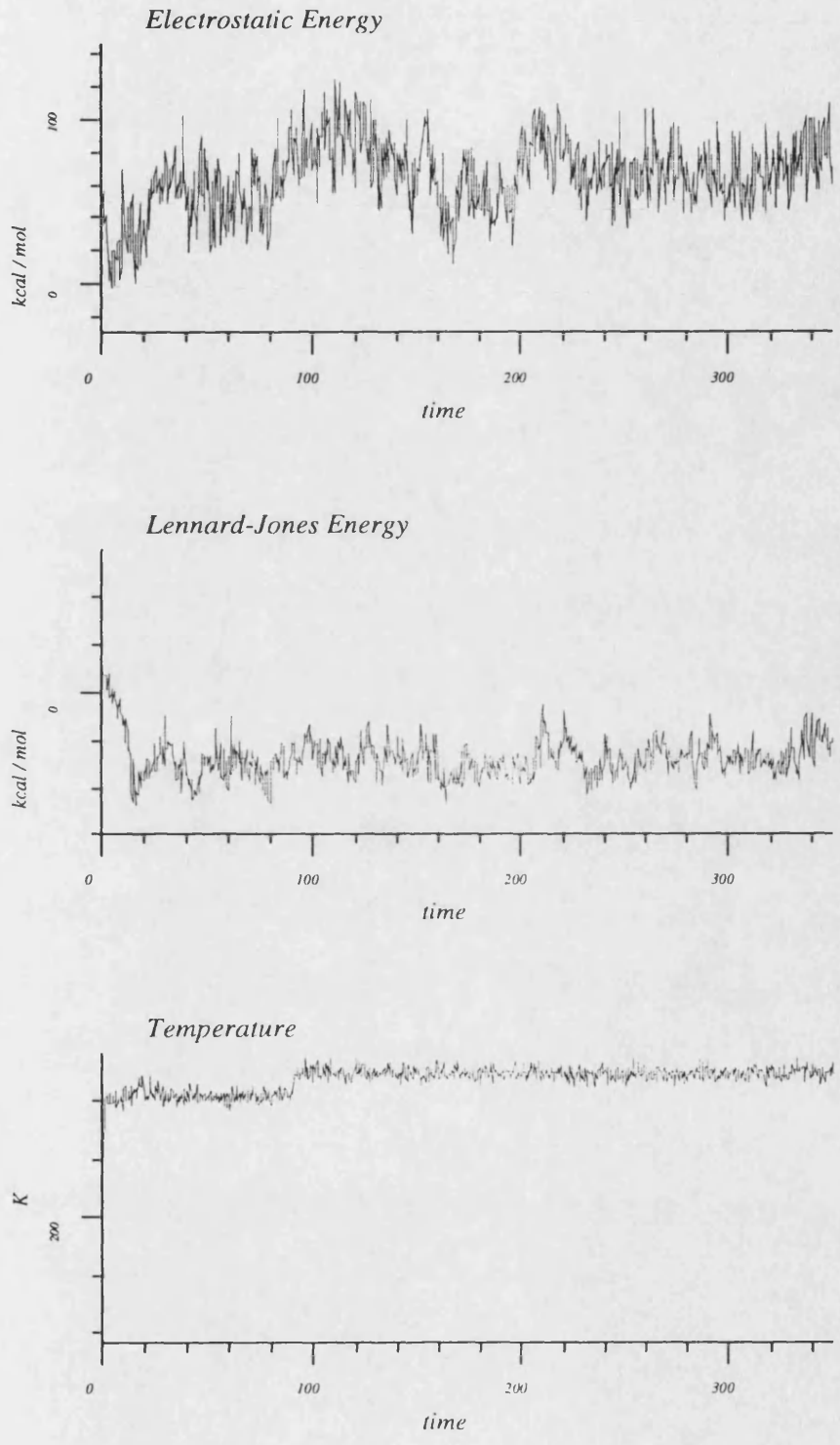


**Fig 5.3.1b** Electrostatic and Lennard-Jones Energies and Temperature Profiles for C5_3

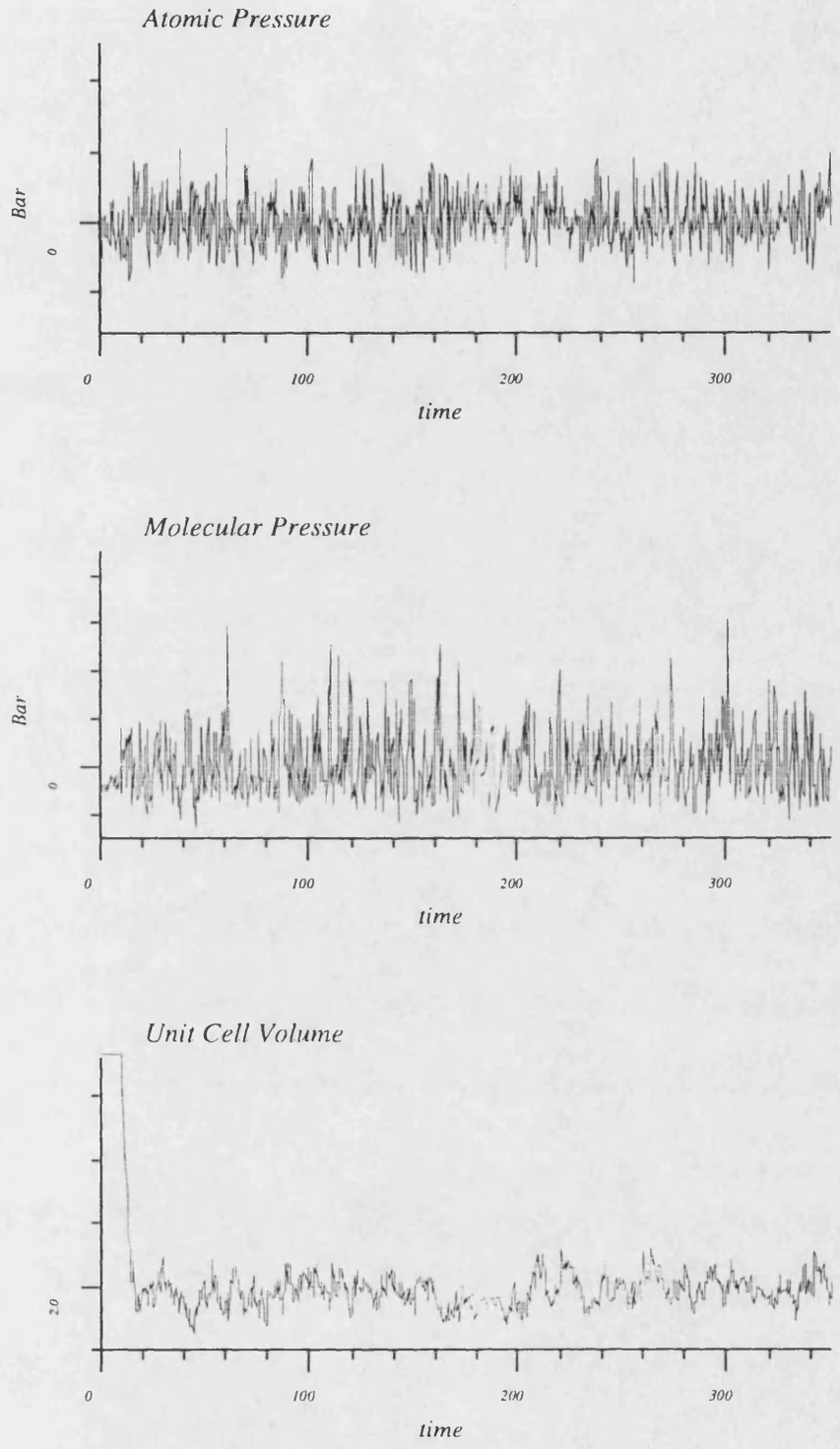


**Fig 5.3.1c** Unit Cell Volume, Molecular and Atomic Pressures for C5_3

The unit cell volume decreases by approximately 27 % from its starting value as a consequence of the pressure bath scaling. This increase was non-isotropic but all the unit cell vectors decreased, the bilayer normal, ucv B, by 4 % and the two head group vectors, ucv A and C, by 5 and 20 % respectively, table 5.3.1.

**Table 5.3.1** Unit cell dimensions

| Unit cell | Initial value | Average 100-350 ps | % Change |
|---|---|---|---|
| Vector A Å | 24.5 | 23.3 | – 5.0 |
| Vector B Å | 45.5 | 43.5 | – 4.3 |
| Vector C Å | 24.5 | 19.6 | –19.9 |
| Volume $Å^3$ | 27311 | 19893 | – 27.2 |

The molecular pressure appears to have reached equilibrium in terms of the pressure scaling algorithm after 85 ps of pressure scaling ( 100 ps ), with an average molecular pressure of 95.8 bar, whilst the atomic pressure is 1.5 bar, again the standard deviation of these values are so large as to make any interpretation of these values difficult, table 5.3.2.

**Table 5.3.2** Molecular and atomic pressure

| Pressure bar | Average 100-350 ps | Standard Deviation |
|---|---|---|
| Molecular | 95.8 | 1289 |
| Atomic | 1.5 | 1734 |

Unit cell vectors A and C are seen to oscillate about an average of 23.3 Å and 19.6 Å, whilst the bilayer normal has an average of 43.5 Å.

The temperature of the system was scaled to 320 K, which resulted in an average temperature of 323.6 K.

The relative stability of the temperature and pressure variables, as shown by their standard deviations, table 5.3.3, is an indication of the correlation time for those properties and hence for the processes involved. The temperature obviously has a small correlation time whilst the pressure scaling has a much larger time, probably of the order of tens to hundreds of ps.

**Table 5.3.3** Average molecular pressure and temperature

| Parameter | Average<br>100-350 ps | Standard<br>Deviation |
|---|---|---|
| Temperature<br>K | 323.6 | 5.0 |
| Molecular pressure<br>bar | 95.8 | 1289 |

### 5.3.3 Analysis of 100 - 350 ps

For this period of the simulation the system appears to be fairly stable with only small oscillations seen in the unit cell vectors and volume about their average values, table 5.3.4.

**Table 5.3.4** Unit cell dimensions

| Unit cell | Average 100-350 ps | Standard Deviation |
|---|---|---|
| Vector A Å | 23.3 | 0.3 |
| Vector B Å | 43.5 | 1.0 |
| Vector C Å | 19.6 | 0.3 |
| Volume $Å^3$ | 19893 | 452.5 |

The kinetic energy is obviously very stable over this period due to the effect of the temperature bath. Thus the total energy mirrors the potential energy in its fluctuations. Whilst the standard deviation is small, 2.5 %, there are some significant fluctuations seen, with a decrease in the kinetic energy from 150 to 165 ps and a rising back up again over the next 15 ps.

The electrostatic and Lennard-Jones energies show the same changes throughout the course of the simulation, mirroring the potential energy. Some of these fluctuations can be accounted for by the pressure bath scaling, the effect of which can cause large changes in the Lennard-Jones, table 5.3.5.

**Table 5.3.5** Energy components

| Energy<br>kcal $mol^{-1}$ | Average<br>100-350 ps | Standard<br>Deviation |
|---|---|---|
| Total energy | 3652.6 | 41.9 |
| Potential energy | 1816.2 | 45.5 |
| Kinetic energy | 1809.3 | 28.0 |
| Electrostatic | 69.6 | 18.5 |
| Lennard-Jones | -142.1 | 33.4 |
| Temperature K | 323.6 | 5.0 |

The change in potential energy and the corresponding changes in the Lennard-Jones and electrostatic energies stem from a marked reduction in the bilayer normal unit cell vector, ucv B, over the time period 150 to 160 ps. This vector slowly rises again but appears to be involved in a long time scale motion.

The head group vectors, ucv A and C, oscillate about their average values for the whole time period, but these are small fluctuations, shown by their small standard deviations, fig 5.3.2.

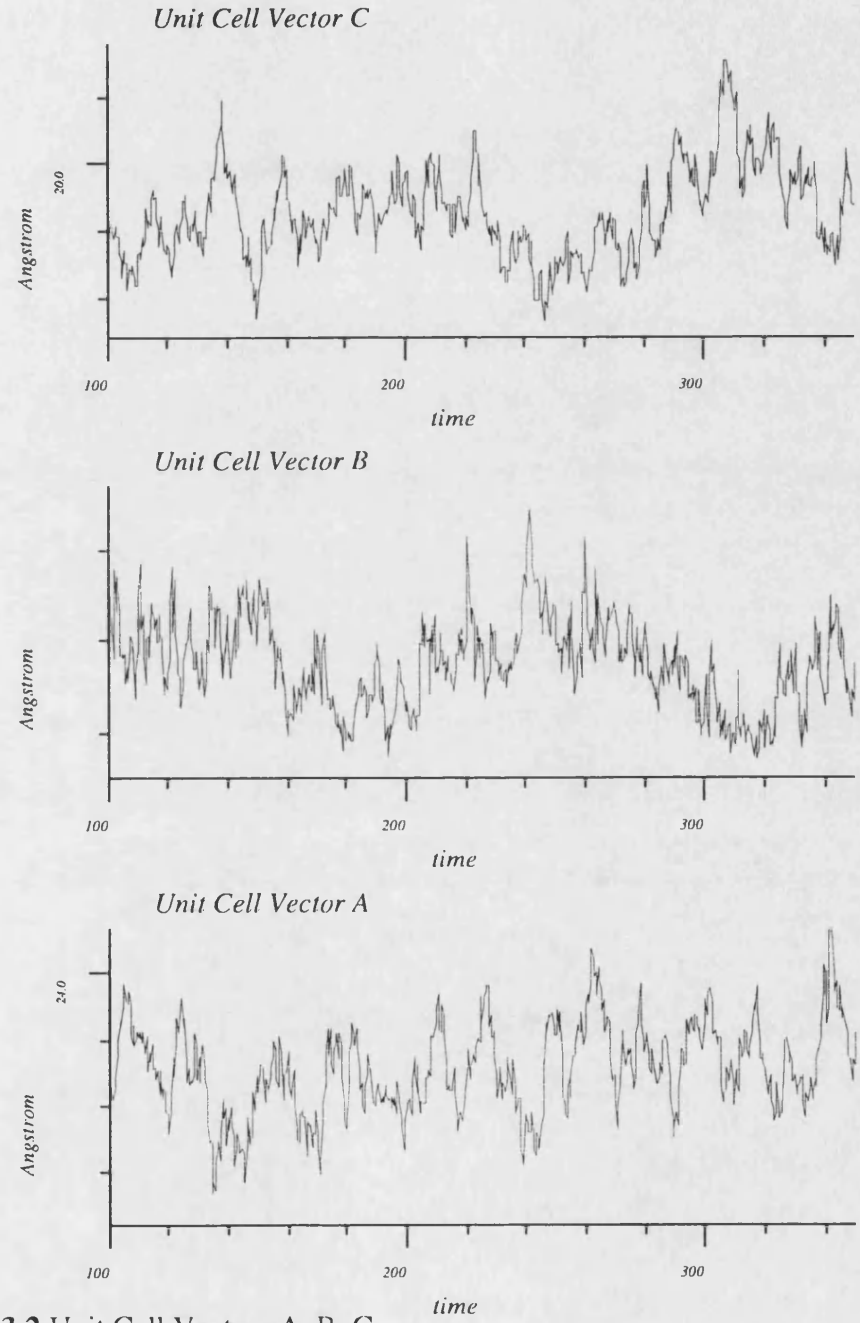


**Fig 5.3.2** Unit Cell Vectors A, B, C

### 5.3.4 Fourier Transformation of the Thermodynamic Data

The thermodynamic data for this part of the simulation, 100-350 ps, has been Fourier transformed to reveal any correlations within the data. The Fourier transformed potential, kinetic, total and Lennard-Jones energies and the molecular pressure are shown in fig 5.3.3.

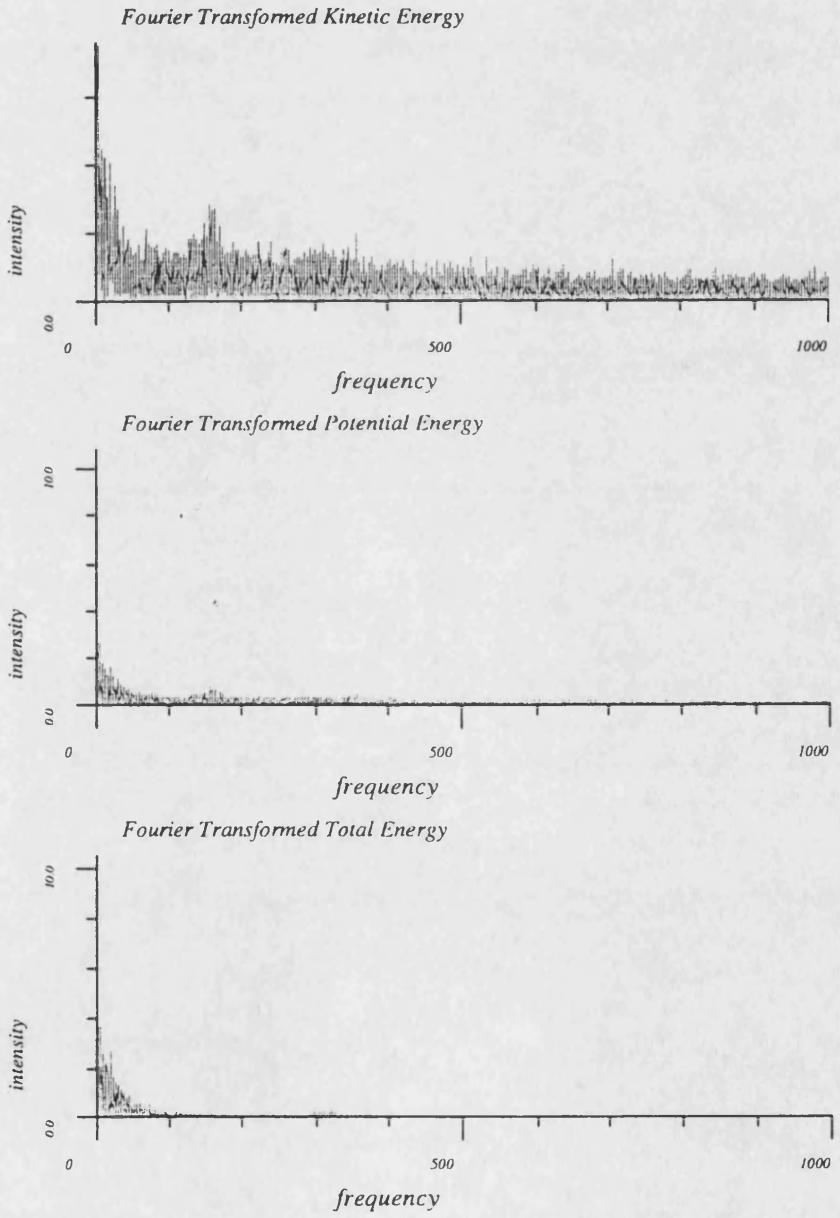


**Fig 5.3.3a** Fourier Transformed Potential, Kinetic and Total Energies

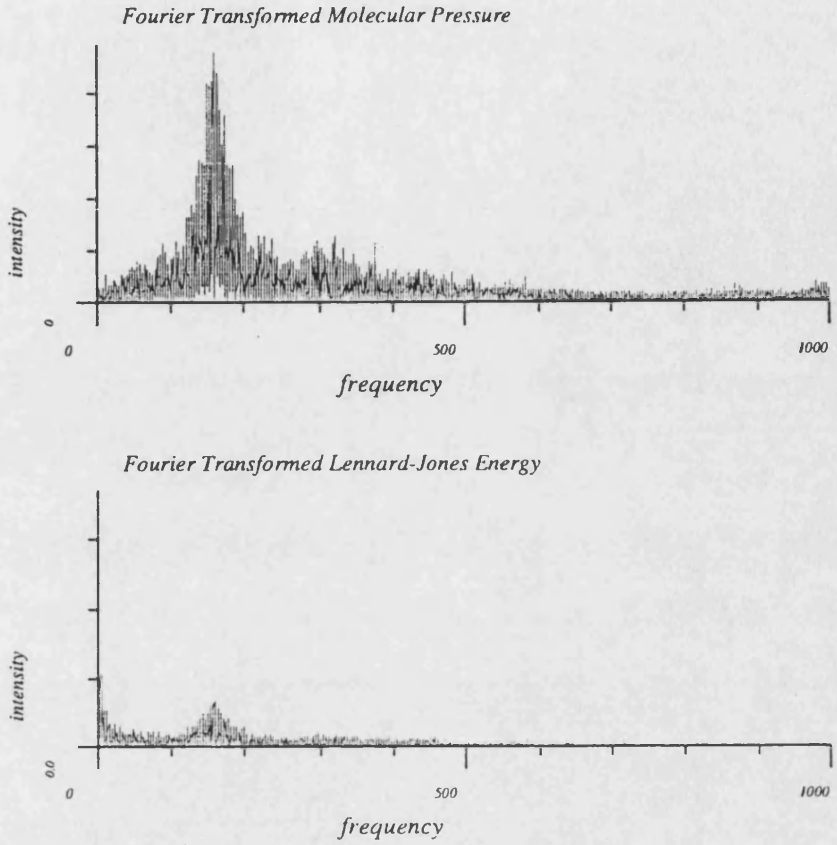


**Fig 5.3.3b** Fourier Transformed Lennard-Jones Energy and Molecular Pressure

The kinetic and Lennard-Jones energies and the molecular pressure all have a large dominant frequency around 160 $cm^{-1}$, which is also observed in the potential energy to a lesser extent. This corresponds to a time period for the frequency of ~220 fs, the time constant for the pressure bath scaling, $t_p$. The presence of this peak in the kinetic energy indicates that there is a high degree of coupling between the constant temperature and pressure baths.

This peak at 160 $cm^{-1}$ seen in the molecular pressure is also observed in the Fourier transform of the unit cell vector B, the component of the molecular pressure along the y-axis, fig 5.3.4, but not appreciably in any other unit cell vector or pressure.

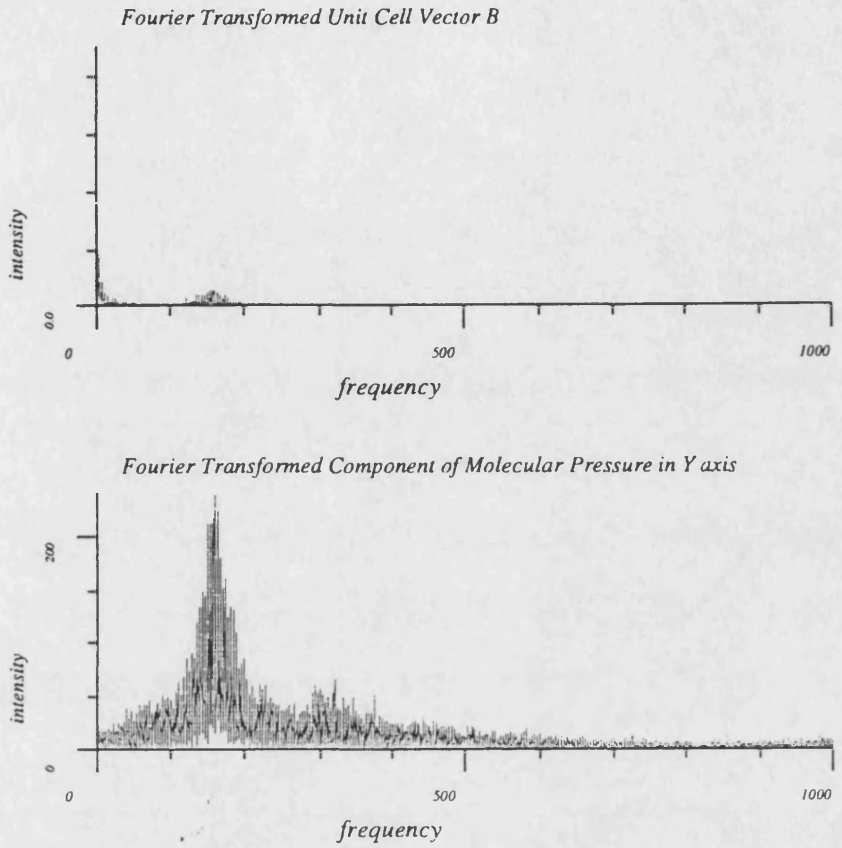


**Fig 5.3.4** Fourier Transformed Unit Cell Vector B and Component of the Molecular Pressure along the Y axis.

This indicates that it is fluctuations in the unit cell vector B, the bilayer normal, which are most highly correlated with the pressure scaling. This is observed as a characteristic breathing motion of the bilayer due to rearrangements along the bilayer normal.

**5.2.5 Filtering of Thermodynamic data**

The thermodynamic data has been filtered to remove all frequencies above 20 $cm^{-1}$, in order to investigate the correlation between the potential and Lennard-Jones energies.

The filtered potential and Lennard-Jones energies are shown on fig 5.3.5, this plot showing the high degree of correlation between these two energies.

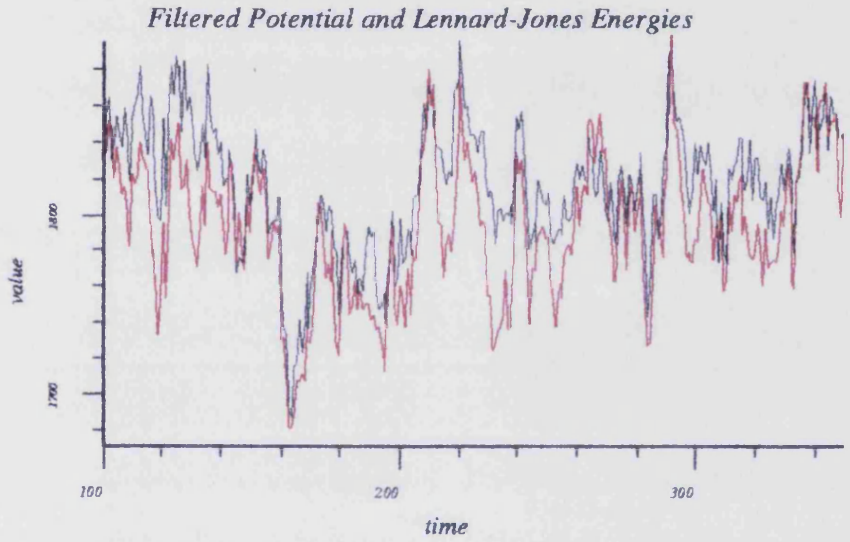


**Fig 5.3.5** Filtered Potential ( black ) and Lennard-Jones ( red ) Energies

This indicates that the potential energy is dominated by the Lennard-Jones energy. There is also a close correlation between the Lennard-Jones energy and the unit cell volume, indicating that the changes in unit cell volume, due to the pressure scaling, cause a corresponding change in the Lennard-Jones energy. This correlation is not seen between the internal energies and the potential energy showing that it is the inter-molecular non-bonded interactions, due to the changes in the unit cell volume, that dominate the potential energy.

## 5.3.6 Analysis of Structural Data

### Acyl Chain Average Torsion Angles

The average values for the torsion angles defined in chapter 3 for the acyl chains are shown below in table 5.3.7.

**Table 5.3.7** Average Acyl Chain Torsion Angles and Standard Deviations

| | Average 100-350 ps | Standard Deviation | | Average 100-350 ps | Standard Deviation |
|---|---|---|---|---|---|
| $\phi_1$ | 130.4 | 178.4 | $\phi_{13}$ | 195.9 | 50.9 |
| $\phi_2$ | 188.8 | 35.6 | $\phi_{14}$ | 179.6 | 29.6 |
| $\phi_3$ | 185.7 | 50.3 | $\phi_{15}$ | 185.9 | 41.8 |
| $\phi_4$ | 177.7 | 27.4 | $\phi_{16}$ | 181.4 | 29.8 |
| $\phi_5$ | 168.5 | 48.4 | $\phi_{17}$ | 181.8 | 33.9 |
| $\phi_6$ | 177.0 | 27.2 | $\phi_{18}$ | 188.9 | 44.7 |
| $\phi_7$ | 171.5 | 44.3 | $\phi_{19}$ | 171.1 | 39.1 |
| $\phi_8$ | 177.1 | 31.4 | $\phi_{20}$ | 192.4 | 48.4 |
| $\phi_9$ | 180.1 | 49.1 | $\phi_{21}$ | 181.6 | 42.2 |
| $\phi_{10}$ | 164.3 | 52.5 | $\phi_{22}$ | 192.5 | 57.3 |
| $\phi_{11}$ | 184.7 | 49.6 | $\phi_{23}$ | 190.4 | 53.9 |
| $\phi_{12}$ | 154.3 | 58.6 | | | |

The fluidity of the acyl chains is indicated by the average torsions angles and their standard deviations. The first torsion, $\phi_1$, in chain 1 has free rotation about it average value, with a standard deviation of 180°. This is the first torsion after the double bond ( see chapter 3 ) indicating that the structural constraints of this unit allow the torsion to freely rotate.

The terminal torsions of both chains, $\phi_{12}$, $\phi_{22}$ and $\phi_{23}$, also have a high degree of rotational freedom with large standard deviations and average values considerably different from the initial 180° starting conformation.

Within the acyl chains there are several torsions, $\phi_4$, $\phi_6$, $\phi_{14}$ and $\phi_{16}$, that have significantly smaller standard deviations and all these torsions oscillate around the initial starting conformation. This indicates that the intermolecular interactions within the bilayer prevent certain torsions from rotating as freely as the others and hence reducing the potential volume that the bilayer can occupy.

**Segmental Order Parameters**

The segmental order parameters for the two chains of the ceramide lipids have been calculated and are shown in fig 5.3.6.

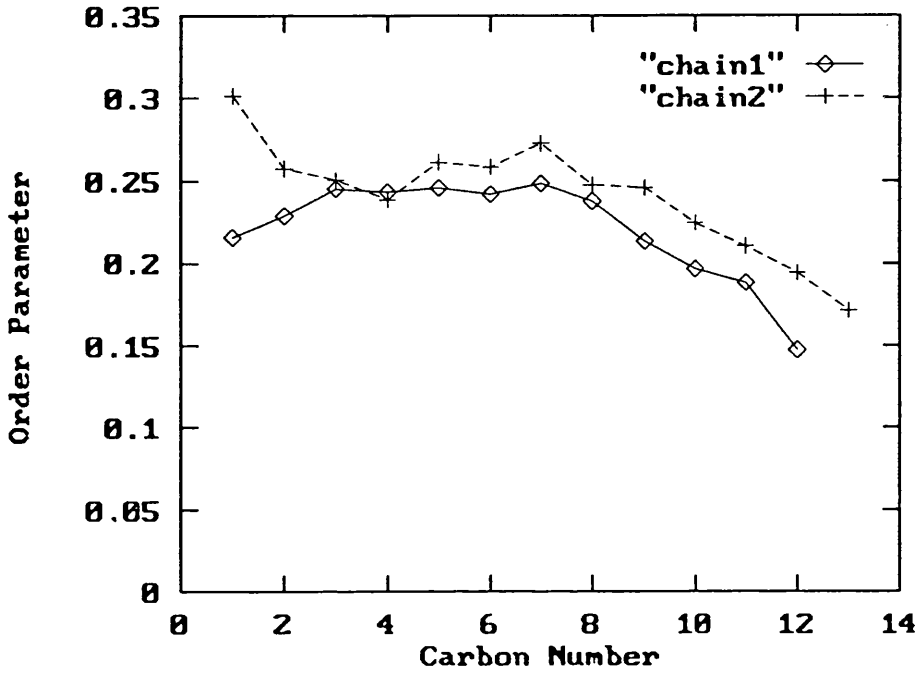


**Fig 5.3.6** Segmental Order Parameters for Chains 1 and 2 of C5_3.

The segmental order profiles for the two acyl chains for this simulation show the characteristic plateau of values until carbon number 8 and then the order parameters decrease along the tails of the hydrophobic chains.

Both chain profiles show a dip in value around the carbon 3 position in agreement with experimental results. This agrees with the torsion results, which show a lower standard deviation for $\phi_4$ and $\phi_6$ in chain 1 and $\phi_{14}$ and $\phi_{16}$ in chain 2 indicating that there is a loss of rotation around these carbon atoms.

The drop in order parameter values from carbon 8 downwards is in agreement with experimental results. This indicates that the bilayer becomes more fluid at the middle. This is explained in terms of a decrease in density at the middle of the bilayer which thus allows the terminal carbons more free volume in which to rotate.

## 5.4 Conclusions

These are the first bilayer simulations that have been performed upon skin lipids. The three lipid simulations presented differ from each other by the nature of the central molecule in one monolayer of the bilayer. Thus the first simulation investigated a pure ceramide 5 bilayer, but also acts as a 'control' for the two substitution experiments. In these the central lipid in one monolayer is replaced by one cholesterol moiety either 3-β-cholesterol, the native form, or 3-α-cholesterol, the hydroxyl isomer. These experiments probe the interaction of the these substituents with the bilayer and the affect they have upon the bilayer properties.

All three simulations are found to be stable over the sampled period, during which the system was under constant temperature and pressure bath conditions. Their potential energy profiles show only small standard deviations away from the average values. The kinetic energies are also very stable due to the presence of the temperature bath scaling, which in all three simulations had a target temperature of 320 K. The molecular and atomic pressures, however, in all three simulations had very large standard deviations, over an order of magnitude greater than their average molecular pressure. This is explained in terms of the long correlation time of the pressure in these systems, this correlation time appears to be in the order of 10's to 100's of picoseconds. Thus the scaling algorithm used with only a relatively short pressure time constant, $t_p$, has very large fluctuations.

### 5.4.1 Structural Aspects of Molecular Substitution

The effect of removing a central lipid and substituting it with different cholesterol moieties has a small effect upon the dimensions of the bilayer, table 5.4.1.

**Table 5.4.1** Unit cell dimensions for the ceramide 5 simulations

| Unit Cell | C5_1 | C5_2 | C5_3 |
|---|---|---|---|
| Vector A Å | 19.2 | 23.0 | 23.3 |
| Vector B Å | 44.8 | 44.4 | 43.5 |
| Vector C Å | 23.1 | 19.1 | 19.6 |
| Volume $Å^3$ | 19851 | 19523 | 19893 |

The use of the constant pressure bath has been to produce three very similar average unit cell dimensions. Indicating that cholesterol may be included into the bilayer without causing too great a disruption to the general packing arrangement of the lipid head groups.

The unit cell volumes have very small differences from each other and hence the average head group area per lipid for each simulation, table 5.4.2, these values are in good agreement with experimental results.

**Table 5.4.2** Volume change and Area per lipid for ceramide 5 simulations

| | C5_1 | C5_2 | C5_3 |
|---|---|---|---|
| % change in volume | 0 | – 1.7 | 0.2 |
| Head group area per lipid, $Å^2$ | 49.2 | 48.9 | 50.7 |

The torsion angles and the segmental order parameters for the acyl chains have been examined and these values are within the bounds of experimental results. The pure bilayer system reproduces the order parameter values for a fluid bilayer system but the actual shape of the profile is too flat. The lack of a significant drop in order parameter values from carbon number 8 downwards indicates that there is not an increase in rotational freedom near the centre of the bilayer. This increase in freedom is seen in experimental systems by the drop in order parameters. It is explained by the increased volume, that the terminal carbons have available to them in which to rotate. There is a drop in density at the centre of this bilayer and whilst the terminal carbons are more rotationally free than carbons further up the chain. The segmental order parameters themselves are compared against experimentally derived results, there is a significant difference in the time scales involved in these two experiments[5]. The profiles derived from NMR experiments are averaged over long time periods whilst the profiles presented here are from very shorter time periods and a much smaller system. Therefore it is not surprising that the results do not completely match those from experiment.

The influence of cholesterol upon the bilayer is to increase the order within the bilayer, the torsion angles have a decreased standard deviation compared to the pure bilayer system, indicating less rotational freedom. The order parameters also increase showing a loss of fluidity in the chains, i.e. a more ordered system. This is in agreement with experimental results where cholesterol is seen to reduce the fluidity of model membrane systems.

The affect of 3-α-cholesterol is in general similar to that of the native 3-β-cholesterol, however the system is marginally less stable. This system best reproduces the form of the segmental order parameters, with the drop in values from carbon 8 downwards. The α-steroids are natural membrane anaesthetics postulated to disrupt the membrane structure, this large scale behaviour is not seen in this simulation but this may be due to the short time scale of the simulation and the low concentration of the dopant molecule.

**5.4.2 Thermodynamic Results**

All three simulations show a direct correlation between the potential energy and Lennard-Jones energy. This is explained in terms of the pressure bath scaling algorithm, which scales the unit cell volume at every step, in order to keep the average pressure to the target pressure. This is achieved by scaling the co-ordinates and unit cell vectors either up or down to increase or decrease the volume correspondingly. The molecules within the unit cell are scaled by their centres of mass.

This does not affect the internal and intramolecular energies of molecules in the system but intermolecular energies will be affected and hence the potential energy. This was investigated by filtering the thermodynamic trajectories. Using digital signal processing techniques all frequencies above 20 $cm^{-1}$ were removed, leaving only the lowest frequency motions in the system. The removal of all high frequencies allows the investigation of conformational motion and energetics from the overall myriad of motions in the simulation.

This filtering revealed a correlation between the Lennard-Jones energy and the Unit cell volume, indicating that the changes in unit cell volume due to the pressure scaling cause changes in the Lennard-Jones energy.

The thermodynamic data has been Fourier transformed and in all three simulations a large dominant peak, around 160 $cm^{-1}$, has been found in the molecular pressure spectrum. This corresponds to a time of ~220 fs which is the time constant, $t_p$, for the pressure bath. The peak is also observed in the kinetic energy profile, indicating that there is a high degree of correlation between the pressure and the kinetic energy, this is explained by the definition of the pressure;

$$PV = NK_bT + \langle \omega \rangle \qquad \text{( eqn 5.1 )}$$

$$PV = N1/3 \langle \Sigma p_i^2 / m_i \rangle + \langle \omega \rangle \qquad \text{( eqn 5.2 )}$$

The ideal contribution to the pressure is derived from the kinetic energy and the virial term, $\omega$, is derived the gradient of the potential energy of the system, eqn 2.30. Hence in an NVE ensemble a increase in the pressure via a volume reduction will

result in the system gaining kinetic energy and the temperature rising, the effect of a piston compressing a gas.

In a constant temperature and pressure simulation both the pressure, P, and the kinetic energy, $\Sigma\ p^2\ /\ m$ , are constrained to oscillate around target values. However as stated earlier the time scales for their respective correlations to the system are very different. The temperature has a small correlation time, 10-100 fs, and can adjust more quickly to instantaneous perturbations to the system, whilst the pressure reacts over a much longer time scale. Thus instantaneous volume changes which over the course of the simulation will be adjusted to by all the variables are more quickly responded to by changes in the kinetic energy to compensate for the slow response time of the pressure. This results in the high degree of coupling seen between the pressure and temperature variables from the Fourier transform spectra. This high degree of correlation between the pressure and the temperature may be causing some instability in the system, which affects the constant temperature bath. This results in all three average temperatures being slightly higher than the target temperature of 320 K, but within one standard deviation of that target.

The instability is suspected to arise from the method of incorporating temperature and pressure baths simultaneously. The velocities and co-ordinates are both scaled simultaneously but independently, no account is taken of the other parameter when the scaling occurs. This appears to result in numerical instabilities. Any numerical instabilities in molecular dynamics algorithms tend to be seen as temperature increases, which of course a temperature bath will effectively hide. An increased instability could be reflected by the slightly higher average temperature of the system than the bath temperature. Such a difference is not seen in constant temperature simulations alone.

## 5.5 References

1 P.K.C. Paul, D.J. Osguthorpe and M.M. Campbell, Journal Of The Chemical Society-Perkin Transactions 1 (1990) 3363.

2 R.B. Sessions, D.J. Osguthorpe and P. Dauber-Osguthorpe, J. Phys. Chem. 99 (1995) 9034.

3 W. Abraham and D.T. Downing, Pharmaceutical Research 9 (1992) 1415.

4 F. Zhou and K. Schulten, J. Phys. Chem. 99 (1995) 2194.

5 A.J. Robinson, W.G. Richards, P.J. Thomas and M.M. Hann, Biophys. J. 67 (1994) 2345.

# CHAPTER 6

*CERAMIDE 4 SIMULATIONS*

## 6.0 Introduction

The two simulations presented in this chapter are concerned with a ceramide possessing asymmetric chain lengths. Thus, unlike the simulations reported in chapter 5, the lipids have to initially partially interdigitate in order to form the bilayer without creating areas of vacuum with no lipid. The two simulations that have been performed are

1. a pure ceramide 4 bilayer containing 18 lipids, C4_1,
2. a bilayer as in 1 where one central lipid from one monolayer has been replaced by one 3-β-cholesterol, C4_2.

The simulations have been investigated for their thermodynamic and structural properties over the period of the simulations. As in the previous investigations the central lipid in the top bilayer has been replaced with a cholesterol moiety and a simulation performed to investigate the influence of cholesterol upon the bilayer.

## 6.1 Pure Ceramide 4 Bilayer, Simulation , C4_1

A pure ceramide 4 bilayer, model C4_1, was constructed using the methodology described in chapter 3. Two ceramide 4 molecules were built and placed directly over each other in the bilayer conformation, using the Insight molecular modelling suite. This construct was aligned along the y - axis, now defined as the bilayer normal, using the *ALIGN* program. The bilayer was then built by replication in the head group axes, x and z. This resulted in an 18 lipid bilayer, consisting of two 3x3 monolayers.

The resulting co-ordinates were minimised, under periodic boundary conditions, until the total maximum derivative was less than 0.5 kcal $mol^{-1}$ $Å^{-1}$. The resulting unit cell had the following dimensions:

**Table** 6.01 Unit cell Dimensions

| Unit cell vector A | Unit cell vector B | Unit cell vector C | Unit cell angles $\alpha = \beta = \gamma$ | Unit cell Volume |
|---|---|---|---|---|
| Å | Å | Å | ° | $Å^3$ |
| 24.5 | 59.0 | 25.0 | 90 | 36138 |

This unit cell was used as the initial starting conformation for the molecular dynamics simulation.

### 6.1.1 Simulation Conditions

The molecular dynamics simulation was initially sampled in the constant NVE ensemble for 50 ps after which a constant temperature bath was applied, with a target average temperature of 320 K and a temperature bath time constant of 150 fs. The system was sampled under these constant temperature conditions for a further 300 ps.

### 6.1.2 Analysis of Thermodynamic Data

The thermodynamic data is stored on a trajectory history file every 4 steps of the simulation, this information was be extracted and manipulated using the FOCUS[1] program.

The extracted thermodynamic information for the whole simulation is shown in fig 6.1.1, the application of the temperature bath can clearly be seen at 50 ps. After this the potential appears to remain stable for the rest of the simulation.

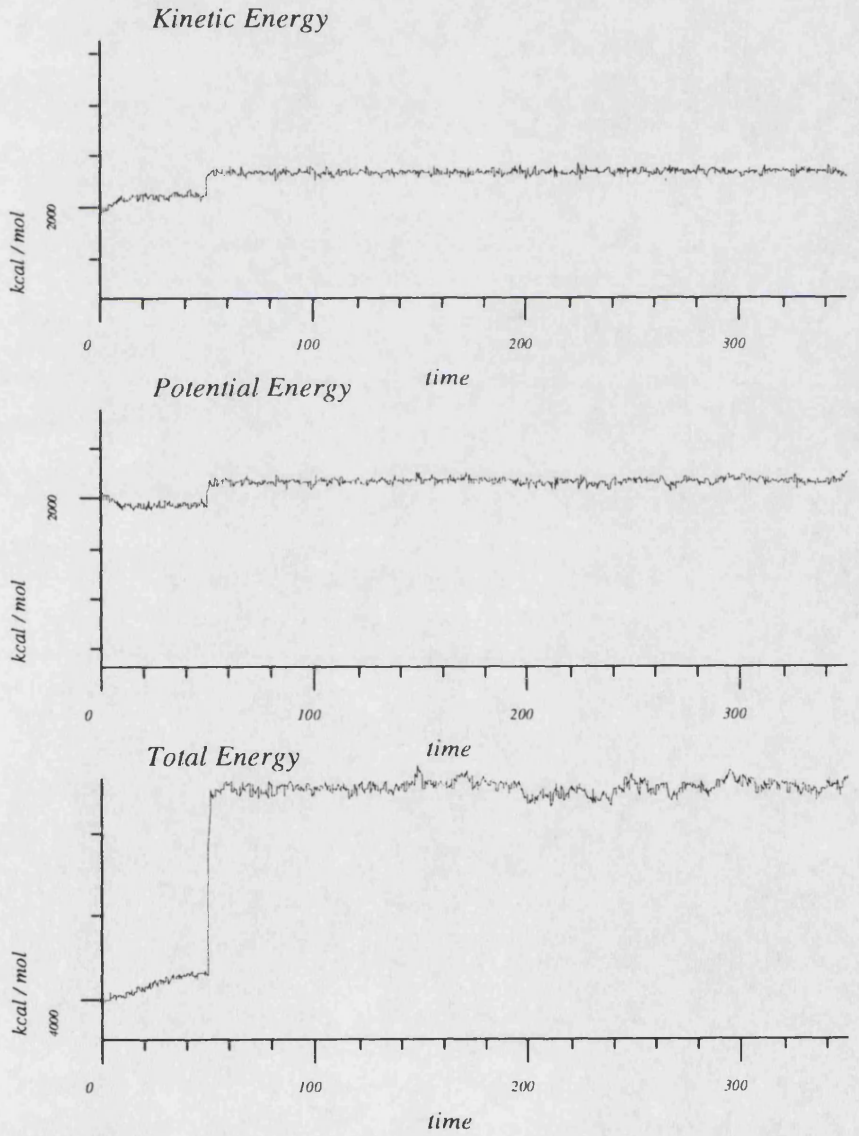


**Fig 6.1.1a** Potential, Kinetic and Total Energies for C4_1

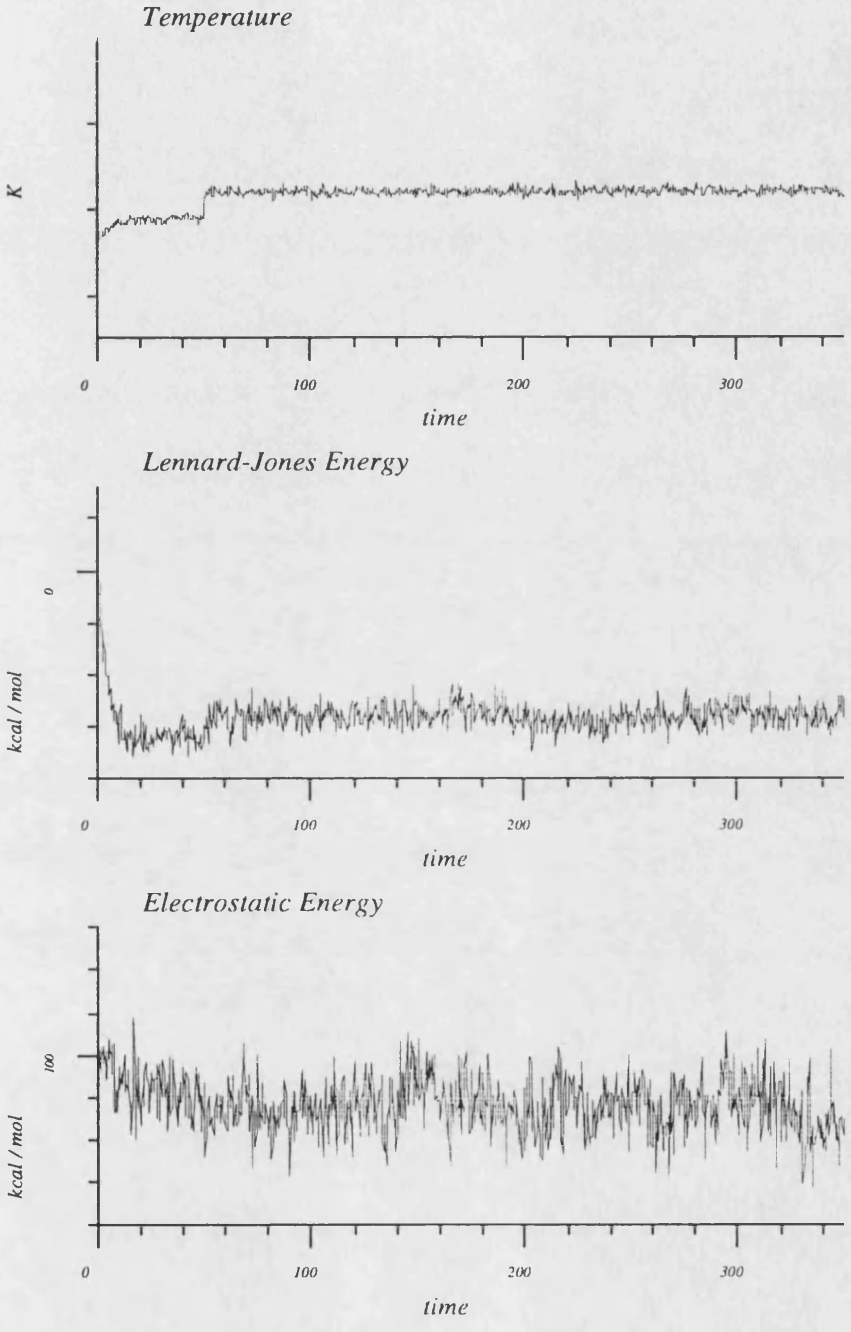


**Fig 6.1.1b** Electrostatic and Lennard-Jones Energies and Temperature Profiles for C4_1

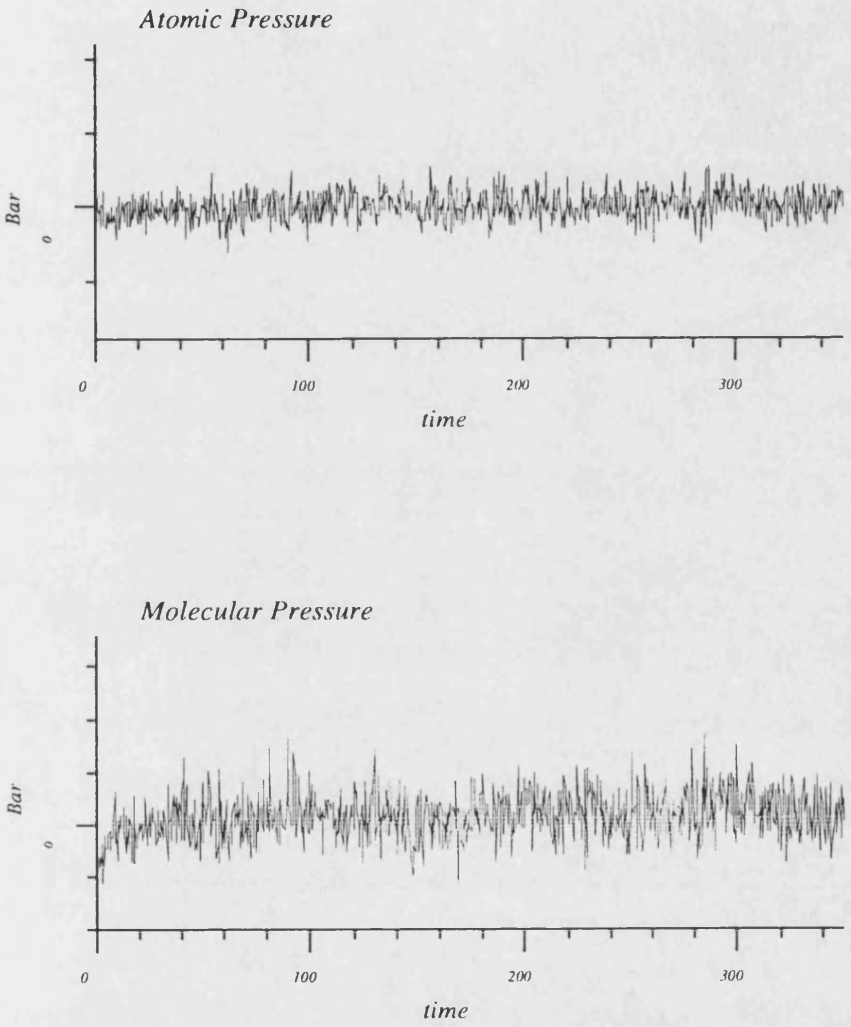


**Fig 6.1.1c** Atomic and Molecular Pressure for C4_1

The Lennard-Jones energy, fig 6.1.1, rises after the introduction of the temperature bath but levels out quickly, the electrostatic energy is less stable with larger fluctuations seen. The molecular and atomic pressures are relatively stable for

the simulation, there is a slight increase in the molecular pressure over the first 20 ps of the simulation after which it levels out.

### 6.1.3 Analysis of Thermodynamic Data 100 - 350 ps

Small oscillations are seen in the total energy plot, fig 6.1.2, for this time period.

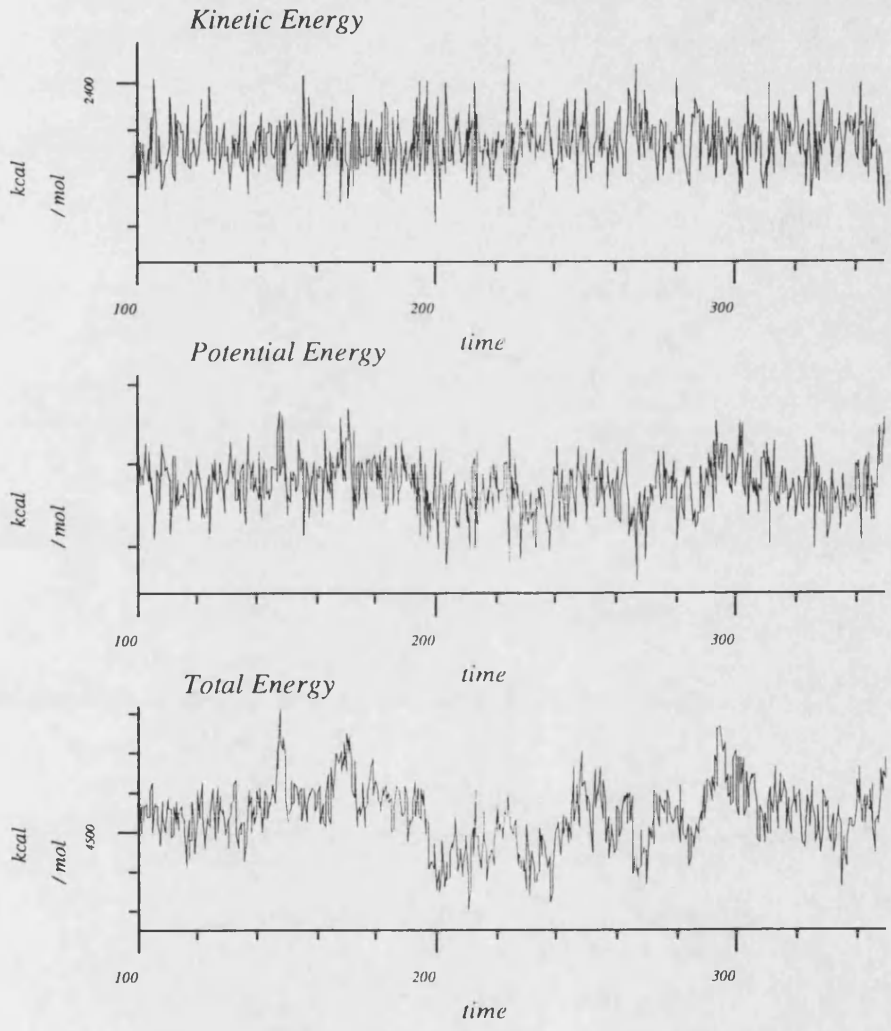


**Fig 6.1.2** Potential, Kinetic and Total Energies for C4_1, 100-350 ps

The standard deviations for this, the kinetic and potential energies are very small all less than 2 % of the total energy indicating that the system is very stable with regard to these energies, table 6.1.2.

**Table 6.1.2** Energy averages of C4_1

| Energy kcal $mol^{-1}$ | Average 100-350 ps | Standard Deviation | % |
|---|---|---|---|
| Total | 4508.9 | 16.3 | 0.4 |
| Kinetic | 2335.2 | 27.1 | 1.2 |
| Potential | 2173.7 | 32.1 | 1.5 |

These results show that the system is very stable for the period of the simulation with only small deviations away from the average. Larger deviations are seen in the Lennard-Jones and electrostatic energies, as expected there is only a small deviation in the temperature, table 6.1.3 and shown in fig 6.1.3.

**Table** 6.1.3

| Parameter | Average 100-350 ps | Standard Deviation | % |
|---|---|---|---|
| Lennard-Jones energy kcal $mol^{-1}$ | – 278.7 | 20.3 | 7.3 |
| Electrostatic energy kcal $mol^{-1}$ | 76.2 | 12.8 | 16.8 |
| Temperature K | 320.1 | 3.7 | 1.2 |

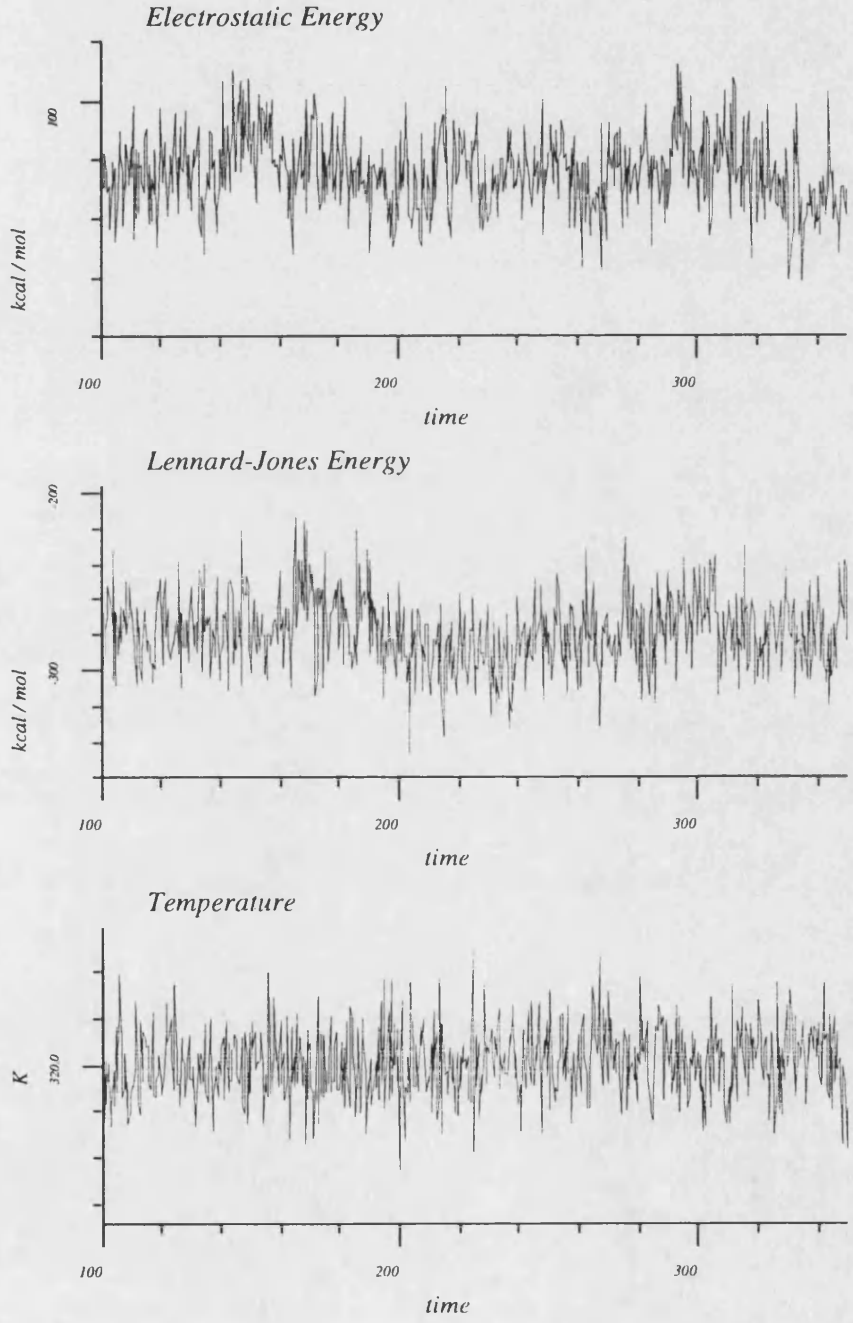


**Fig 6.1.3** Electrostatic and Lennard-Jones Energies and Temperature for period 100-350 ps.

There is no pressure scaling on this simulation, so the pressure is allowed to vary with the simulation conditions.

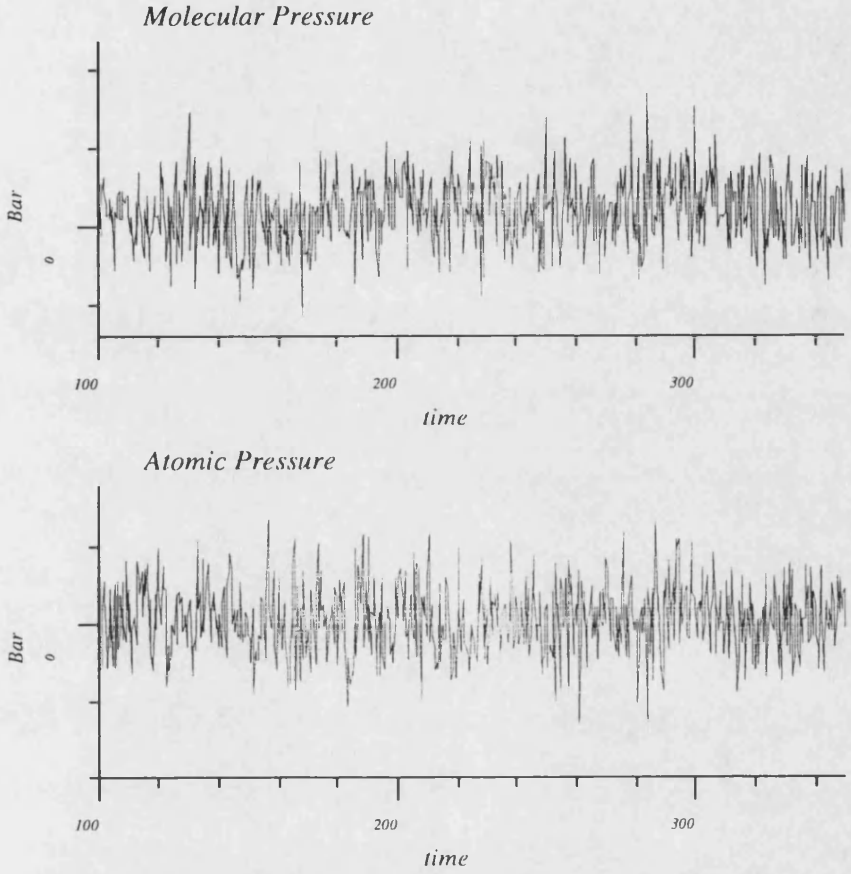


**Fig 6.1.4** Atomic and Molecular Pressure for time period 100-350 ps

As can be seen in fig 6.1.4 the molecular and atomic pressures appear to be very stable over the simulation, again however there is a very large standard deviation associated with both indicating the very long correlation times associated with this, table 6.1.4.

**Table 6.1.4** Atomic and molecular pressure

| Pressure bar | Average 100-350 ps | Standard Deviation |
|---|---|---|
| Atomic | 117.6 | 892.9 |
| Molecular | 191.7 | 435.2 |

The molecular and atomic pressure tensors along the axes are shown in table 6.1.5.

**Table 6.1.5** Unit cell pressure averages

| Component of Atomic pressure tensor along ( bar ) | Average 100-350 ps | Standard Deviation |
|---|---|---|
| X axis | – 100.0 | 1278.8 |
| Y axis | 268.1 | 1509.9 |
| Z axis | 185.2 | 1312.9 |
| Component of Molecular pressure tensor along ( bar ) | | |
| X axis | -13.0 | 330.9 |
| Y axis | 304.3 | 1055.8 |
| Z axis | 284.0 | 533.8 |

The standard deviations seen in all the pressure variables are again very large, making a detailed analysis of them statistically meaningless. The negative values seen in the atomic and molecular pressure tensor components in the X axis indicate that the total area of the head group is too large and should be reduced.

There appears to be no direct correlation between any of the parameters obtain from the analysis of the trajectory data. There does however appear to be a general correlation between the potential energy and the Lennard-Jones energy, with the Lennard-Jones energy following the general form of the potential, fig 6.1.5.

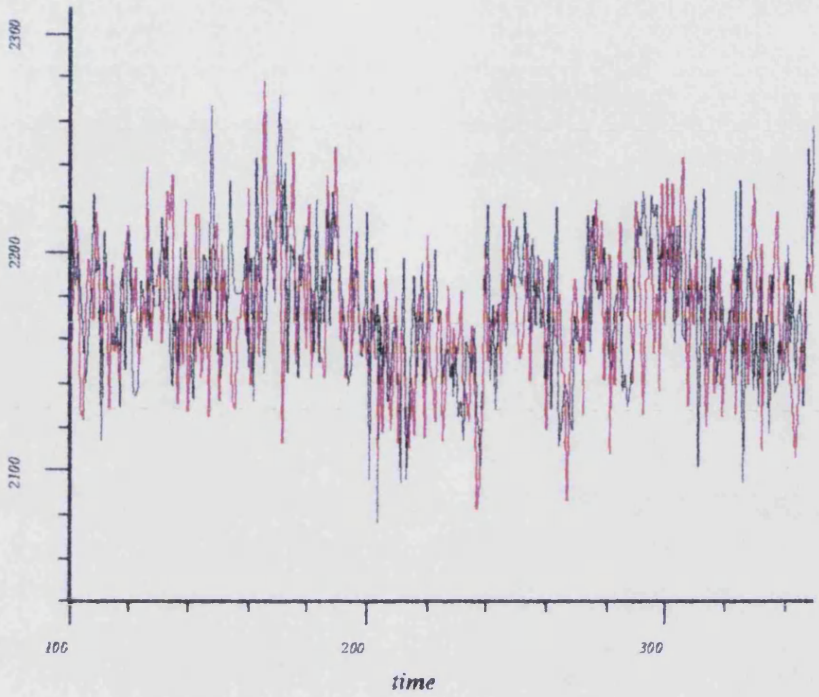


**Fig 6.1.5** Potential ( black ) and Lennard-Jones ( red ) energies for time period 100-350 ps

As in the previous chapter, it is presumably intermolecular interactions that form this correlation as there appear to be no correlations between the potential and internal energies. There does appear to be a degree of correlation between the Lennard-Jones energy and the pressure tensor along unit cell vector B, i.e. the bilayer normal, further indicating that any correlation between the Lennard-Jones and potential energies is due to intermolecular interactions.

### 6.1.4 Fourier Transformation of Trajectory Data

The thermodynamic data for this section of the simulation, 100-350 ps, has been fourier transformed to reveal any correlations within the data. The data is transformed from the time domain into the frequency domain. Any events that occur over a regular time span will appear at the frequency of that time period.

Digital signal processing techniques can be applied to the fourier transformed data to remove frequencies that are not of interest, usually high frequency modes such as bond stretches and angles bends. This results in the removal of 'noise' from the property, this resultant property can then be back transformed into the time domain to give the low frequency 'noiseless' property. This enables the investigation of these low frequency motions, which are often conformational changes[2].

As expected there is no peak at 160 $cm^{-1}$ seen in any of the transformed spectra, due to there being no pressure bath scaling applied to the system. There are no other obvious peaks that occur in the majority of spectra.

The fourier transformed spectra for the potential, kinetic and total energies are shown in fig 6.1.6.

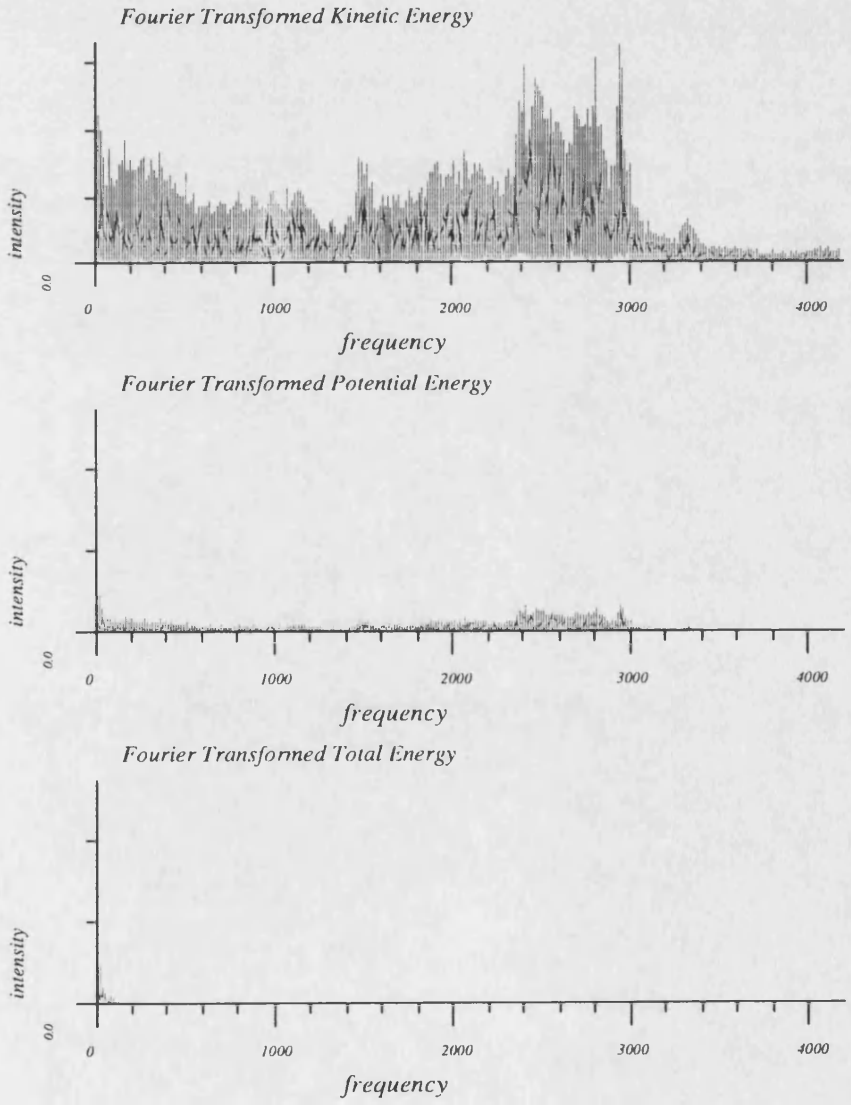


**Fig 6.1.6** Fourier transformed Potential, Kinetic and Total Energies

The peaks seen in the kinetic energy between 2500 and 3500 $cm^{-1}$ are presumably due to the affect the temperature bath scaling has upon the bond stretching. The velocity of the atoms being scaled thus effecting the speed of the oscillation. Presumably these affects would also be found in the kinetic energy spectra from the C5 simulations except that their intensity is very small compared to that of the peak at 160 $cm^{-1}$.

### 6.1.5 Filtering of Trajectory Data

The relationship between the potential energy and the Lennard-Jones energy has been investigated using fourier transform techniques.

The thermodynamic data has been filtered to remove any frequencies above 20 $cm^{-1}$. A degree of correlation is observed between the Lennard-Jones energy and potential energy with the Lennard-Jones energy following the form of the potential energy, fig 6.1.7, this is not as directly correlated as in the Ceramide 5 simulations, see chapter 5.

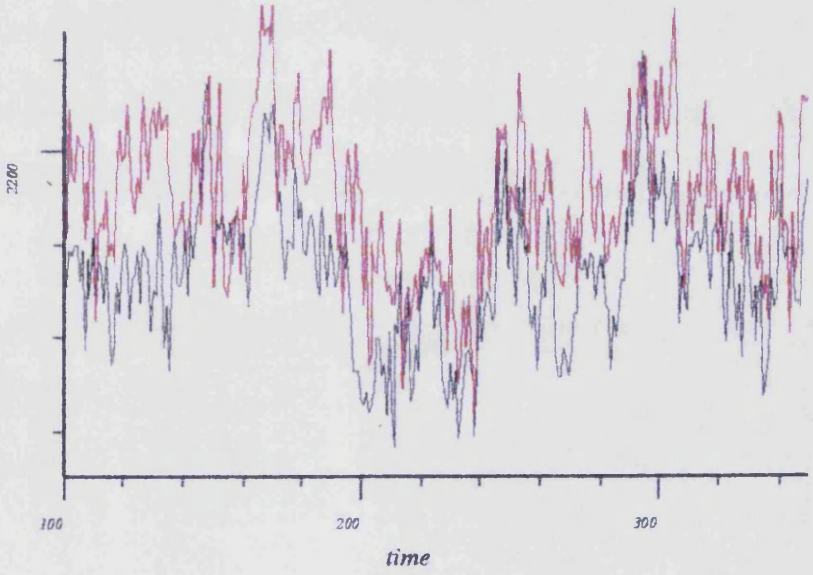


**Fig 6.1.7** Filtered Potential ( black ) and Lennard-Jones ( red ) Energies

There is a degree of correlation between the Lennard-Jones energy and the component of the molecular pressure tensor along the bilayer normal, unit cell vector B, fig 6.1.8. These properties appear to be better correlated in the later half of the simulation, 200-350 ps, rather than in the initial 100 ps this is also seen in a slight correlation between the Lennard-Jones energy and the molecular pressure which is better expressed in the later half of the simulation rather than the first 100-200 ps stage.

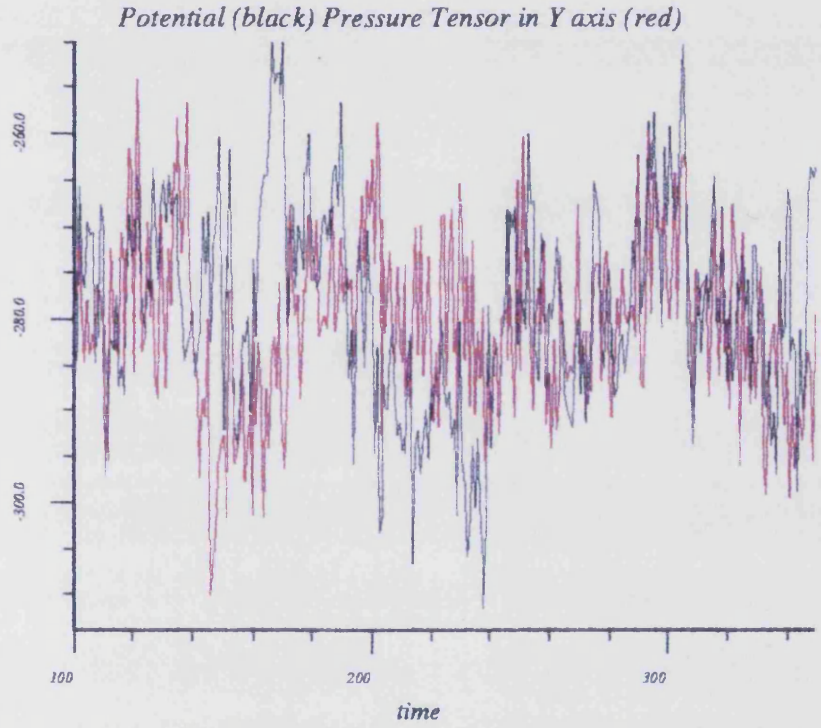


**Fig 6.1.8** Filtered Lennard-Jones Energy and Component of the Molecular Pressure Tensor along the Y axis

The correlation between the Lennard-Jones energy and the pressure tensor along the bilayer normal is explained in terms of the breathing motion of the bilayer seen in the examination of the co-ordinate trajectories. Where the two monolayers of the bilayer move apart from each other slightly and then move back together.

## 6.1.6 Analysis of Structural Data

### Chain Torsion Angles

The torsion angles, as described in chapter 3, for the two acyl chains are shown in table 6.1.6, below.

**Table 6.1.6** Acyl chain torsion angles for C4_1 simulation

| | Average 100-350 ps | Standard Deviation | | Average 100-350 ps | Standard Deviation |
|---|---|---|---|---|---|
| $\phi_1$ | 180.3 | 10.6 | $\phi_{17}$ | 179.8 | 9.4 |
| $\phi_2$ | 179.7 | 9.7 | $\phi_{18}$ | 178.8 | 9.5 |
| $\phi_3$ | 177.7 | 13.2 | $\phi_{19}$ | 179.4 | 10.9 |
| $\phi_4$ | 180.0 | 9.6 | $\phi_{20}$ | 178.8 | 9.6 |
| $\phi_5$ | 181.1 | 11.3 | $\phi_{21}$ | 180.4 | 10.8 |
| $\phi_6$ | 180.0 | 9.7 | $\phi_{22}$ | 178.5 | 10.4 |
| $\phi_6$ | 181.0 | 11.2 | $\phi_{23}$ | 179.9 | 9.9 |
| $\phi_8$ | 179.3 | 11.1 | $\phi_{24}$ | 177.2 | 12.1 |
| $\phi_9$ | 180.9 | 13.3 | $\phi_{25}$ | 179.9 | 10.4 |
| $\phi_{10}$ | 180.9 | 15.4 | $\phi_{26}$ | 179.9 | 11.9 |
| $\phi_{11}$ | 176.8 | 11.5 | $\phi_{27}$ | 179.8 | 11.7 |
| $\phi_{12}$ | 179.1 | 11.6 | $\phi_{28}$ | 179.9 | 11.4 |
| $\phi_{13}$ | 181.1 | 10.1 | $\phi_{29}$ | 182.3 | 13.7 |
| $\phi_{14}$ | 179.5 | 10.4 | $\phi_{30}$ | 181.9 | 19.6 |
| $\phi_{15}$ | 180.0 | 9.5 | $\phi_{31}$ | 180.1 | 19.9 |
| $\phi_{16}$ | 178.6 | 10.1 | | | |

The fluidity of the acyl chains is shown by their average torsion angles and standard deviations. As can be seen from the table above there is very little rotational

motion seen in any of the acyl chains, they all oscillate with very small standard deviations around the initial starting conformation of 180°.

This is a very curious result, as it would be expected that having a considerably longer chain 2 would allow for a much greater torsional freedom, especially in that second chain, due to the increased volume. The initial co-ordinates of the system may have prevented early torsional motion, due to the slight interdigitation. However, after the initial few picoseconds the monolayers had moved apart from each other eliminating the interdigitation. The longer chain would be expected to reduce the freedom of the early torsion angles, seen in experimental order parameters, but the torsions towards the end of the chain would then be expected to have more rotational freedom. Obviously the system conditions have prevented this from occurring, resulting in a very inflexible and static system.

### Segmental Order Parameters

The segmental order parameters for the two acyl chains have been calculated, these are displayed below in fig 6.1.9.

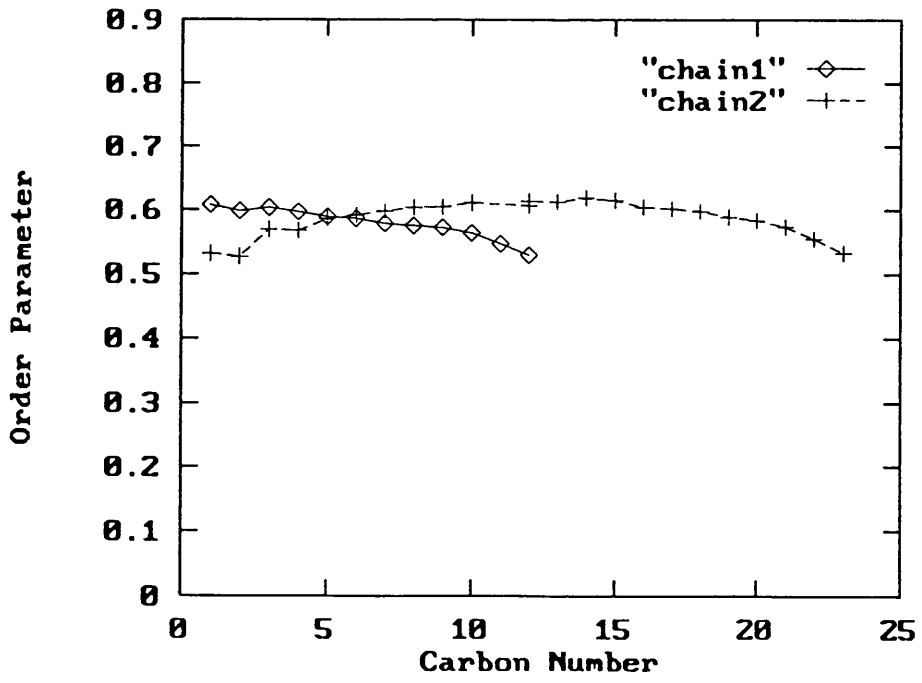


**Fig 6.1.9** Segmental Order Parameters for C4_1

The segmental order parameters further confirm the lack of rotational freedom observed from the torsion data. The order parameters are essentially flat for the majority of the acyl chains only decreasing as the end of the chain is approached. This in agreement with the slight increase in standard deviation seen in torsion angles lower down the acyl chain. The high values for the order parameters also indicates the lack of freedom in these chains, with a lack of fluidity in the centre of the bilayer, although these values are larger than the experimental values.

The shorter chain, chain 1, has a characteristic fall off in the order parameter values from carbon number 8 downwards. Also in the longer chain, chain 2, there is a falling off in the parameter values from carbon number 15 downwards. However as already stated, there is so little spread in these values that all the carbons in both chains lack rotational freedom. The actual values of these order parameters agree with those obtained experimentally[3,4].

## 6.2.0 Ceramide 4 Bilayer with a Central Cholesterol Substituted

The bilayer model C4_2, consisting of 17 Ceramide 4 lipids and a single cholesterol molecule was constructed using the starting conformation for bilayer model C4_1 as a template. The central lipid in the top monolayer was replaced by a cholesterol molecule using the *Insight*[5] molecular modelling suite. The y axis was still the bilayer normal, with the x and z axes describing the head group.

The resulting co-ordinates were then minimised, under periodic boundary conditions, until the total maximum derivative was less than 0.5 kcal $mol^{-1}$ $Å^{-1}$. These minimised co-ordinates were used as the starting conformation for the molecular dynamics simulation.

The initial unit cell dimensions were identical to those of the C4_1 model as seen in table 6.2.1.

**Table** 6.2.1 Unit cell Dimensions

| Unit cell vector A | Unit cell vector B | Unit cell vector C | Unit cell angles $\alpha = \beta = \gamma$ | Unit cell Volume |
|---|---|---|---|---|
| Å | Å | Å | ° | $Å^3$ |
| 24.5 | 59.0 | 25.0 | 90 | 36138 |

### 6.2.1 Simulation Conditions

The bilayer model was initially sampled with a constant temperature bath applied, a target temperature of 300 K to stabilise the system, after 15 ps the target temperature was altered to 310 K for 30 ps and finally at 45 ps the target temperature was raised again to 320 K with a temperature bath time constant of 150 fs. The model was sampled for a further 170 ps under these conditions, i.e. a constant temperature simulation. After 228 ps of the simulation a bond catastrophe occurred

and the simulation was stopped, for these purposes the simulation will only be analysed from 100-220 ps. The factors causing the bond catastrophe will be discussed further.

## 6.2.2 Analysis of Thermodynamic Data

The extracted thermodynamic data is shown in fig 6.2.1.

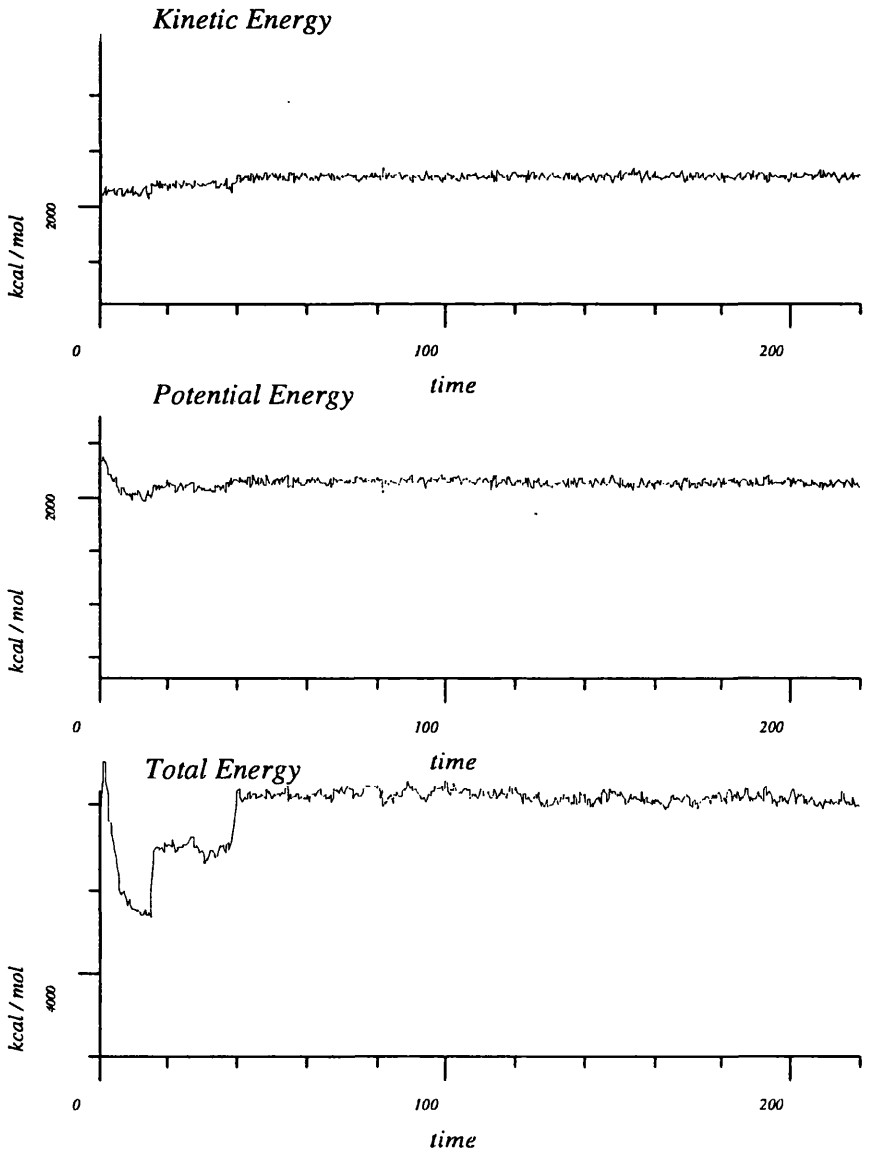


**Fig 6.2.1a** Potential, Kinetic and Total Energies for C4_2

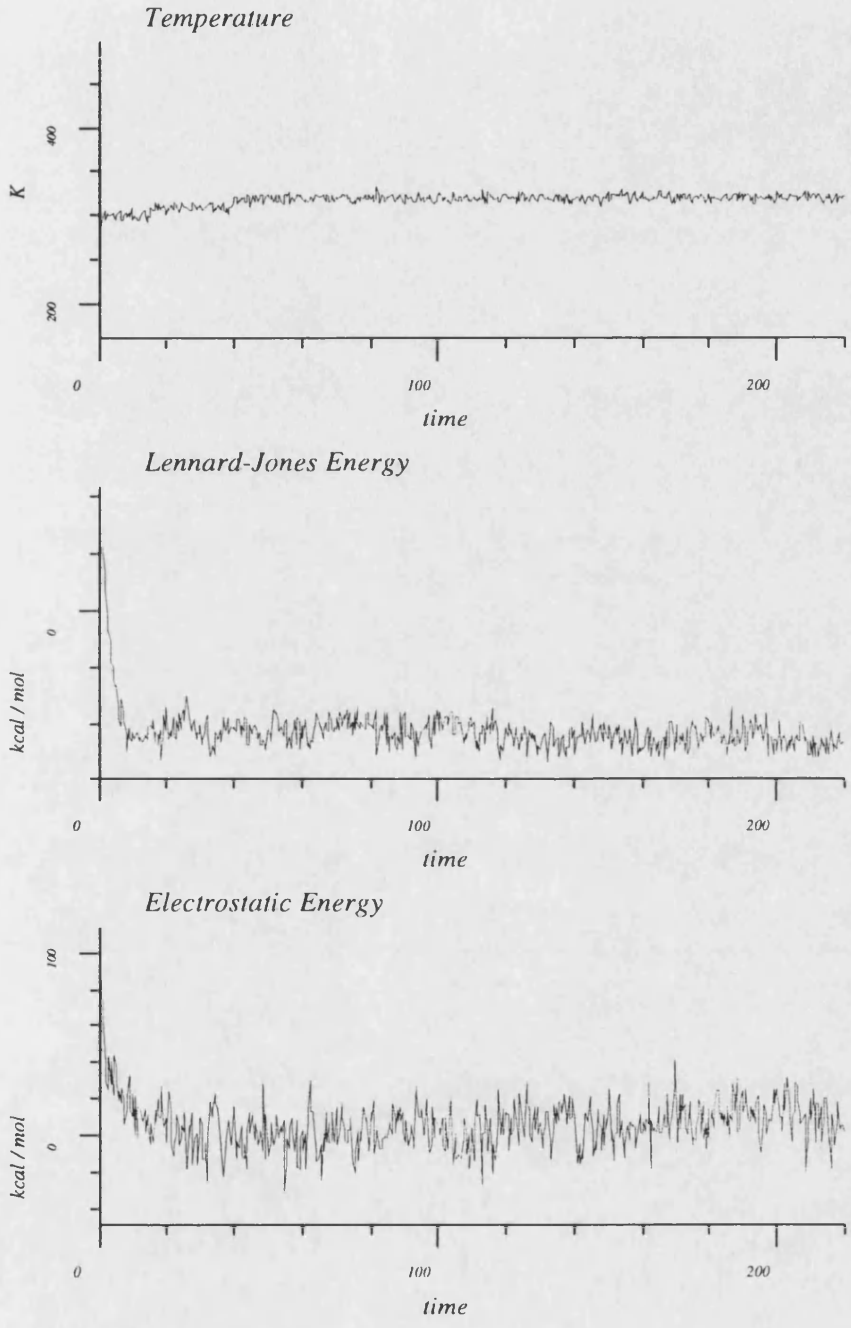


**Fig 6.2.1b** Electrostatic and Lennard-Jones Energies and Temperature Profiles for C4_2

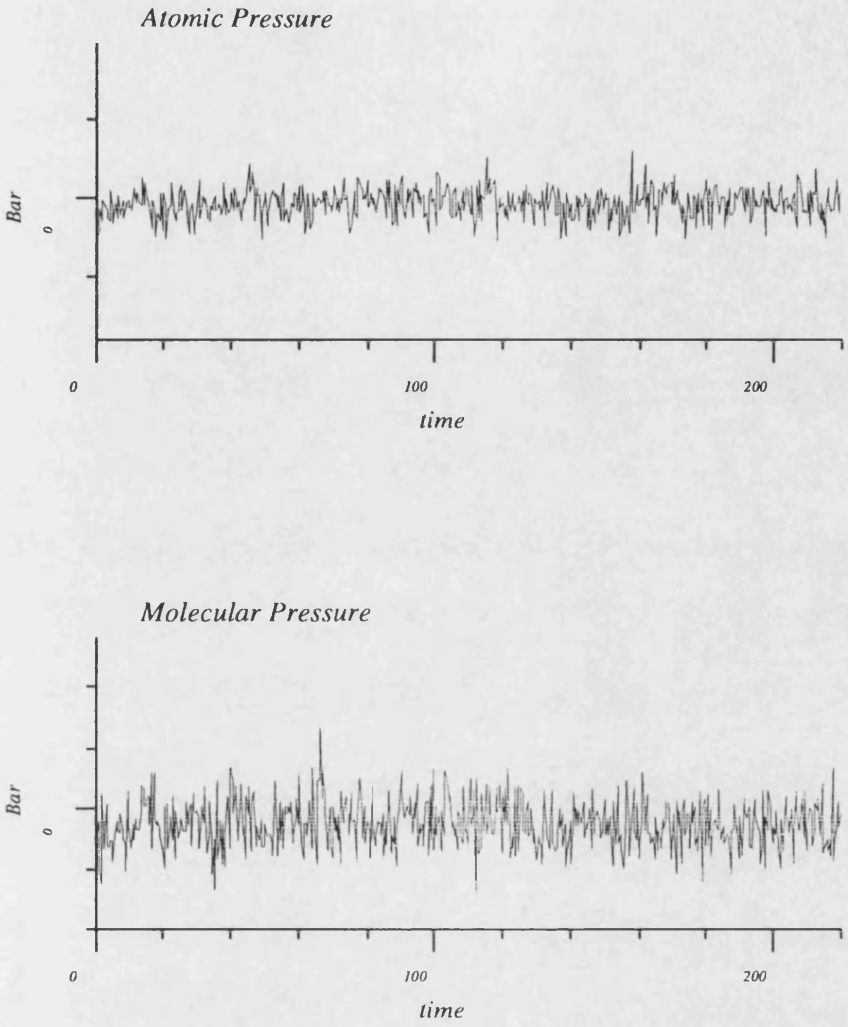


**Fig 6.2.1c** Atomic and Molecular Pressures for C4_2

The effect of the temperature bath and the initial changes can clearly be seen on the potential, kinetic and total energy plots. The Lennard-Jones and electrostatic energies appear to be relatively stable over the simulation as do the molecular and atomic pressures. As expected all the internal energies are stable over the simulation.

### 6.2.3 Analysis of 100 - 220 ps

The plots of the kinetic, potential and total energies are shown in fig 6.2.2, the average values and their standard deviations are shown in table 6.2.2, from these it can be seen that the simulation is relatively stable up until 220 ps, with only very small standard deviations.

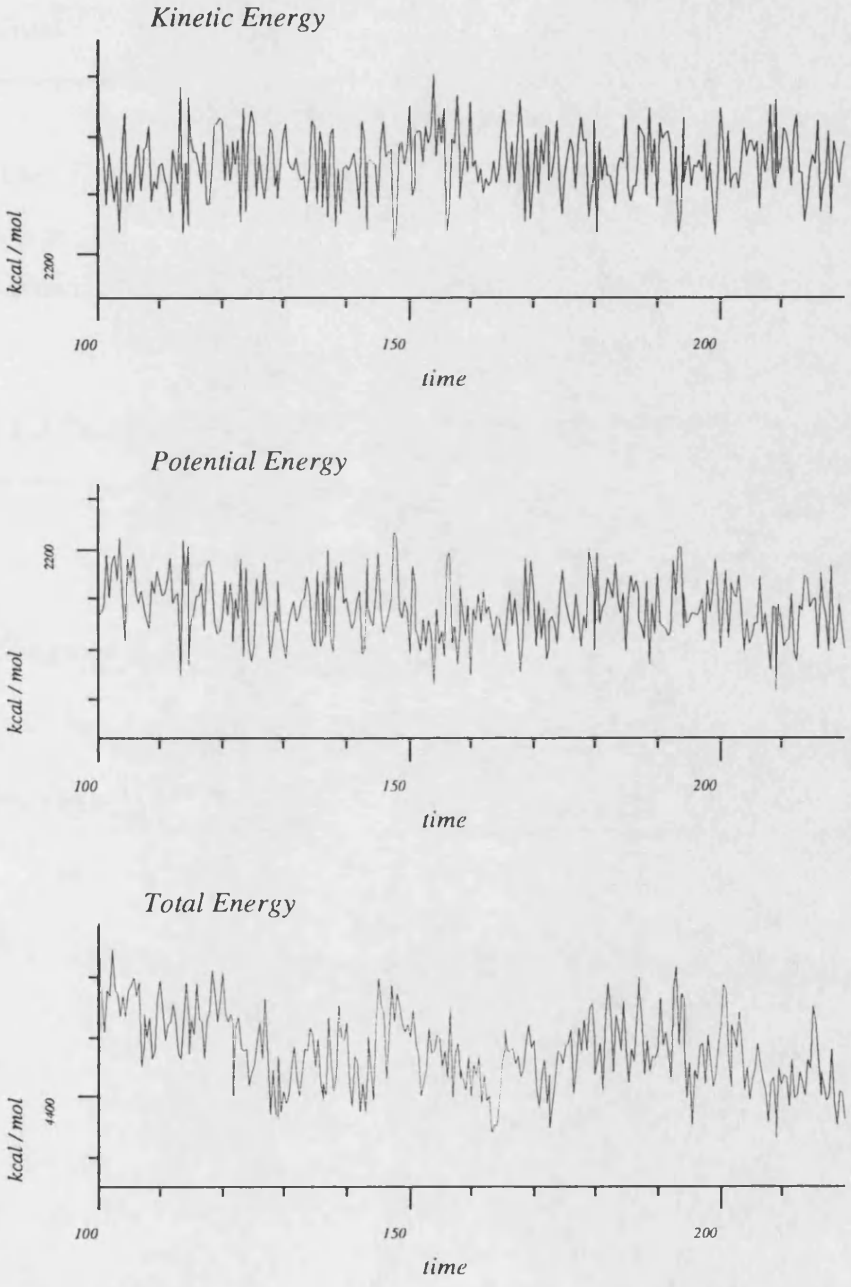


**Fig 6.2.2** Potential, Kinetic and Total Energies for Time Period 100-220 ps

**Table 6.2.2** Average Energies

| Energy<br>kcal $mol^{-1}$ | Average<br>100-220 ps | Standard<br>Deviation | % |
|---|---|---|---|
| Potential | 2142.2 | 30.6 | 1.4 |
| Kinetic | 2276.1 | 26.8 | 1.2 |
| Total | 4418.2 | 20.8 | 0.5 |

The temperature is very stable around the target temperature, whilst the pressure is negative for both the atomic and molecular calculations, indicating that the unit cell dimensions are too large, table 6.2.3

**Table 6.2.3** Temperature and Pressure Averages.

| | Average<br>100-220 ps | Standard<br>Deviation |
|---|---|---|
| Temperature<br>K | 320.1 | 3.8 |
| Molecular pressure<br>bar | – 242.0 | 389.7 |
| Atomic pressure<br>bar | – 315.1 | 865.0 |

Analysis of the components of atomic and molecular pressure tensors in the unit cell axes indicates that it is the pressure along the bilayer normal that has the largest negative value, table 6.2.4. This shows that this vector is too large and should be reduced. However the standard deviations for all of these values are so large as to make a detailed an analysis of this data statistically meaningless.

**Table 6.2.4** Atomic and Molecular Pressure Tensors

| Component of Atomic pressure tensor along ( bar ) | Average 100-220 ps | Standard Deviation |
|---|---|---|
| X axis | – 103.3 | 1255.6 |
| Y axis | – 770.3 | 1475.3 |
| Z axis | – 71.7 | 1254.4 |
| Component of Molecular pressure tensor along ( bar ) | | |
| X axis | – 22.1 | 321.4 |
| Y-axis | – 702.3 | 957.9 |
| Z-axis | 16.5 | 467.1 |

There appears to be a degree of correlation between the potential energy and the Lennard-Jones energy, fig 6.2.3.

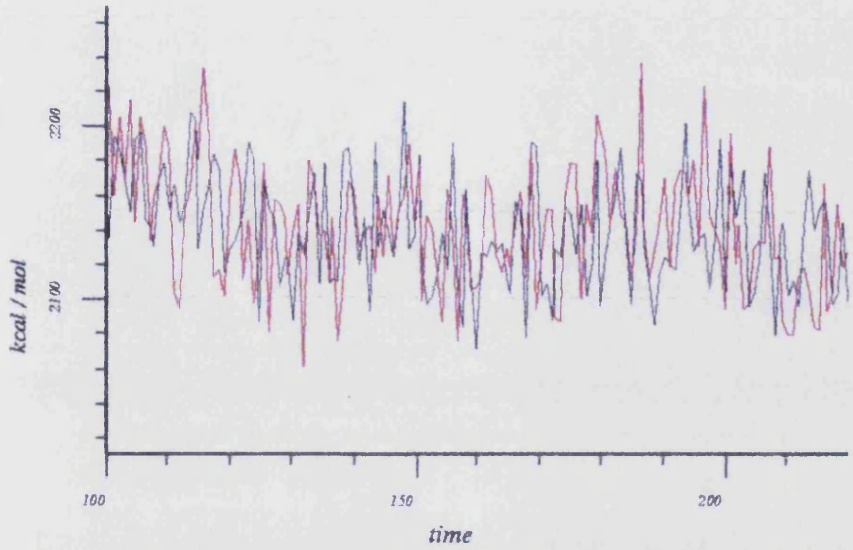


**Fig 6.2.3** Potential ( black ) and Lennard-Jones (red ) Energies for 100-220 ps

This may be a consequence of the pressure being dominated by one axis. This correlation and any others has been investigated by using digital signal processing techniques.

## 6.2.4 Fourier Transformation of Thermodynamic Data

The thermodynamic data has been fourier transformed, from the time domain into the frequency domain, in order to investigate any correlations within the data.

As in the previous simulation there are no dominant peaks around 160 $cm^{-1}$ seen in any of the spectra. There are no high intensity peaks which are common to the majority of the spectra.

The fourier transformed spectra of the potential, kinetic and total energies are shown in fig 6.2.4. Again the kinetic energy spectra shows significant peaks in the range from 2500-3000 $cm^{-1}$. This is presumably due to the altering of atomic velocities, due to temperature scaling, effecting the bond vibrations.

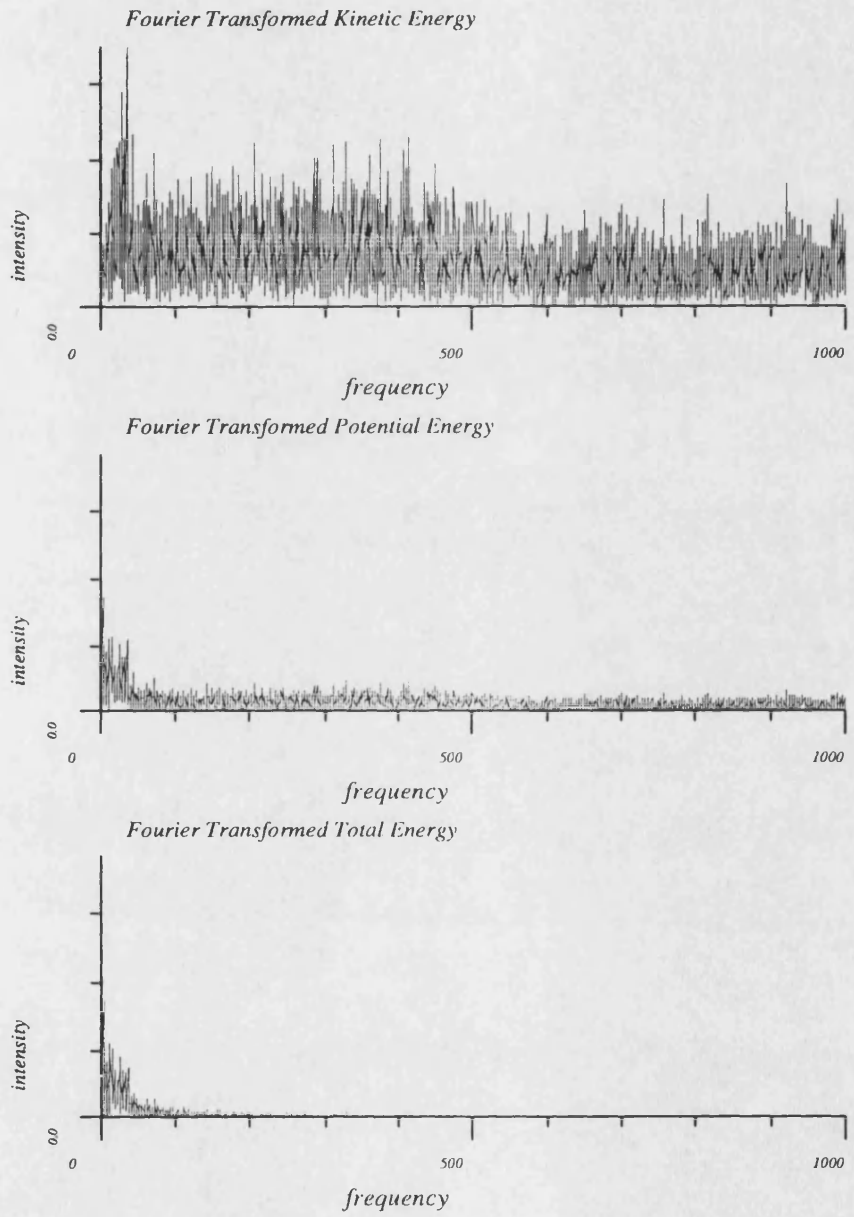


**Fig 6.2.4** Fourier transformed Potential, Kinetic and Total Energies.

## 6.2.5 Filtering of Trajectory Data

The thermodynamic data has been filtered to remove any frequencies above 20 $cm^{-1}$. This filtering has been used to investigated the degree of correlation between the potential energy and the Lennard-Jones energy. There is a degree of correlation between these two, with the form of the Lennard-Jones energy following the general form of the potential energy, fig 6.2.5, but this is not a direct correlation.

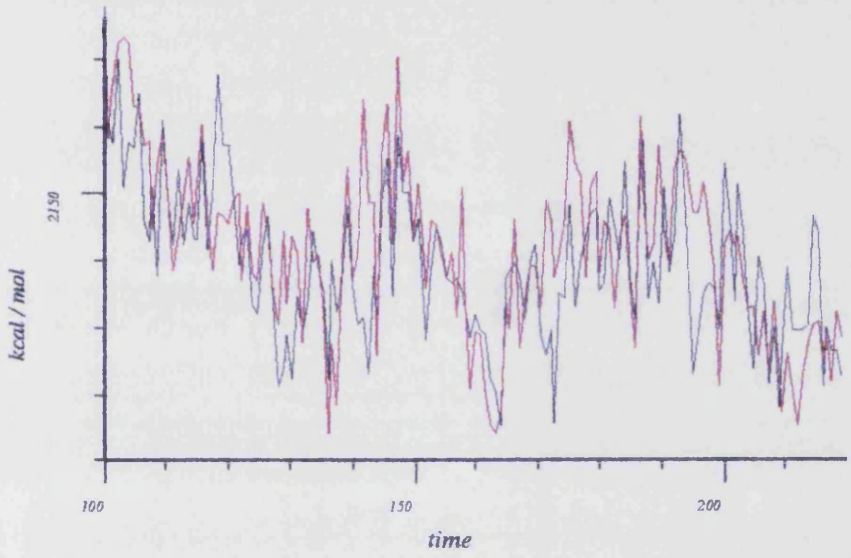


**Fig 6.2.5** Filtered Potential ( black ) and Lennard-Jones ( red ) Energies.

This correlation is closer during the initial period under investigation, as the time approaches the end of the simulation the correlation lessens. There is also some correlation between the Lennard-Jones energy and the component of the molecular pressure tensor in the Y axis, the bilayer normal, fig 6.2.6. This indicates that the pressure component in the bilayer normal direction is significantly affecting the Lennard-Jones energy. It is this pressure component that has the largest negative value, table 6.2.4, indicating that this axis and hence unit cell vector is too large. There are no other correlated variables seen from this filtering.

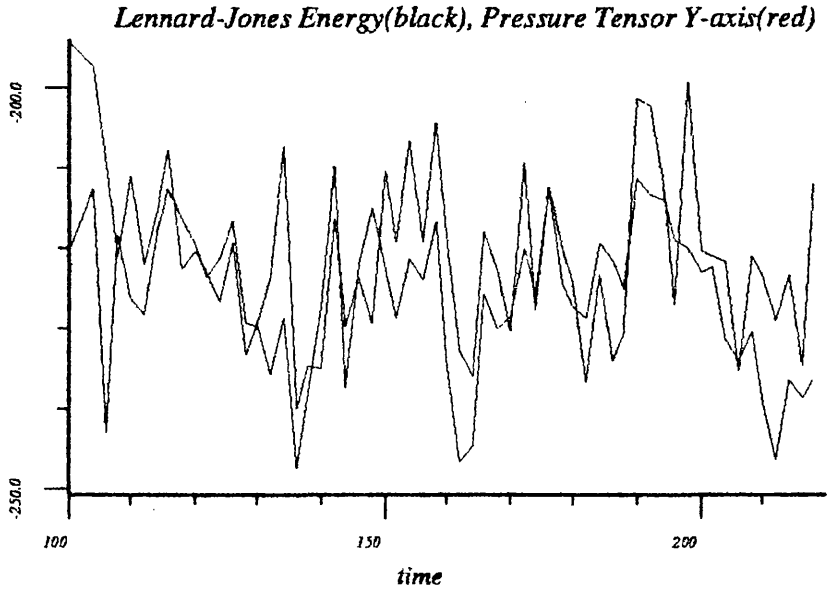


**Fig 6.2.6** Filtered Lennard-Jones Energy and Component of Molecular Pressure in the Y axis

## 6.2.6 Analysis of Structural Data

### Chain Torsion Angles

The torsion angles, as described in chapter 3, for the two acyl chains are shown in table 6.2.5, below.

**Table 6.2.5** Acyl chain torsion angles

| | Average 100-220 ps | Standard Deviation | | Average 100-220 ps | Standard Deviation |
|---|---|---|---|---|---|
| $\phi_1$ | 180.6 | 12.6 | $\phi_{17}$ | 180.1 | 9.4 |
| $\phi_2$ | 179.6 | 10.8 | $\phi_{18}$ | 178.6 | 11.2 |
| $\phi_3$ | 179.9 | 9.9 | $\phi_{19}$ | 179.8 | 9.5 |
| $\phi_4$ | 179.9 | 9.6 | $\phi_{20}$ | 180.3 | 11.0 |
| $\phi_5$ | 179.9 | 9.7 | $\phi_{21}$ | 179.5 | 10.5 |
| $\phi_6$ | 179.9 | 9.9 | $\phi_{22}$ | 179.7 | 10.6 |
| $\phi_7$ | 179.2 | 11.9 | $\phi_{23}$ | 180.1 | 10.2 |
| $\phi_8$ | 179.4 | 11.1 | $\phi_{24}$ | 180.1 | 11.7 |
| $\phi_9$ | 179.4 | 15.0 | $\phi_{25}$ | 180.2 | 10.8 |
| $\phi_{10}$ | 180.6 | 12.5 | $\phi_{26}$ | 180.6 | 11.9 |
| $\phi_{11}$ | 176.4 | 11.9 | $\phi_{27}$ | 180.7 | 12.1 |
| $\phi_{12}$ | 176.2 | 12.7 | $\phi_{28}$ | 177.1 | 14.1 |
| $\phi_{13}$ | 180.4 | 11.0 | $\phi_{29}$ | 178.8 | 14.8 |
| $\phi_{14}$ | 177.0 | 12.8 | $\phi_{30}$ | 179.9 | 19.9 |
| $\phi_{15}$ | 180.1 | 9.5 | $\phi_{31}$ | 178.3 | 20.9 |
| $\phi_{16}$ | 178.7 | 10.5 | | | |

The average torsion angles and their standard deviations give an indication of the fluidity of the system and its flexibility. The data in table 6.2.5 shows that this

bilayer system is very static and inflexible, with all the torsion angles oscillating around their initial starting values, 180°, with very small standard deviations, < 20°.

This is a surprising result as there is a considerable difference in length between the two acyl chains, chain 2 is 10 carbons longer, and thus it would be expected for there to be a higher degree of flexibility in this chain, as there is more volume available for it to rotate in, unless the terminal carbons have become 'anchored' in the opposite bilayer and are thus prevented from rotating. However this is not indicated by either any noticeably large values in the Lennard-Jones energy, nor by any significant decrease in the standard deviations for those torsions, indeed the terminal torsions for chain 2 are the only ones in which there is any significant standard deviation, >15°. Thus indicating that the system conditions are causing this lack of rotational freedom. There is more rotational freedom in the initial torsions of each chain, $\phi_{1,2}$ and $\phi$ but this is soon reduced as the middle of each chain is approached, the chains becoming more rotationally restricted until the last torsions of each chain..

**Segmental Order Parameters**

The segmental order parameters for the two acyl chains have been calculated, these are displayed below in fig 6.2.7.

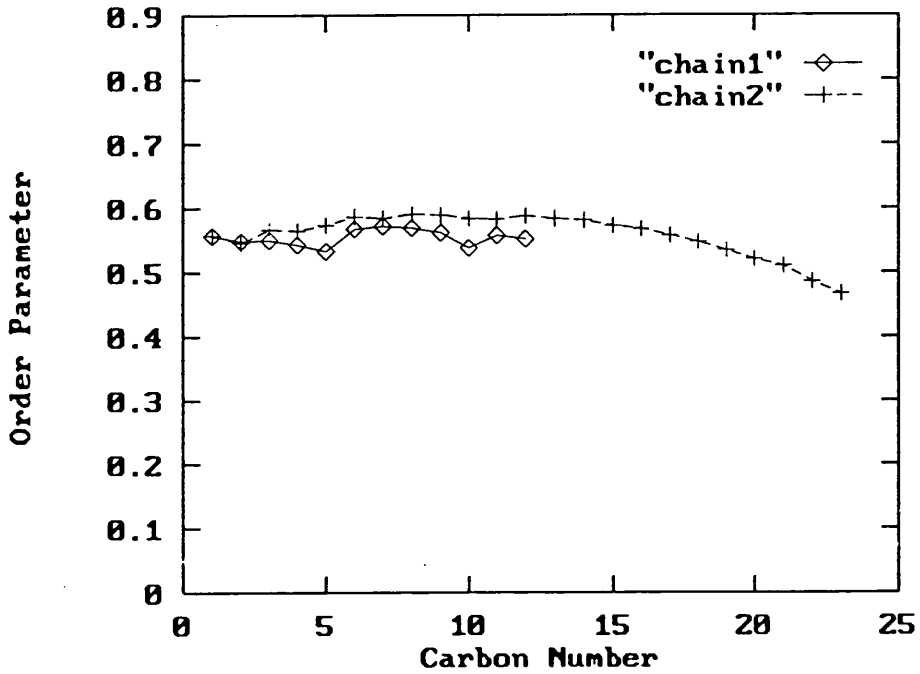


**Fig 6.2.7** Segmental Order Parameters for chains 1 and 2 of C4_2

The torsion data for this simulation indicated that the torsions have very little rotational freedom, all being essentially fixed around their initial 180° starting conformation. This is further seen in the analysis of the segmental order parameters. These all have very high values indicating a lack of freedom. The characteristic plateau of values up to carbon number 8 is observed in the shorter chain and up to carbon 15 in the longer chain, but these 'plateaux' are continued much further down both chains, only at the very ends of the acyl chains is any decrease in the order parameters observed. Again this mirrors the torsion data, where only the final few torsions in the acyl chains had standard deviations > 15°. Both the torsion data and the order parameters indicate that the system lacks fluidity, being quite rigid in the hydrophobic centre of the bilayer.

## 6.3.0 Investigation of Bond Catastrophe

As stated previously the C4_2 model underwent a bond catastrophe 228 ps into the simulation. The reasons for this have been investigated by analysing the thermodynamic and structural data for the preceding few picoseconds.

There was a build up in the bond energy around the fused atoms of the A and B rings of the cholesterol, see fig 6.3.1.

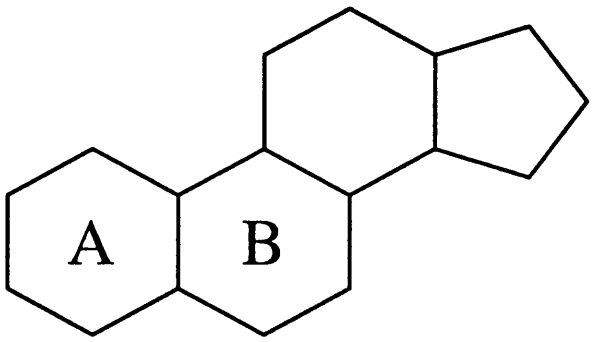


**Fig 6.3.1** A and B rings of steroids

The bond energy built up from non-bonded interactions between the cholesterol and its surrounding lipids. Between 228 and 229 ps this build up reached a maximum and it had sufficient energy to force the bond between atoms 9 and 10, see fig 6.3.2 to blow apart.

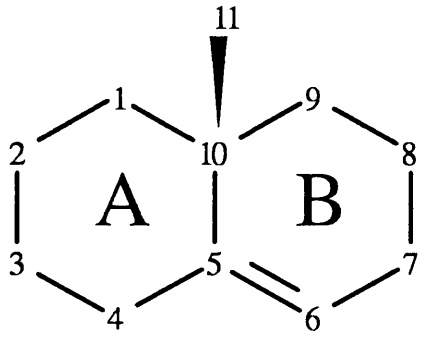


**Fig 6.3.2** Atoms numbers for bond catastrophe

The build up in energy in the bonds of the ring is due to the strained ring system. Non-bonded interactions are calculated for all pairs of atoms separated by 2 or more bonds, the first non-bonded interactions to be taken into account are those between atoms separated by two atoms, fig 6.3.3, these are known as 1,4 interactions.

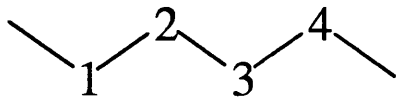


**Fig 6.3.3** 1-4 Non-bonded interactions

This interaction is also described by the torsion parameter for those 4 atoms. The VFF[6] potential is parameterised to take this into account, i.e. the experimental torsion barrier is given by the sum of the 1,4 non-bond interaction and the torsion potential. For $sp^2$ systems in aromatic ring systems the favoured torsion angles can be 0°. At this angle the 1,4 atoms are spatially close to each other so the non-bond interaction will attempt to force them to move further away, in competition with the torsion potential. Particular problems occur with six membered rings, where 1,4 interactions at low torsion angles occur across the ring between every set of atoms opposite each other, fig 6.3.4.

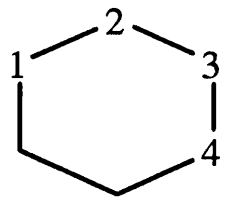


**Fig 6.3.4** 1,4 Interactions in 6 Membered Rings

In steroid ring systems the problem is further increased by the presence of fused six membered rings. This results in those atoms of the fused system being involved in 1,4 interactions in both ring systems. In the specific case of cholesterol the situation is further exacerbated by the two atoms fusing rings A and B, being

strained quaternary carbons, fig 6.3.2. Carbon 5 is part of the double bond system causing strain to both ring A and B.

In the present simulation intra and intermolecular clashes have resulted in a build up of energy around the ring fusion atoms. This results in a build up of energy in the bond between atoms 9 and 10 and eventually this energy reaches such a level that it is sufficient to cause the bond to blow apart. This bond breakage alleviates the 1,4 interactions by reducing the strain in the ring system. Other potentials also have problems with these interactions and have suggested scaling to reduce them[7].

## 6.4.0 Conclusions

These simulations were conducted using the constant temperature bath methodology. Both the simulations have very stable energetic profiles for the duration of the sampling period, with no standard deviation being greater than 1.5 % in any of the kinetic, potential or total energies. The data sampled for the C4_2 simulation does not include the few picoseconds before the bond catastrophe.

### 6.4.1 Constant Temperature Bath

The constant temperature bath conditions have resulted in the two average temperatures for the simulations being virtually identical to each and to the target temperature of 320 K, see table 6.4.1

**Table 6.4.1** Average temperatures for the C4 simulations

| Temperature for simulation K | Average over sampled period | Standard Deviation |
|---|---|---|
| C4_1 | 320.1 | 3.7 |
| C4_2 | 320.1 | 3.8 |

The similarities in the average temperatures and their standard deviations shows the short time correlation between this variable and the system, considering the differences in the time periods considered in each.

### 6.4.2 Effect of Molecular Substitution

The effect of the cholesterol molecule in this simulation appears to have been to reduce both the molecular and atomic pressures. These simulations have been performed under constant volume conditions and so obviously the unit cell can not change its volume. However the C4_2 simulation results in both a negative molecular and atomic pressure. This indicates that the unit cell for this simulation is too large and that if the volume were allowed to fluctuate then the volume would reduce to account for this anomalous condition. Thus the substitution of a ceramide for

cholesterol appears to have caused this change. There are several plausible reason for this,

- Cholesterol has a lower overall volume than a Ceramide 4.
- Cholesterol is thinner than the ceramide it is replacing.
- Cholesterol interacts more favourably because the repulsive interactions between ceramide-ceramide and ceramide-cholesterol are lowered.

### 6.4.3 Thermodynamic Results

The fourier transform results show that there is no coupling between the pressure and the kinetic energy in either of the simulations. The peaks seen at 160 $cm^{-1}$ in the C5 simulations are not present as direct consequence of not performing any pressure scaling.

The filtered trajectories show relationships between the potential energy and the Lennard-Jones energy in both simulations. There are no relationships seen between the potential energy and any of the internal energies indicating that these relationships are due to intermolecular changes in the system.

This is further confirmed, in both simulations, by the relationship seen between the Lennard-Jones energy and the component of the molecular pressure tensor in the Y axis, the bilayer normal. The filtered trajectory of this component is also seen to follow the molecular pressure, indicating that it is the most dominant component in the pressure. This is explained in terms of the breathing motion of the bilayer. The two monolayers of the bilayer are seen to move away from and toward each other during the course of the simulation. Thus there will be accompanying changes in the Lennard-Jones energy as the monolayers come closer together and move further apart, thus causing changes in the potential energy. This breathing motion occurs within a unit cell that is not allowed to change its volume, no pressure. This motion may be a direct consequence of the lack of pressure scaling and thus the enforced inability of the system to adjust to the pressures fluctuations.

## 6.5.0 References

1 D.J. Osguthorpe and P. Dauber-Osguthorpe, Journal Of Molecular Graphics 10 (1992) 178.

2 R.B. Sessions, D.J. Osguthorpe and P. Dauber-Osguthorpe, J. Phys. Chem. 99 (1995) 9034.

3 P. Ewald, Ann. Phys. 64 (1921) 253.

4 K.F. Lau, H.E. Alper, T.S. Thatcher and T.R. Stouch, J. Phys. Chem. 98 (1994) 8785.

5 INSIGHT, BIOSYM technologies, San Diego, USA, (1989).

6 P. Dauber-Osguthorpe, V.A. Roberts, D.J. Osguthorpe, J. Wolff, M. Genest and A.T. Hagler, Proteins-Structure Function And Genetics 4 (1988) 31.

7 S.J. Weiner, P.A. Kollman, D.A. Case, U.C. Singh, C. C.Ghio, S. Alagona, S.J. Profeta and P. Weiner, J. Am. Chem. Soc. 106 (1984) 765.

# Chapter 7

*CONCLUSION*

## 7.0 Conclusion

The first simulations of skin lipid bilayer systems have been performed. These systems have been analysed in order to examine their thermodynamic and structural behaviour. The bilayer systems included lipids with symmetric and asymmetric acyl chain lengths and the inclusion of dopant molecules, cholesterol. In order to investigate the dynamic behaviour of the bilayers new methodology has been developed and tested.

## 7.1 Development of Methodology

The Velocity Verlet[1] integration algorithm has been incorporated into the VFF[2] in order to facilitate the use of some new constant temperature bath routines. There is an error associated with the use of a truncated cutoff applied to the non-bonded potential interactions when investigating heterogeneous systems with partial charges. This results in a difference in the average velocities of sub-components of the system, thus the average temperatures of these sub-components is also very different. To investigate this problem simulations of a protein in water have been performed at constant temperature. A 40 K difference in the average temperature between the protein and the water resulted, whilst the average temperature of the whole system was at the target temperature.

Two methodologies, based upon the use of temperature baths, have been implemented in this study in order to circumvent this problem.

- The first of these samples a new set of velocities from a Maxwell-Boltzmann distribution about the temperature of the last step. This methodology has been applied to the trial protein and water system and resulted in the protein being

simulated at the target temperature. Thus this method provides a solution to the cutoff problem. However due to the reassignment of velocities from a random distribution the time dependency of the simulation is lost across these reassignments as it impossible to back integrate. Essentially this is a Monte-Carlo step taken during a dynamics simulation. Thus time dependent properties should not be calculated over these. If the velocity reassignment is removed from the simulation then eventually the velocity disparity will re-establish itself.

- The second solution involves the use of multiple temperature baths rather than a single one. In an analogous fashion this methodology has been applied to the protein and water system, this again resulted in the protein being simulated at the target temperature. A consequence of scaling two or more bodies in a system with different scaling factors is the inclusion of angular momentum artefacts into the simulation. To prevent this from happening the angular momentum before and after scaling is calculated for each sub-component and any difference is removed.

Both the methods proposed have resulted in simulations where the protein and the surrounding waters have been simulated at the target temperature. There are other methodologies that might be considered. The application of a switching function to the cutoff will remove the sudden discontinuity in energy and derivatives, seen with truncated cutoffs, that cause the temperature effects. However an investigation of a large protein, Streptomyces-Griseus Protease-A, by Kitson *et al*[3] has shown that the use of a truncated cutoff rather than one using switching functions results in a simulation in which the protein structure is closer to experiment. This is due to the nature of the derivatives of the function, while the function smoothly tapers off the potential to zero at cutoff, it introduces large forces in the switching region[4]. These forces retards the movement of molecules outward and inward from the cutoff creating structural artefacts.

Another method for calculating the long range forces is the Ewald sum[5]. This is a technique for efficiently summing the interaction between an ion an its periodic images. The function may be written as

$$V^{zz} = 1/2 \Sigma \{ \Sigma \Sigma z_i z_j | r_{ij} + n |^{-1} \} \qquad \text{( eqn 7.1 )}$$

where $z_i$, $z_j$ are the charges and the function is summed over n, the simple cubic lattice points.

This method would not have any of the problems associated with a truncated cutoff and hence there would not be inconsistencies with the derivatives. However, this potential implies that periodic images will be effected by each other, i.e. a crystallinity is being imparted to the system. This is not the case with biological systems. While plasma membranes do appear to have a degree of liquid crystal behaviour there is no evidence to suggest that there is any long range order in skin lipid bilayer systems. In simulations employing periodic boundary conditions, the crystallinity is an artefact used to reduce the edge effects. In these cases system sizes and cutoff distances are carefully chosen to exclude periodic interactions.

## 7.2 Simulations of Skin Lipid Bilayers

Two types of skin lipids have been studied, one with equal chain lengths, ceramide 5, and one with differing lengths, ceramide 4. Both of these lipid types are found to be constituents of skin bilayers. They have been modelled as pure bilayer systems and with a single dopant molecule cholesterol included.

The ceramide 5 simulations have shown that a stable bilayer can be produced and simulated. All three simulations were performed under similar conditions of constant temperature and pressure. The inclusion of dopant molecules, 5-cholesten-3β-ol and 5-cholesten-3α-ol, has not greatly effected the physical dimensions of the system, with all three showing similar average unit cell dimensions, see table 5.4.1. The dopants have altered the fluidity of the acyl chains in the bilayer core, this is observed in the segmental order parameter profiles. The bilayers have become more ordered as a consequence of the presence of cholesterol. The models fail to correctly

reproduce the form of the experimentally derived segmental order parameters however, the values for the order parameters are within the bounds of those derived from experiment.

The ceramide 4 simulations were performed under different conditions with only a temperature bath being applied. The simulation when cholesterol was included into the bilayer under went a bond catastrophe after 228 ps and could not be restarted, but before this occurred both simulations were stable. The build up of bond energy that resulted in the bond catastrophe began a few picoseconds before, due to intermolecular interactions between cholesterol and the surrounding lipids.

The torsion data and segmental order profiles obtained from these simulations show that the system has less freedom in the acyl chain region, i.e. higher order parameters. There is considerably less rotational freedom in the methylene units close to the head groups and whilst there is more freedom at the end of the chains this is still considerably less than seen with the ceramide 5 systems. This may be explained by the longer chains having less freedom due to the extended length, however the shorter chains also show less freedom indicating that it is the system itself rather than any sub-component that lacks freedom. This may be a consequence of the lack of pressure scaling in these simulations and hence an inability of the bilayers to respond to internal changes by a corresponding change in volume and pressure.

The segmental order parameter profiles in both Ceramide 4 and 5 simulations reproduce the general values found from experiment, however, the form of the profiles for both lipid systems are too flat. The direct comparison of long time scale NMR experiments with short term molecular dynamics simulations is not satisfactory and may account for some of the problems observed[6].

## 7.3 Problems associated with bilayer simulation

There are several problems associated with conducting bilayer simulations. These may be summarised

- Approximations of the model
- Degree of doping
- Size of the system employed

As already discussed the models used to describe the system have some inherent difficulties associated with them due to nature of the assumptions used. The concentration of dopant used in these simulations is much lower than that found naturally in the skin. However these systems are an attempt to probe the nature of the general interaction of the dopant with the system, so the effect of including a single cholesterol molecule is examined. These simulations have been performed upon small systems which have enabled the methodology developed to be tested and investigated. Some of the general properties associated with lipid bilayers, such as ripple phases, cannot be investigated with such small systems.

## 7.4 Further Work

A number of aspects of both the simulation and the analysis require further examination and development.

1. Due to the limitation of computer time only a very small bilayer unit has been examined. Once these techniques have been shown to adequately simulate these systems then the size of the unit cell must be increased so that much larger systems can be examined. This can be achieved by the advancement in super computer technology and software improvements which is beginning to allow these larger systems to be effectively examined.
2. The concentration of dopant molecules needs to be increased to allow the simulation of a system which is closer in chemical composition to that found experimentally in the skin.
3. No account has been taken of the role of fatty acids in the skin bilayers. These consistent an important chemical class and offer further areas of interaction in the head group region not investigated in these simulations.
4. The simulation of bilayers containing different types of skin lipids would allow for the investigation of the interaction between lipids of differing chain lengths and substitution patterns.
5. A detailed investigation of the nature of the inter-head group interactions needs to be made. The hydrogen bonding patterns of amide head groups has been

postulated elsewhere[7] and the disruption of this is thought to be involved in the absorption of substances through the skin.

6. Only a single bilayer unit has been simulated. Whilst this is the constituent unit of the intercellular lamellae it would be of benefit to examine double or even triple bilayer units. This would allow the examination of the interaction between bilayer units, an interaction that has yet to be investigated.
7. The pressure scaling algorithm gives rise to artefacts due to its direct scaling of the pressure. An investigation of the other pressure scaling algorithms available needs to be made, and a less harsh algorithm employed. There are several algorithms suggested by Allen and Tildesley[8] for conducting pressure scaling, where the rate of change of the pressure is scaled rather than the pressure itself. Some of these may be of benefit to biological simulations.

## 7.5 Concluding Remarks

This study has attempted to simulate the lipid bilayer units found in the upper most layer of the human skin, the stratum corneum, in order to allow for the dynamical and structural behaviour of these systems to be examined. Clearly considerable further work needs to be done, before a satisfactory understanding of the complex processes involved in the skin's behaviour can be achieved.

A number of problems have been highlighted and some solutions have been elucidated and a continuing effort is being made to address these in the future. This study may therefore be used to pin point some of the pit falls of such simulations and allow others to improve on the results obtained.

A number of tools have been recently developed[9] for the analysis of lipid bilayer simulations and these have been further added to in this work. These allow for the effective comparison of physical properties obtained from the trajectories with results from both other theoretical studies and experimental results.

## 7.6 References

1 W.C. Swope, H.C. Anderson, P.H. Berens and K.R. Wilson, J. Chem. Phys. 76 (1982) 637.

2 D.J. Osguthorpe and P. Dauberosguthorpe, Journal Of Molecular Graphics 10 (1992) 178.

3 D.H. Kitson, F. Avbelj, J. Moult, D.T. Nguyen, J.E. Mertz, D. Hadzi and A.T. Hagler, Proceedings Of The National Academy Of Sciences Of The United States Of America 90 (1993) 8920.

4 K.F. Lau, H.E. Alper, T.S. Thatcher and T.R. Stouch, J. Phys. Chem. 98 (1994) 8785.

5 P. Ewald, Ann. Phys. 64 (1921) 253.

6 A.J. Robinson, W.G. Richards, P.J. Thomas and M.M. Hann, Biophys. J. 68 (1995) 164.

7 I. Pascher, Biochim. Biophys. Acta 455 (1976) 433.

8 M.P. Allen and D.J. Tildesley, Computer Simulation of Liquids (Oford Science Publications, Oxford, 1987).

9 A.P. Lemon, P. Dauber-Osguthorpe and D.J. Osguthorpe, Comput. Phys. Comms. 91 (1995) 97.

# APPENDIX

The potential library used during the course of the is the published version of VFF[1].

## Atomic Charges and Potential Types

### Ceramides

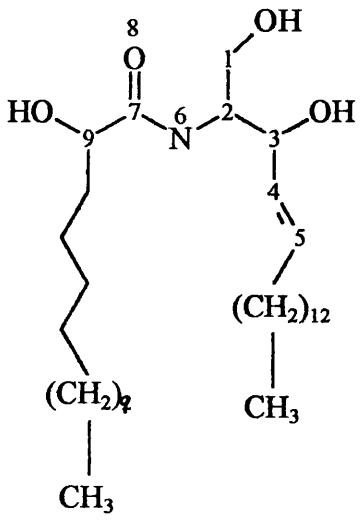


All hydrogens attached to carbons have a charge of 0.1. The charges on the other atoms of the head group and the methylene segments of the acyl chain are given below.

**Table A1**

| Atom | Potential | Charge | Atom | Potential | Charge |
|---|---|---|---|---|---|
| C1 | c2 | -0.17 | N6 | n3 | -0.5 |
| C2 | c1 | -0.12 | HN | hn | 0.28 |
| C3 | c1 | -0.07 | C7 | c' | 0.38 |
| C4 | c= | -0.1 | O8 | o' | -0.38 |
| C5 | c= | -0.1 | C9 | c2 | -0.07 |

**Table A2** Hydroxyl Group, Methyl and Methylene Potentials and Charges

| Atom | Potentials | Charge | Atom | Potential | Charge |
|---|---|---|---|---|---|
| Hydroxyl | | | Methyl | | |
| OH | oh | -0.38 | C | c3 | -0.3 |
| HO | ho | 0.35 | H | h | 0.1 |
| Methylene | | | H | h | 0.1 |
| C | c2 | -0.2 | H | h | 0.1 |
| H | h | 0.1 | | | |
| H | h | 0.1 | | | |

**Cholesterol**

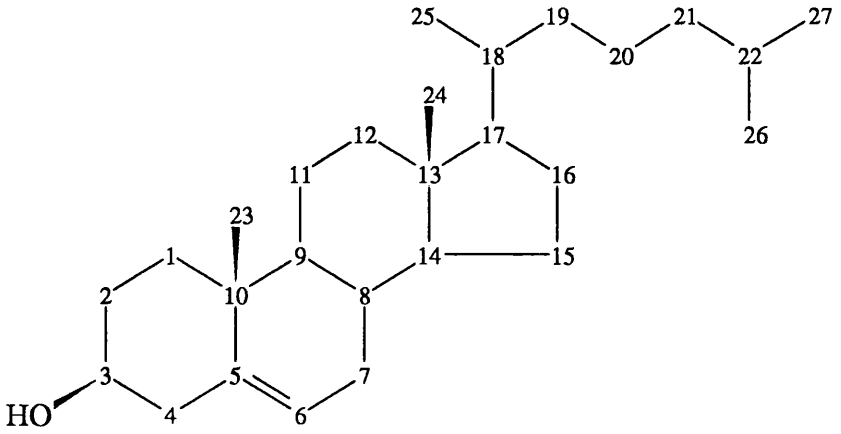


All hydrogens attached to carbons have a charge of 0.1. The charges on the carbon and oxygen atoms are listed below.

**Table A3** Cholesterol Atomic Potentials and Atom Types

| Atom | Potential | Charge | Atom | Potential | Charge |
|---|---|---|---|---|---|
| OH | oh | -0.38 | C13 | c1 | -0.1 |
| HO | ho | 0.35 | C14 | c1 | -0.1 |
| C1 | c2 | -0.2 | C15 | c2 | -0.2 |
| C2 | c2 | -0.2 | C16 | c2 | -0.2 |
| C3 | c1 | -0.07 | C17 | c1 | -0.1 |
| C4 | c2 | -0.2 | C18 | c1 | -0.1 |
| C5 | c= | 0.0 | C19 | c2 | -0.2 |
| C6 | c= | -0.1 | C20 | c2 | -0.2 |
| C7 | c2 | -0.2 | C21 | c2 | -0.2 |
| C8 | c1 | -0.1 | C22 | c1 | -0.1 |
| C9 | c1 | -0.1 | C23 | c3 | -0.3 |
| C10 | c | 0.0 | C24 | c3 | -0.3 |
| C11 | c2 | -0.2 | C25 | c3 | -0.3 |
| C12 | c2 | -0.2 | C26 | c3 | -0.3 |

## References

1 P. Dauberosguthorpe, V.A. Roberts, D.J. Osguthorpe, J. Wolff, M. Genest and A.T. Hagler, Proteins-Structure Function And Genetics 4 (1988) 31.